

Copyright
by
Taner Akkin
2003

The Dissertation Committee for Taner Akkin Certifies that this is the approved version of the following dissertation:

Biomedical Applications of a Fiber Based Low-Coherence Interferometer for Quantitative Differential Phase Measurements

Committee:

Thomas E. Milner, Supervisor

H. Grady Rylander III, Supervisor

Johannes F. de Boer

Brian L. Evans

Ashley J. Welch

**Biomedical Applications of a Fiber Based Low-Coherence
Interferometer for Quantitative Differential Phase Measurements**

by

Taner Akkin, B.S., M.S.

Dissertation

Presented to the Faculty of the Graduate School of

The University of Texas at Austin

in Partial Fulfillment

of the Requirements

for the Degree of

Doctor of Philosophy

The University of Texas at Austin

December 2003

Dedication

To my parents / Anne ve babama

Acknowledgements

This dissertation would not be complete without mentioning help and support from many people and institutions. First of all, I would like to thank and express my gratitude to my advisors Drs. Tom Milner and Grady Rylander for their guidance, support and trust. The enthusiasm and friendship they provided have been priceless. I have learnt many things from my friend Dr. Digant Davé. Digant, here is a sincere thank-you for everything. I would like to thank Drs. Johannes de Boer, Brian Evans, and A. J. Welch for improving the quality of this work by serving on my committee.

I am thankful to Dr. David Landowne for his valuable suggestions on matters related to nerve preparation, Dr. Harvey Fishman for teaching me dissection of the squid nerve, Dr. Wolfgang Frey, Ted Gaubert and Bongsu Jung for providing a calibrated sample for accuracy measurement of our system, and Dr. Sharon Thomsen for histology verification. I sincerely thank Dr. Richard Smalling's group at University of Texas Medical School at Houston for supplying arterial tissue, and Dr. Sergey Telenkov and Shriram Sethuraman for their help in the experiment. I like to thank Drs. Kirill Larin and Jong-In Youn for their participation in analyte and cartilage experiments, respectively.

I would like to thank Dr. Gracie Vargas for teaching me many practical aspects about the laboratory, Jen Siegert and Aparna Raman for being my partners in several class projects devoting long hours and days, Joe Villard for his help while I was getting used to the life and language in US, and Chris Rylander for helping me in the lab especially when the fibers and sometimes fishing lines are all tangled. Occasional help from Oliver Stumpp, Nate Kemp, Haitham Zaatari and JeeHyun Kim are greatly appreciated; thanks guys. Finally, I thank all the graduate students in the upper basement for being around whenever I needed a break. Administrative assistants cannot be forgotten, thanks a bunch Melanie Gulick, Joni Burks, Maggie Fitch, Audie Hébert and Vicki Stratton for making life as a graduate student easier.

I would like to acknowledge the Ministry of National Education of Turkey for a scholarship, which made my PhD education possible abroad. I thank UT at Austin for supporting me with a university continuing fellowship. I would also like to acknowledge financial support from the National Institute of Health and Advanced Technology Program of Texas for funding this research.

Hatice ve Kazım Akkın için: Anne ve baba, desteğiniz ve güveniniz sayesinde dilinden bir şey anlamadığınız ve size adanan bu kitap meydana geldi. Sevginizden ve adıma çektiğiniz sıkıntılardan dolayı size ne kadar teşekkür etsem azdır. Ellerinizden öperim.

Biomedical Applications of a Fiber Based Low-Coherence Interferometer for Quantitative Differential Phase Measurements

Publication No. _____

Taner Akkin, Ph.D.

The University of Texas at Austin, 2003

Supervisors: Thomas E. Milner, and H. Grady Rylander III

This dissertation presents design, implementation, and biomedical applications of a novel polarization-maintaining-fiber based phase sensitive optical low-coherence reflectometer (PS-OLCR). Using dual channels, PS-OLCR detects Angstrom/nanometer scale optical path length changes by calculating phase difference between depth resolved interference fringes. Ability to detect such small changes in optical path length at specific depths is useful in a wide variety of biomedical imaging and sensing applications. Application areas investigated in this dissertation include (i) measurement of analyte concentrations, (ii) imaging surface topography, (iii) cartilage surface response to electrical stimulation, (iv) arterial tissue response to photothermal stimulation, (v) birefringence measurement, and (vi) optical detection of neural activity. For each application, results of PS-OLCR differential phase measurements are presented.

Table of Contents

List of Tables.....	xii
List of Figures	xiii
List of Abbreviations.....	xvii
Chapter 1: Introduction	1
1.1 Motivation	1
1.2 Specific Goals	2
1.3 Dissertation Overview	3
Chapter 2: Phase Sensitive Optical Low-Coherence Reflectometer.....	7
2.1 Abstract	7
2.2 Introduction	7
2.3 Materials and Methods.....	9
2.3.1 Optical Low-Coherence Tomography.....	9
2.3.2 Phase Sensitive Optical Low-Coherence Reflectometer.....	11
2.3.3 Signals and Processing.....	16
2.4 Results	20
2.4.1 Phase Accuracy	20
2.4.2 Phase Sensitivity	22
2.4.3 Environmental Perturbations.....	25
2.5 Discussion	29
2.5.1 Polarization Mode Dispersion.....	30
2.5.2 Modulation Scheme.....	32
2.5.3 Ghost Lines	33
2.6 Conclusion.....	36
Chapter 3: Measurement of Analyte Concentrations	37
3.1 Abstract	37

3.2 Introduction	37
3.3 Materials and Methods	38
3.4 Results	40
3.5 Discussion	44
3.6 Conclusion.....	46
Chapter 4: Imaging Surface Topography	47
4.1 Abstract	47
4.2 Introduction	47
4.3 Materials and Methods	48
4.4 Results	49
4.5 Discussion	51
4.6 Conclusion.....	52
Chapter 5: Cartilage Surface Response to Electrical Stimulation.....	53
5.1 Abstract	53
5.2 Introduction	53
5.3 Materials and Methods	55
5.4 Results	56
5.5 Discussion	58
5.6 Conclusion.....	59
Chapter 6: Arterial Tissue Response to Photothermal Stimulation.....	60
6.1 Abstract	60
6.2 Introduction	60
6.3 Materials and Methods	62
6.4 Results	63
6.5 Discussion	65
6.6 Conclusion.....	66
Chapter 7: Birefringence Measurement of Nerve	67
7.1 Abstract	67

7.2 Introduction	67
7.3 Materials and Methods	68
7.4 Results	69
7.5 Discussion	72
7.6 Conclusion.....	73
Chapter 8: Optical Detection of Neural Activity	74
8.1 Abstract	74
8.2 Introduction	74
8.3 Literature Review	76
8.3.1 Nerve Anatomy	76
8.3.2 Action Potential.....	78
8.3.3 Previous Studies on Neural Activity	79
8.4 Materials and Methods	86
8.4.1 Preparation	86
8.4.2 Measurement Setup	89
8.5 Results	91
8.5.1 Surface Displacement.....	92
8.5.2 Retardation Change	104
8.5.3 Optical Path Length Change	109
8.6 Discussion	113
8.6.1 Mechanisms to Explain Surface Displacements	113
8.6.2 Comparison of Optical and Electrical Signals	115
8.6.3 Detectable Signals	116
8.7 Conclusion.....	119
Chapter 9: Summary, Future Directions and Conclusion	120
9.1 Summary	120
9.2 Future Directions.....	121
9.2.1 Optical System	122

9.2.2 Measurement of Analyte Concentrations	125
9.2.3 Electrokinetic Response of Cartilage	126
9.2.4 Photothermal Response of Arterial Tissue.....	127
9.2.5 Optical Detection of Neural Activity	127
9.2.6 Other Applications	129
9.3 Conclusion of the Dissertation	130
References	131
Vita	136

List of Tables

Table 3.1 Phase shift ($d\phi/dC$) and refractive index change (dn/dC) per unit analyte concentration. dn/dC values are extrapolated from literature at visible wavelengths, physiological ranges, and corresponding maximum phase shifts are given. (*) $d\phi/dC$, dn/dC , and C_{physiol} values for albumin and globulin are in $\text{rad}/(\text{mg}/\text{dL})$, $\times 10^{-5}/(\text{mg}/\text{dL})$, and mg/dL , respectively. 42

List of Figures

Figure 2.1: Generic system for optical coherence tomography.....	10
Figure 2.2: Phase sensitive optical low-coherence reflectometer (PS-OLCR). C- collimator, D-detector, G-diffraction grating, L-lens, M-mirror, and W- Wollaston prism.	12
Figure 2.3: Cross-section of a Panda PM fiber.	13
Figure 2.4: Sample path configurations: (a) single beam, (b) laterally and (c) longitudinally displaced channels. L-lens, and W-Wollaston prism.....	15
Figure 2.5: Coherence function of a PS-OLCR channel.....	16
Figure 2.6: Drive signal applied to LiNbO ₃ wave-guide phase modulator (a), and corresponding phase modulation of the PS-OLCR channels (b).	18
Figure 2.7: Phase extraction algorithm.	19
Figure 2.8: Chromium step-height measured by PS-OLCR and Atomic Force Microscopy (AFM). The results are in excellent agreement with each other, and demonstrate accuracy of the PS-OLCR measurement.	21
Figure 2.9: Temporal response of liquid crystal variable retarder measured by PS- OLCR. Noise on individual phase channels (φ_1 and φ_2) is removed from the differential phase signal ($\Delta\varphi$).	23
Figure 2.10: Phase sensitivity: (a) single record, and (b) average of 10 records. Averaging smoothes the noise.....	24
Figure 2.11: Perturbation of temperature change on the fiber system: (a) measured temperature in the box enclosing the fiber system, (b) axial shift of the coherence functions, and (c) relative movement of coherence functions (i.e., differential path length change).....	26
Figure 2.12: Long-term stability of the PS-OLCR.....	28
Figure 2.13: Common-mode rejection of mechanical vibrations: (a) individual path length fluctuations, and (b) change in differential path length.....	29
Figure 2.14: Coherence functions of the two PS-OLCR polarization channels (a), and a slope in phase difference along the coherence functions (b).	31
Figure 3.1: Phase shift due to concentration changes: (a) glucose and NaCl, (b) CaCl ₂ and KCl, (c) MgCl ₂ and urea, and (d) albumin and globulin. Straight lines are the linear fit using a least-squares algorithm, and bars indicate the standard deviation of the measurements.	41
Figure 3.2: Phase shift due to change in glucose concentrations in scattering media with scattering coefficients of (a) $\mu_s \cong 50 \text{ cm}^{-1}$ and (b) $\mu_s \cong 100 \text{ cm}^{-1}$. Straight lines are the linear fit using least-squares algorithm, and bars indicate standard deviation of the measurements.....	44
Figure 4.1: Sample path configuration to scan spatially separated polarization channels laterally on the sample, where L- lens, W-Wollaston prism, and arrows indicate polarization states.	48

Figure 4.2: Surface features on a chromium film. The dashed ovals indicate the same feature in the transition region. One is inverted due to the negative sign in differential phase calculation.	50
Figure 4.3: Three-dimensional image of a chromium step (~150 nm). Smaller surface features in the order of 10 nm exist.	51
Figure 5.1: Experimental setup used in surface displacement of cartilage.	55
Figure 5.2: Surface displacements of electrically stimulated cartilage. Stimulation amplitude: 5 V, stimulation frequencies: (a) 1 Hz, (b) 0.5 Hz, and (c) 0.2 Hz. Dashed lines indicate the stimuli with arbitrary amplitudes.	56
Figure 5.3: Surface displacements of electrically stimulated cartilage. Stimulation amplitude: 10 V, stimulation frequencies: (a) 1 Hz, (b) 0.5 Hz, and (c) 0.2 Hz. Dashed lines indicate the stimuli with arbitrary amplitudes.	57
Figure 6.1: Experimental setup used in measurement of photothermal response of an atherosclerotic artery.	62
Figure 6.2: Depth resolved intensity image of an atherosclerotic rabbit artery.	63
Figure 6.3: Individual ($p1$, $p2$) and differential (Δp) path length variations between two points in arterial tissue in response to laser excitation. $p1$ and $p2$ are recorded from 100 μm and 200 μm below the luminal surface, respectively. (a) and (b) from healthy area, and (c) and (d) from above the plaque. Positive cycles of rectangular waveforms indicate laser excitation.	65
Figure 7.1: Sample path configuration of PS-OLCR to image a crayfish nerve.	68
Figure 7.2: Depth resolved intensity and phase images of a crayfish nerve.	70
Figure 7.3: Maximum phase retardation due to birefringence of a crayfish nerve. Measurement is performed when the nerve was along one of the polarization channels (0° orientation).	71
Figure 7.4: Measured phase retardations as a function of nerve orientation.	72
Figure 8.1: Nerve chamber.	88
Figure 8.2: Sample path configurations of PS-OLCR for measuring (a) surface displacement, (b) retardation change, and (c) optical path length change of an excited nerve.	90
Figure 8.3: Histology (trichrome staining) of a crayfish walking leg nerve. Experiment data shown in Figure 8.4 are recorded from this nerve.	93
Figure 8.4: Optical path length change due to surface displacement of a stimulated crayfish leg nerve. Action potentials are in arbitrary units. Stimulus (300 μA , 50 μs) is at 2 ms. (a) and (b) are recorded from spatially close (<1 mm) but different points on the nerve. Optical signals are average of 500 responses.	94
Figure 8.5: Histology (trichrome staining) of a crayfish walking leg nerve. Experiment data shown in Figure 8.6 are recorded from this nerve.	95
Figure 8.6: Optical path length change due to surface displacement of a stimulated crayfish leg nerve. Action potentials are in arbitrary units. Stimulus (300 μA , 50 μs) is at 2 ms. (a) and (b) are recorded from top surface (average of	

500 responses), and 15 μm below the top surface (average of 250 responses) of the nerve, respectively.	97
Figure 8.7: Histology (trichrome staining) of a crayfish walking leg nerve. Experimental data shown in Figure 8.8 and Figure 8.9 are recorded from this nerve.	98
Figure 8.8: Control experiment of surface displacement with stimulus amplitude below and above the action potential threshold. Action potentials are in arbitrary units. Stimulus duration is 50 μs and presented at 2 ms. (a) and (c) with stimulus amplitude of 60 μA , and (b) and (d) with stimulus amplitude of 100 μA . Optical signals are average of 100 responses, and recorded from top surface of a crayfish leg nerve.	99
Figure 8.9: Control experiment of surface displacement with stimulus amplitude below and above the action potential threshold. Action potentials are in arbitrary units. Stimulus duration is 50 μs and presented at 2 ms. (a) with stimulus amplitude of 1.4 mA, and (b) with stimulus amplitude of 3 mA. Optical signals are average of 200 responses, and recorded from top surface of a crayfish leg nerve.	101
Figure 8.10: Histology (trichrome staining) of a squid (<i>Lolliguncula brevis</i>) nerve. Experimental data shown in Figure 8.11 is recorded from this nerve.	102
Figure 8.11: Optical path length change of a surface displacement experiment performed on a stimulated squid nerve. Action potential is in arbitrary unit. Stimulus (4 mA, 50 μs) is at 2 ms. 500 optical responses are averaged.	103
Figure 8.12: Histology (trichrome staining) of a crayfish walking leg nerve. Experimental data shown in Figure 8.13 is recorded from this nerve.	105
Figure 8.13: Optical path length change of a retardation change experiment performed on a stimulated crayfish nerve. Action potential is in arbitrary unit. Stimulus (300 μA , 50 μs) is at 2 ms. 500 optical responses are averaged. There is no indication of neural activity in the given range of PS-OLCR signal.	106
Figure 8.14: Histology (trichrome staining) of a squid nerve. A giant axon, fin nerve (small axons), and perineurium are indicated. Experimental data shown in Figure 8.15 is recorded from this nerve.	107
Figure 8.15: Optical path length change of a retardation change experiment performed on a stimulated squid nerve. Action potential is in arbitrary unit. Stimulus (3 mA, 50 μs) is at 2 ms. 1500 optical responses are averaged. There is no indication of neural activity in the given range of PS-OLCR signal.	108
Figure 8.16: Optical path length change experiment performed on a stimulated crayfish nerve. Action potential is in arbitrary unit. Stimulus (300 μA , 50 μs) is at 2 ms. 500 optical responses are averaged. There is no indication of neural activity in this figure.	110

Figure 8.17: Histology (trichrome staining) of a squid nerve. A giant axon, fin nerve (small axons), and perineurium are indicated. Experimental data shown in Fig. 8.18 are recorded from this nerve.....	111
Figure 8.18: Optical path length change experiment performed on a stimulated squid nerve. Stimulus (50 μ s) is 75 μ A for the lower trace and 300 μ A for the upper trace, and presented at 1 ms. Optical traces are average of 250 responses that are recorded from different regions of the nerve. Action potentials are not available.....	112
Figure 9.1: Frequency multiplexed optical low-coherence reflectometer. C- collimator, D- photo detector, G- diffraction grating, L- lens, M-mirror, PS- polarization splitter, V- modulation voltage, and W-Wollaston prism. Small rectangles indicate fiber splices and the values show the splice angle in degrees.....	123

List of Abbreviations

A/D	Analog to Digital converter
AFM	Atomic Force Microscope
FM-OLCR	Frequency Multiplexed Optical Low-Coherence Reflectometer
FWHM	Full-Width Half-Maximum
LCVR	Liquid Crystal Variable Retarder
LiNbO ₃	Lithium Niobate
NA	Numerical Aperture
mM	milliMolar
Ms/s	Mega sample per second
OCT	Optical Coherence Tomography
PM	Polarization Maintaining
PS-OLCR	Phase Sensitive Optical Low-Coherence Reflectometer
RSOD	Rapid Scanning Optical Delay-line

Chapter 1: Introduction

1.1 MOTIVATION

Everyday, people suffering from various diseases are rushed to hospitals for diagnosis and treatment. Although modern medicine can provide solutions to many health problems, diseases have to be diagnosed quickly and accurately before beginning therapy. Treatments as well as diagnostic methods require better understanding of health conditions. Tissue-imaging modalities with different contrast and resolution provide valuable information about health, and are being used in diagnostic and therapeutic techniques. Noninvasive methods are particularly important, because time, resources and risk taken in associated procedures may be greatly minimized.

In recent years, use of light to image depth features in tissue has become a promising field of research. Optical coherence tomography (OCT) can image biological tissue with micrometer axial resolution using depth-resolved interference fringes. In interferometry, both amplitude and phase of the fringes carry physical information about the target. Differential measurements provided by dual channel interferometers improve the signal to noise ratio significantly by rejecting common mode noise. Sub-wavelength changes in optical path length at specific depths can be detected by differential phase measurements. Detection of such small changes in optical path length is useful in a wide variety of biomedical imaging and sensing applications.

1.2 SPECIFIC GOALS

Optical coherence tomography is a non-invasive, single channel, amplitude-only device that can image a target with depth resolved slices. As in OCT, a phase sensitive optical low-coherence reflectometer (PS-OLCR) yields non-invasive, depth resolved ($\sim 10 \mu\text{m}$) imaging of tissue microstructures. PS-OLCR uses a polarization-maintaining (PM) fiber to measure Angstrom/nanometer scale optical path length changes between two depth-resolved polarization channels using differential phase measurements. Therefore, PS-OLCR provides not only the amplitude images, but also differential phase contrast. First PS-OLCR (Davé, Akkin, Milner, and Rylander III, 2001) instruments reported nanometer ($\sim 5 \text{ nm}$) resolution in optical path length change and frequency multiplexing capability. In the beginning, PS-OLCR was not suitable for many applications including imaging, because of a significant number (~ 15) of ghost lines in the proximity of coherence functions. In other words, an image of a single tissue layer was corrupted by approximately 15 additional layers that were as large as one tenth of the main layer. I proposed to overcome this limitation, and improve the PS-OLCR sensitivity further. My primary contribution to PS-OLCR instrumentation is redesign of the fiber-based system to remove ghost lines and achieve at least 5X increase in resolution allowing Angstrom/nanometer scale path length changes in a single acquisition.

After demonstrating accuracy and sensitivity, a well-characterized and optimized PS-OLCR is now available to investigate a variety of biomedical research problems. With the 5X improvement in resolution, I used the PS-OLCR

system to measure nanometer scale optical path length changes in clear and scattering media with high lateral ($\sim 10 \mu\text{m}$) and longitudinal ($\sim 10 \mu\text{m}$) resolution. My other major contribution presented in this dissertation is the quantitative analysis of refractive index, birefringence and surface displacement of biological tissues using PS-OLCR differential phase measurements. Specifically, tissue responses to external stimuli (i.e. electrical or photothermal) are investigated, since the response can indicate important information about health and possibly be used as a diagnostic tool. If a clinical diagnostic device similar to that presented here is designed, work reported in this dissertation will provide an important basis.

Over the last fifty years many studies have been reported for optical detection of neural activity. Since neural diseases such as glaucoma, multiple sclerosis and Alzheimer's are debilitating and nerve cell death is irreversible, any diagnostic tool that provides a measure of neural functionality is extremely important. Results reported in my dissertation indicate that PS-OLCR is a good candidate for non-invasive measurement of changes in an excited nerve. Realization of such a clinical diagnostic device that may aid in the early detection of neural diseases would be a lifetime achievement for me.

1.3 DISSERTATION OVERVIEW

After the introduction, *Chapter 2* describes the PS-OLCR system in detail. Basic theory of optical low-coherence interferometry, signal processing, accuracy and sensitivity measurements of PS-OLCR, and studies to improve PS-OLCR

system performance are presented. Identifying important optical problems such as existence of ghost lines and dispersion associated with PS-OLCR, and implementing appropriate engineering solutions are important contributions of this dissertation. Differential phase measurements recorded by PS-OLCR provide Angstrom/nanometer scale changes in optical path length at specific depths in a specimen. Measurement of such small optical path length changes in tissue is useful in a wide variety of biomedical imaging and sensing applications. Subsequent chapters introduce various applications using PS-OLCR differential phase measurements. Importance of the applications and associated contributions are stated below.

Chapter 3 presents PS-OLCR measurement of analyte concentrations in clear and turbid media. Phase shifts due to concentration changes of major body analytes including glucose are measured, and found consistent with the results previously reported at visual wavelengths. Because estimated number of people suffering diabetes is more than 150 million and the current glucose sensing techniques involve a finger puncture for blood analysis, non-invasive measurement of glucose concentration is crucial. Optical techniques suggested for non-invasive measurement of glucose concentration have limitations associated with low sensitivity and accuracy in the physiological range (3-30 milliMolar). The high accuracy and sensitivity of PS-OLCR may be important in clinical studies. Methods that achieve sub-milliMolar sensitivity are discussed.

Chapter 4 demonstrates non-contact imaging of surface topography, which is important to detect surface quality and defects in materials. Since stylus-

profiling techniques may be deleterious to the surface, alternative instruments have been developed. PS-OLCR with its dual-beam differential phase operation is presented for non-contact characterization of surface structures. Images of chromium film surfaces are acquired with nanometer scale sensitivity. Measurement of surface topography discontinuities and surface imaging of biological structures are discussed.

Chapter 5 explores surface displacements in electrically stimulated cartilage. Effects of stimulus amplitude and frequency on cartilage surface displacement are studied and compared with previous reports. Use of PS-OLCR in non-contact diagnosis of osteoarthritis is proposed.

Chapter 6 investigates laser-induced photothermal changes inside arterial tissue. Detection of vital arterial plaques may require not only a high-resolution imaging technique, but also measurement of mechanical properties of the plaque. Absorption of laser radiation results in a localized temperature increase that stimulates a photothermal tissue response. Nanometer scale optical path length changes between two points in arterial tissue in response to laser excitation are measured using PS-OLCR. The tissue response may be useful in identifying plaque associated with atherosclerosis. Although such a response is believed to be different in healthy and atherosclerotic arteries, development of this technique requires further investigation.

Chapter 7 examines PS-OLCR birefringence measurement using a nerve cord dissected from crayfish. System performance is tested at several specimen angular orientations. An angle-independent configuration is discussed.

Chapter 8 presents PS-OLCR detection of neural activity. Transient changes in nerve associated with action potential propagation are studied. To obtain a non-invasive tool to diagnose neural diseases, many experiments on surface displacement, change in retardation, and change in optical path length are performed on crayfish and squid nerves. Together with these PS-OLCR measurements, electrical action potential and histology of the nerves are presented. Nerves dissected from crayfish walking legs resulted in approximately 1 nm surface displacement associated with action potential propagation. No chemicals or reflection coatings that may harm the nerve were applied. Therefore, this non-invasive technique may be used for early detection of neural diseases such as glaucoma, multiple sclerosis and Alzheimer's.

Finally, *Chapter 9* presents a summary, future directions and conclusion of the dissertation. Measurement of ultra-small changes in optical path length at specific depths is achieved by the differential phase measurement provided by PS-OLCR. Several biomedical imaging and sensing applications are demonstrated in the dissertation chapters. For future studies, a new fiber-based system capable of frequency multiplexing the polarization channels is proposed for differential phase measurements. The proposed system may improve the signal to noise ratio of the current PS-OLCR, and yield more information since the polarization channels and cross-terms are coded in different electrical frequencies. *Chapter 9* also points out future studies for specific applications related to obtain diagnostic tools.

Chapter 2: Phase Sensitive Optical Low-Coherence Reflectometer

2.1 ABSTRACT

In many optical imaging applications such as monitoring cell and tissue dynamics and imaging of turbid biological samples, detection of ultra-small path length changes provides a useful contrast mechanism. A fiber based phase sensitive optical low-coherence reflectometer is designed and implemented to measure Angstrom/nanometer scale path length changes in highly scattering media with high lateral ($\sim 10 \mu\text{m}$) and longitudinal ($\sim 10 \mu\text{m}$) spatial resolution. This chapter describes the system design and presents performance data and specifications.

2.2 INTRODUCTION

Dual-channel phase sensitive interferometers are capable of measuring sub-wavelength changes in optical path length. Implementations of phase sensitive interferometers utilizing either two polarization (Hitzenberger and Fercher, 1999; Davé and Milner, 2000; Davé *et al.*, 2001) or wavelength (Yang *et al.*, 2000) channels have been reported. Measurement of phase difference between interferometric fringes in the two channels eliminates environmental noise in a common mode fashion and provides excellent phase sensitivity.

The phase sensitive optical low-coherence reflectometer (PS-OLCR) is a novel fiber based differential phase interferometer. With its dual channels, each

of which represents orthogonal modes of a polarization-maintaining (PM) fiber, the PS-OLCR yields fast, accurate and sensitive measurements of relative optical path length differences between the two channels. PS-OLCR has high lateral ($\sim 10\ \mu\text{m}$), longitudinal ($\sim 10\ \mu\text{m}$) and differential phase ($\sim 10^{-3}$ radian) resolution. This allows depth resolved measurement of Angstrom/nanometer scale path length differences, which creates a system that will aid scientists and engineers investigate important phenomena in biomedical engineering and develop useful diagnostic and therapeutic imaging approaches. Applications of PS-OLCR include high resolution intensity and phase imaging, determination of refractive index and birefringence, surface profilometry, measurement of tissue response to external stimuli, measurement of transient changes in surface displacement, birefringence and optical path length, as well as endoscopic and microfluidic bio-sensing.

In this chapter basic theory of optical low-coherence interferometry, a detailed description of the fiber-based PS-OLCR system including sample path configurations and signal processing, and measurements demonstrating system phase accuracy and phase sensitivity are presented. Environmental perturbations on PS-OLCR such as vibration and temperature changes are studied, and common-mode-rejection-ratio of the differential phase system is quantified. Polarization mode dispersion, modulation scheme and a study of ghost lines in the interferometer design are discussed, and improvements in PS-OLCR performance are explained.

2.3 MATERIALS AND METHODS

Section 2.3.1 presents the optical low-coherence interferometry, and states basic formulations on interference signal and resolutions. Section 2.3.2 describes design and construction of PS-OLCR with various sample path configurations. In Section 2.3.3, signals acquired by PS-OLCR are explained and associated signal processing algorithms are suggested.

2.3.1 Optical Low-Coherence Tomography

The work on white-light interferometry led to the development of optical-coherence domain reflectometry, a one-dimensional optical ranging technique (Youngquist *et al.*, 1987; Takada *et al.*, 1987), and optical low-coherence tomography (OCT) (Huang *et al.*, 1991), an imaging technique to produce high-resolution ($\sim 10 \mu\text{m}$) cross-sectional images of tissue microstructures. OCT is similar to ultrasound imaging except it uses infrared light instead of acoustic waves. Inasmuch as the OCT works with back-reflected light, non-invasive measurements of tissue and cell properties are possible. Because systems can be constructed using optical fibers, high-resolution imaging of internal organ microstructures is possible through catheter and endoscopic probes. A good review on OCT can be found in Schmitt, 1999.

Figure 2.1 illustrates a basic fiber-based OCT system. The 2×2 coupler splits a broadband source field into reference (E_r) and sample (E_s) fields. While E_r is back-reflected from the reference mirror, the sample field coupled back to the interferometer is modified by the tissue (E'_s). Light returning from reference

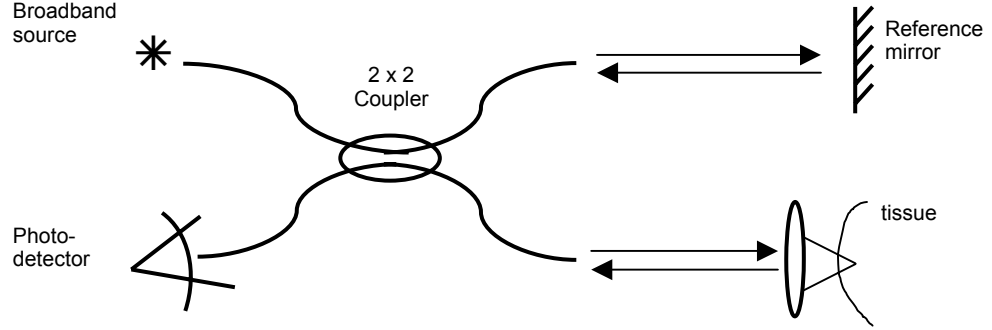


Figure 2.1: Generic system for optical coherence tomography.

and sample paths mixes in the coupler and constructs an interference signal on a photodetector. The detected intensity is,

$$I_d = \langle |E_d|^2 \rangle = \frac{I_r + I'_s}{2} + \Re \left\{ \langle E_r^*(t + \tau) E'_s(t) \rangle \right\} \quad (2.1)$$

where I_r and I'_s are respective DC intensities of reference and sample arms, \Re indicates real part of a complex function, $\langle \rangle$ represents an ensemble average, $*$ is complex conjugate operator and τ is the optical delay adjusted by the reference mirror position. Assuming the tissue does not alter the sample beam, the correlation amplitude depends on the temporal coherence characteristics of the light source. The Wiener-Khinchin theorem states that the complex temporal coherence function $\Gamma(\tau)$ is related to the power spectral density of the source $S(\nu)$ as

$$\Gamma(\tau) = \int_0^\infty S(\nu) \exp(-j2\pi\nu\tau) d\nu. \quad (2.2)$$

The axial resolution Δz is determined by the center wavelength λ_o and the spectral bandwidth $\Delta\lambda$ of the light source. The axial resolution for light sources with a Gaussian-shaped power spectral density is given by

$$\Delta z = \frac{2 \ln 2}{\pi} \left(\frac{\lambda_o^2}{\Delta\lambda} \right) \quad (2.3)$$

where Δz and $\Delta\lambda$ represent the full width at half maximum (FWHM) values. Since the axial resolution is inversely proportional to the bandwidth of the light, broad bandwidth optical sources are necessary to achieve high axial resolution.

The lateral resolution Δx is related to the sample path optics that focuses the beam on the sample, and given by

$$\Delta x = \frac{4\lambda}{\pi} \left(\frac{f}{d} \right) \quad (2.4)$$

where d is the spot size on the lens with the focal length f . High lateral resolution requires a lens with high numerical aperture (NA), and correspondingly a small beam spot at the focus. A tradeoff exists between lateral resolution and depth of focus. However, the depth (axial) resolution in most OCT systems is determined by the coherence length of the light source.

2.3.2 Phase Sensitive Optical Low-Coherence Reflectometer

Figure 2.2 illustrates a schematic diagram of a dual channel phase-sensitive optical low-coherence reflectometer (PS-OLCR) whose channels correspond to orthogonal polarization modes of the PM fiber. The PS-OLCR is constructed with PM Fujikura Panda fiber. Fiber segments are spliced by using a

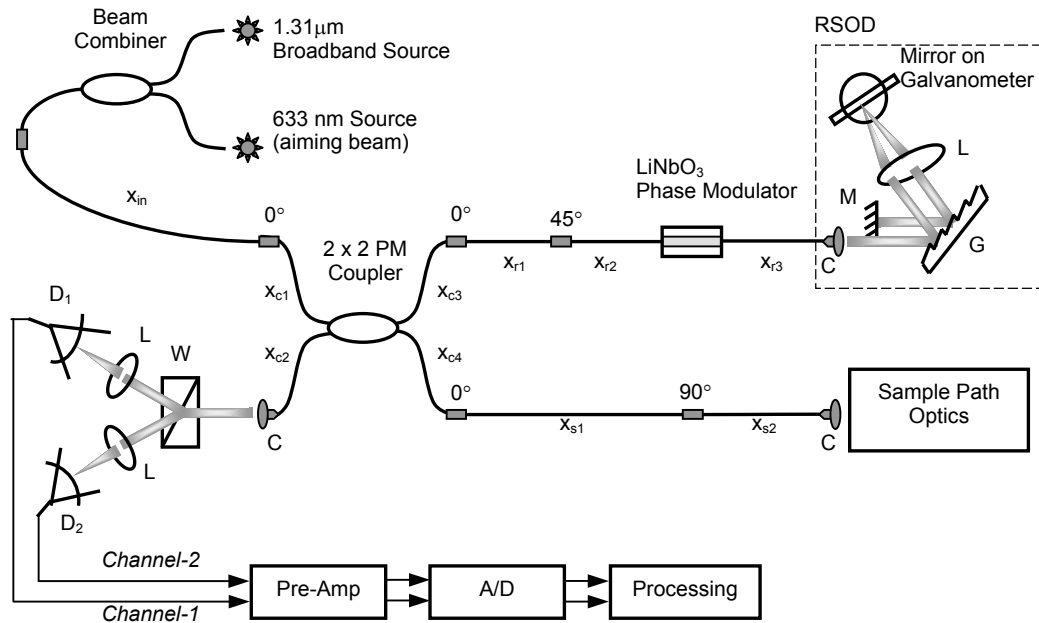


Figure 2.2: Phase sensitive optical low-coherence reflectometer (PS-OLCR). C-collimator, D-detector, G-diffraction grating, L-lens, M-mirror, and W-Wollaston prism.

commercial fiber splicing workstation (Vytran FS 2000) that allows precise alignment of fiber cores and stress axes. Small rectangles in Figure 2.2 represent fiber splices and values above indicate splice angles in degrees between corresponding axes of PM fiber segments.

As shown in Figure 2.3, PM fibers have two stress applying rods within the cladding. Because of anisotropic stress applied to the fiber core in which light travels, refractive index for oscillations along horizontal and vertical directions are different. Application of stress in the PM fiber produces birefringence, and light travels at different speeds in orthogonal channels. Consequently the PM fiber

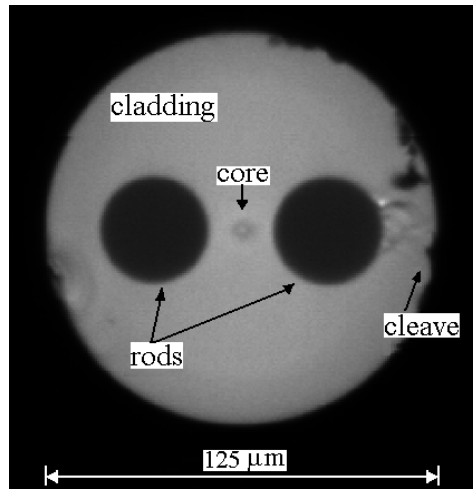


Figure 2.3: Cross-section of a Panda PM fiber.

channels are usually called fast (**f**) and slow (**s**) channels. Interferometer design and splicing of fiber segments are crucial when working with PM fibers.

Single mode, partially polarized light emitted by an optical semiconductor amplifier [$\lambda_0=1.31\mu\text{m}$ and $\Delta\lambda(\text{FWHM})\approx 60\text{nm}$] is combined with a 633 nm source (aiming beam) and delivered to the system. A long input PM fiber segment ($x_{in}+x_{c1}$) creates two decorrelated linearly polarized modes that propagate along the birefringent axes of the PM fiber. Since an off-the-shelf 2×2 PM coupler is supplied with 1 m fiber leads, optical path length in input, reference and sample arms of the coupler are extended by splicing an additional segment of PM fiber with axes at the same orientation (0° splice).

Because the light can propagate through a lithium niobate (LiNbO_3) electro-optic waveguide phase modulator in one linear polarization state (slow channel), a 45° splice in the reference path is necessary to couple both modes

equally into the axis of the modulator. As light in both channels travels the same optical path length in the reference arm after the 45° splice ($x_{r2}+x_{r3}$), fiber lengths attached to the coupler in the sample arm must ensure that the fast and slow polarization channels propagate equivalent optical path lengths. To locate both coherence functions at the same position, a 90° splice in sample path satisfies the following fiber length requirement when the beat lengths of the fiber segments are equal (beat length is the length of PM fiber that delays the polarization channels by a wavelength),

$$x_{c3} + x_{r1} = x_{c4} + x_{s1} - x_{s2}. \quad (2.5)$$

The reference arm includes a rapid scanning optical delay line (RSOD) (Tearney *et al.*, 1997). The RSOD can be configured to compensate material and waveguide dispersion introduced by the LiNbO₃ phase modulator. Dispersion is varied by adjusting the grating-lens separation, so the width of the coherence function is reduced to its minimum value. The RSOD provides linear scans and allows independent control of phase and group delays.

Configuration of sample path optics depends on the specific application. Figure 2.4 illustrates three main configurations. The basic configuration, which only focuses light on a sample (Figure 2.4a), can be used for intensity and phase imaging as well as measurement of birefringence change in tissues. The other two configurations are laterally and longitudinally displaced polarization channels. Figure 2.4b include a Wollaston prism that displaces the orthogonal polarization channels (arrows) laterally. The laterally displaced channels measure relative change in optical path length between two tissue points on which the

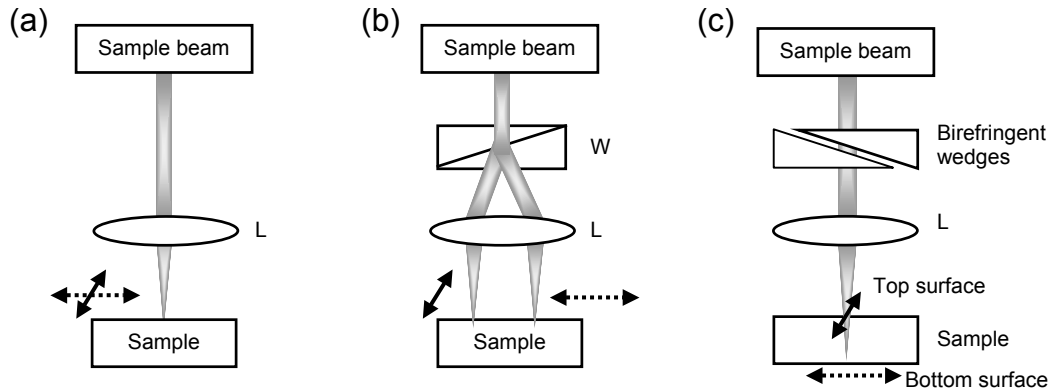


Figure 2.4: Sample path configurations: (a) single beam, (b) laterally and (c) longitudinally displaced channels. L-lens, and W-Wollaston prism.

beams are focused. In Figure 2.4c, a pair of birefringent wedges with axis aligned with the polarization channels delays the two channels longitudinally. The longitudinally displaced channels can measure optical path length change between two longitudinal points that cause depth-resolved interferometric fringe signals. Sample path configurations used in specific experiments will be described further in the next chapters.

When reference and sample path lengths are equal, light back reflected from these arms form an interference signal in the 2×2 PM coupler. A Wollaston prism in the detection path separates the two polarization channels for signal detection. Output of each photo-detector is amplified and band-pass filtered in the analog continuous-time domain. Signals are digitized by a 12-bit analog-to-digital converter and stored in computer memory for processing.

2.3.3 Signals and Processing

Axial resolution in intensity images is highly depended on coherence length given by the spectrum of the source light as described by (2.3). The coherence function recorded from one PS-OLCR polarization channel is illustrated in Figure 2.5. Because the RSOD is configured to introduce only the group delay, the LiNbO₃ phase modulator provides the fringe pattern at a desired frequency.

Depth resolved intensity images of tissues can be obtained by an envelope detection algorithm that uses low-pass filtering of the squared channels (incoherent detection, or amplitude demodulation). Since the number of photons detected decreases exponentially with depth due to scattering and absorption, processed data is usually displaced on a logarithmic or decibel (dB) scale. To

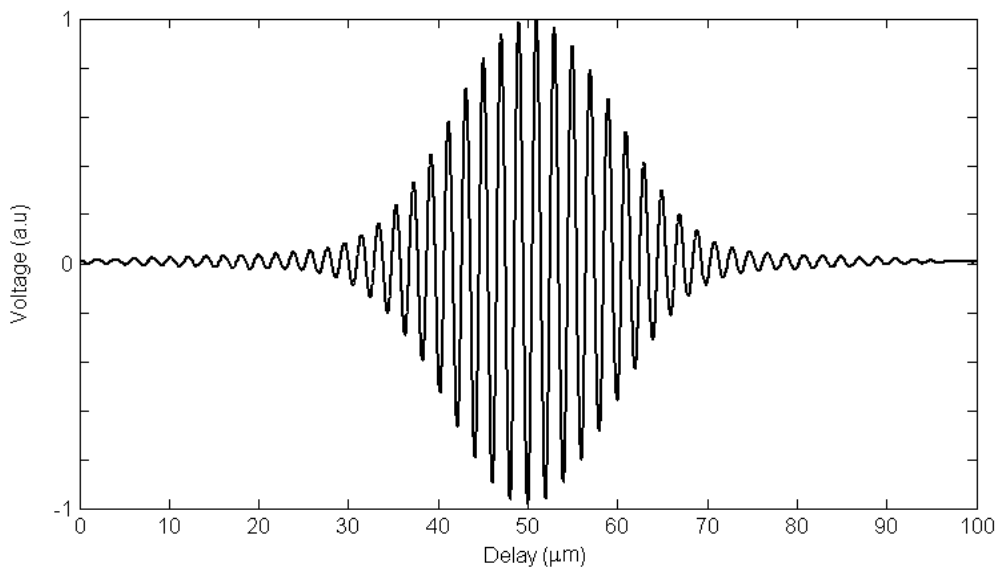


Figure 2.5: Coherence function of a PS-OLCR channel.

construct a cross sectional image, multiple depth scans are acquired and combined sequentially, while the sample is scanned slowly.

Detected light intensity in PS-OLCR channels as a function of temporal delay between light in sample and reference paths is given by the expression,

$$\begin{aligned}
I_m(\tau) &= \left\langle \left| E_{r,m}(t) + E_{s,m}(t - \tau) \right|^2 \right\rangle \\
&= \left\langle \left| E_{r,m}(t) \right|^2 \right\rangle + \left\langle \left| E_{s,m}(t - \tau) \right|^2 \right\rangle \\
&\quad + 2\Re \left\langle E_{r,m}(t) E_{s,m}^*(t - \tau) \right\rangle
\end{aligned} \tag{2.6}$$

where E is the electric field amplitude, and m stands for fast (**f**) and slow (**s**) channels. Assuming the source spectral density is Gaussian with spectral width $\Delta\omega$, the interference term of the above equation becomes proportional to,

$$I_m(\tau) \propto e^{-(\tau/4a^2)} \cos(f\tau + \varphi_m + \phi_N) \tag{2.7}$$

where $a = (\ln 2)^{1/2} / \Delta\omega$, f is the modulation frequency of the phase modulator, ϕ_N is the phase noise in the interferometer due to environmental perturbation, and φ is the phase factor that carries physically relevant information about the specimen. φ in **f** or **s** channels is proportional to the optical path length difference between reference and sample paths which change due to changes in refractive index or physical movement of the sample along the optical axis. Since ϕ_N is present in both channels, noise is cancelled by computing phase difference between the two channels ($\Delta\varphi = \varphi_s - \varphi_f$). Because path length change between polarization channels (Δp) is calculated from phase difference, sub-wavelength path length changes can be measured.

$$\Delta p = \frac{\lambda}{4\pi} \Delta \varphi \quad (2.8)$$

In many applications such as determination of solute concentrations and monitoring surface response of stimulated tissues, measurement of phase difference between the interferometric fringes in the two polarization channels is sufficient. In these cases, instead of scanning tissue in depth over many coherence lengths, stable sinusoidal fringes are obtained by the phase modulation that scans only one fringe repeatedly. To do so, reference and sample optical path lengths are made equal and the LiNbO₃ wave-guide phase modulator is driven with a ramp waveform (Figure 2.6a). To avoid phase jumps in the interference fringes, voltage amplitude of the drive signal (V_π) results in one complete fringe modulation (2π) in double passage of the light as shown in Figure 2.6b.

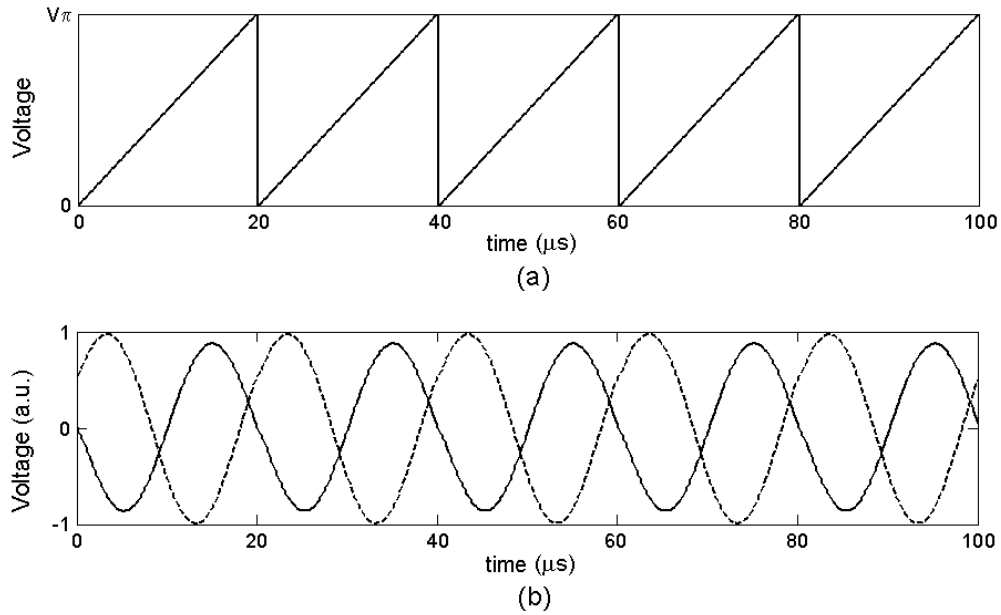


Figure 2.6: Drive signal applied to LiNbO₃ wave-guide phase modulator (a), and corresponding phase modulation of the PS-OLCR channels (b).

Figure 2.7 outlines the phase extraction algorithm applied to data stored in computer memory. Digital band-pass filtering of input data reduces noise in the channels. Given that information is contained in the computed phase and signal to noise ratio limits sensitivity, filtering must be completed with care. For example, a zero-phase filter response can be guaranteed by using a ‘forward and reverse filtering’ technique. The pass-band of the band-pass filter must be sufficiently wide to cover the bandwidth of the phase signal. Although many candidate filter types are available, Chebyshev type II bandpass filters, which are monotonic in the passband and equiripple in the stopband provide good results.

Phase of fringes in each channel are calculated by computing the angle between the signal and its Hilbert transform (Figure 2.7). Because the Hilbert transform in many software tools is based on the fast Fourier transform algorithm, the processing time is shortened if the data length is a power of two. Computed phases (in radians) are unwrapped to remove phase jumps, and the subsequent subtraction yields the phase difference, $\Delta\phi$. Relative path length change between the channels (Δp) is calculated from $\Delta\phi$ in (2.8).

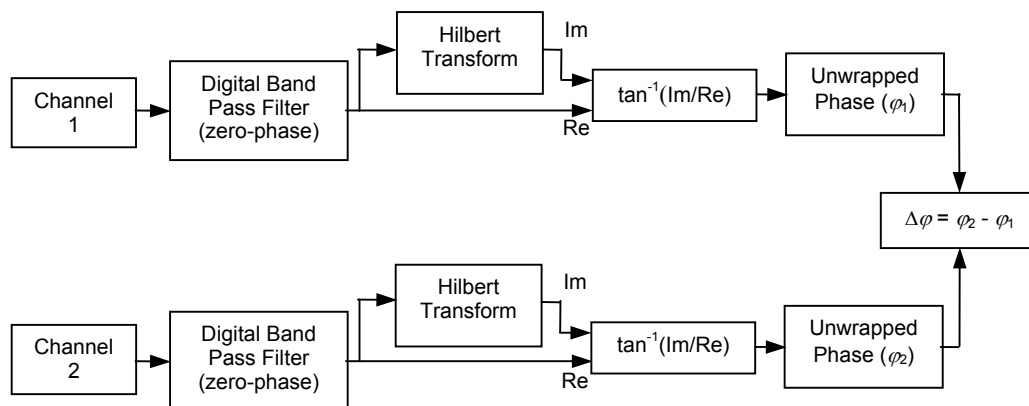


Figure 2.7: Phase extraction algorithm.

2.4 RESULTS

In this section, experimental results on phase accuracy (Section 2.4.1), phase sensitivity (Section 2.4.2) and environmental perturbations (Section 2.4.3) are presented. The PS-OLCR phase accuracy is demonstrated by lateral scanning of a chromium step sample. Atomic force microscope (AFM) confirmed the accuracy of the PS-OLCR measurement. Then, phase sensitivity is found by using a liquid crystal variable retarder positioned in the sample path. Common-mode-rejection-ratio of the system is quantified, as well. Effects of environmental perturbations such as vibration and temperature change are studied to show stability of the PS-OLCR.

2.4.1 Phase Accuracy

Phase accuracy of the PS-OLCR is demonstrated by measuring path length change of laterally displaced channels scanned over a chromium step. To prepare the chromium step sample, a chromium film layer is deposited on a glass substrate. Then, one half of the layer is covered with a second layer of chromium. The sample path configuration used to determine the step-height is as shown in Figure 2.4b. Sinusoidal fringe data of laterally displaced channels is acquired while the sample is translated laterally. When one of the polarization beams cross the step, it induces a phase change in the corresponding channel. The step-height is calculated from the differential phase data using (2.8), and found to be 152 nm. To validate the accuracy of the PS-OLCR measurement, two AFM images were recorded near the optical measurement area. Each AFM image having 512 traces

was averaged to determine the step height. Average step-heights in the first (region-1) and second (region-2) AFM images were 146 nm and 155 nm, respectively. These numbers are in excellent agreement with the PS-OLCR measurement (152 nm). Figure 2.8 illustrates the step-height measured by a single PS-OLCR record, and by the two AFM averages. Besides, the transition region in the PS-OLCR curve depends on the beam diameter, and the *en face* images are accessible by appropriate scanning of the sample beam. The scanning setup and three-dimensional image of the chromium step is presented in surface topography chapter (Chapter 4).

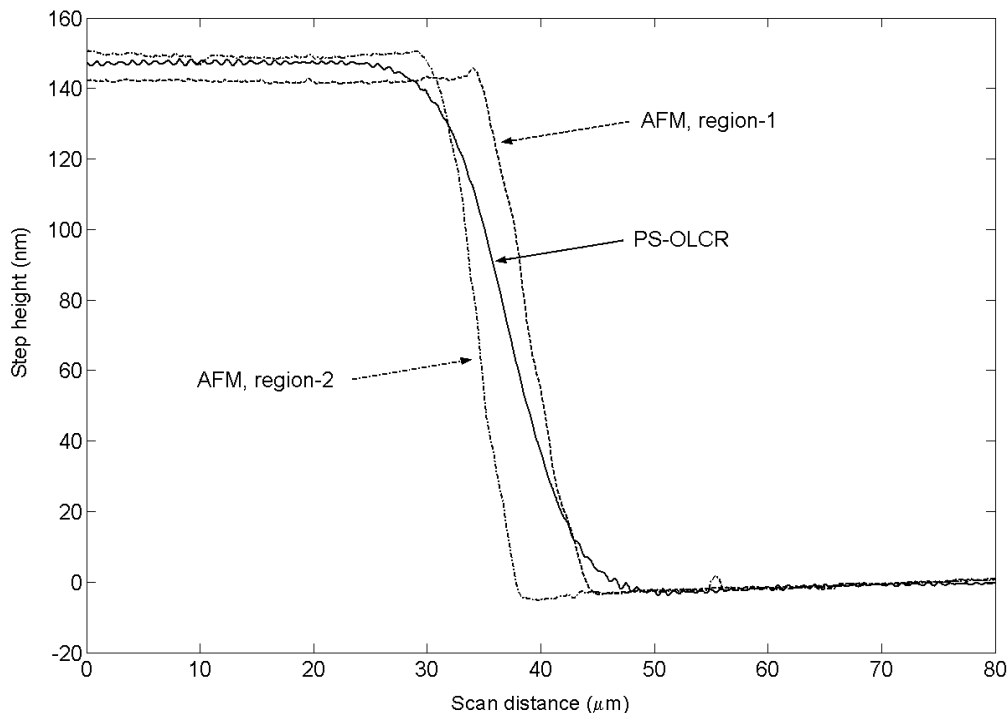


Figure 2.8: Chromium step-height measured by PS-OLCR and Atomic Force Microscopy (AFM). The results are in excellent agreement with each other, and demonstrate accuracy of the PS-OLCR measurement.

2.4.2 Phase Sensitivity

Phase sensitivity of PS-OLCR is demonstrated by using a liquid crystal variable retarder (LCVR) manufactured by Meadowlark Optics (Frederick, CO). The LCVR is positioned between the sample collimator and a reflecting mirror in the sample path optics, and fast and slow axes are aligned with the PM fiber axes. The liquid crystal material birefringence depends on operating wavelength, drive voltage, and temperature. Assuming that wavelength and temperature remain constant during experiments, the LCVR yields maximum retardation between the polarization modes with no voltage applied, since liquid crystal molecules lie parallel to fused silica windows. When a voltage is applied to the LCVR terminals, the liquid crystal molecules tip perpendicular to the fused silica windows reducing the retardation. A 2 kHz square wave of adjustable amplitude is used for controlling the LCVR as described in its manual.

Figure 2.9 shows temporal response of the LCVR as well as the common mode rejection of the PS-OLCR phase noise. The LCVR drive signal is applied between 10 ms and 20 ms. The measured temporal response and retardation are in excellent agreement with the manufacturer specifications. Fluctuations in φ_1 and φ_2 due to environmental effects are common to each channel and greatly reduced in the differential phase ($\Delta\varphi$) signal.

Sensitivity of PS-OLCR is demonstrated by slightly altering the amplitude of the LCVR drive signal to induce very small path length changes. The differential phase signal is divided into four states each of which is 10 ms in duration. The first and last states are driven by the same voltage amplitude; hence,

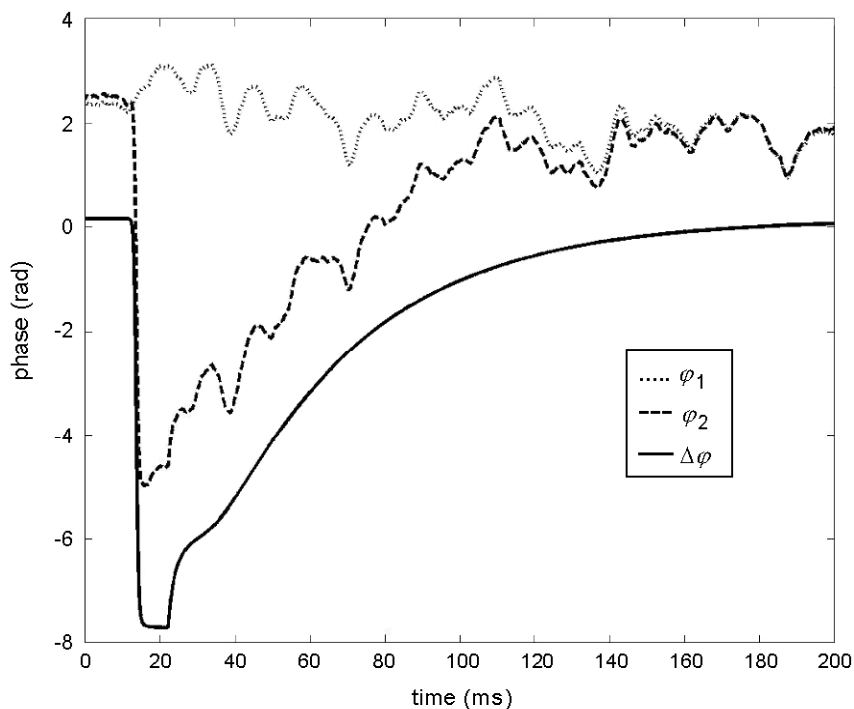


Figure 2.9: Temporal response of liquid crystal variable retarder measured by PS-OLCR. Noise on individual phase channels (φ_1 and φ_2) is removed from the differential phase signal ($\Delta\varphi$).

they are expected to have the same phase level. The induced phase changes can be predicted from Figure 2.10. In processing, a digital band-pass filter with 3 kHz pass-band region is used. Therefore, the temporal resolution is less than 1 millisecond.

The thick segment in the beginning of traces shown in Figure 2.10 is due to signal processing. This transient feature can be removed from data by filtering or a moving average, since it contains sinusoidal fluctuations at fringe frequency. Moreover, because of the processing artifacts, a few points in the beginning and

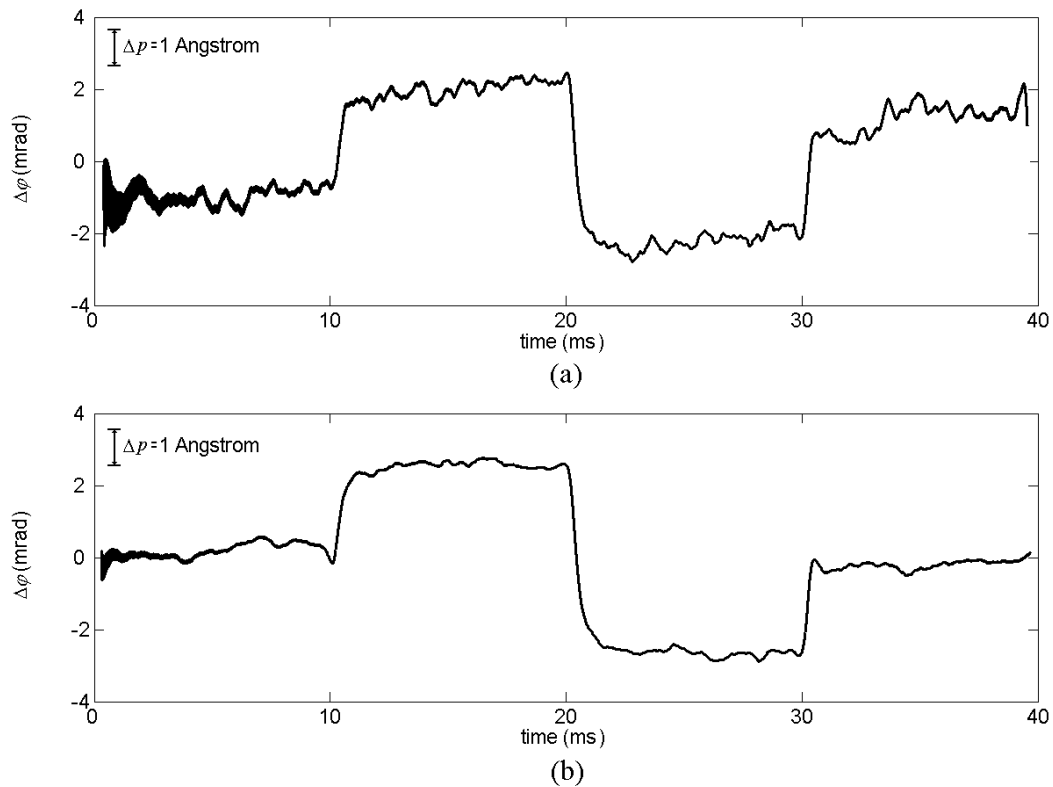


Figure 2.10: Phase sensitivity: (a) single record, and (b) average of 10 records. Averaging smoothes the noise.

end of the records are usually removed. Nevertheless, Figure 2.10a shows that phase sensitivity of an individual record is as low as 1 milliradian, which corresponds to optical path length change of nearly 1 Angstrom when the source wavelength is centered at $1.31 \mu\text{m}$ (2.8). Considering the environmentally induced single channel phase noise is about 1.5 radians (Figure 2.9), the differential phase measurement in PS-OLCR improves the phase sensitivity by three orders of magnitude (~ 30 dB) compared to the single channel

interferometers. Such a high common mode rejection allows sensitive PS-OLCR measurements. Furthermore, averaging over multiple records improves the minimum detectable signal. Averaging N records should improve the signal to noise ratio by a factor $N^{1/2}$. Figure 2.10b shows reduction of noise and a slow drift by averaging.

2.4.3 Environmental Perturbations

Environmental factors such as thermal drift, air currents, vibration and stress can induce optical path length change in the polarization channels. These environmental perturbations are greatly eliminated by common mode rejection of PS-OLCR. However, small residues of noise can be crucial in applications requiring Angstrom-level phase sensitivity.

In order to minimize the environmental effects, the fiber system is placed in a mechanical enclosure and optical components are protected from dust. When fiber movement is restricted, system performance to resolve smaller phase differences is increased. Protecting the sample fiber is important, because light propagates in both orthogonal channels. Because the reference fiber after the phase modulator carries both components (**f** and **s**) on the slow axis, any perturbation of this fiber segment result in equal shifts of the coherence functions and will be removed from the differential phase information.

Section 2.4.3.1 describes temperature-induced perturbations on PS-OLCR. Phase stability over a long period of time is demonstrated as well. Section 2.4.3.2 shows PS-OLCR performance with the presence of extreme mechanical vibration.

2.4.3.1 Temperature Variations

To assess dependence of system performance on temperature change, electric blankets are placed on top of an insulating box enclosing the PM fiber components. Depth scans of a sample mirror are acquired together with a thermocouple recording of the temperature inside the box, which is controlled by turning the electric blankets on (for 15 minutes) and off (for 35 minutes). Figure 2.11 illustrates the temperature in the box in which the fiber system is placed, the

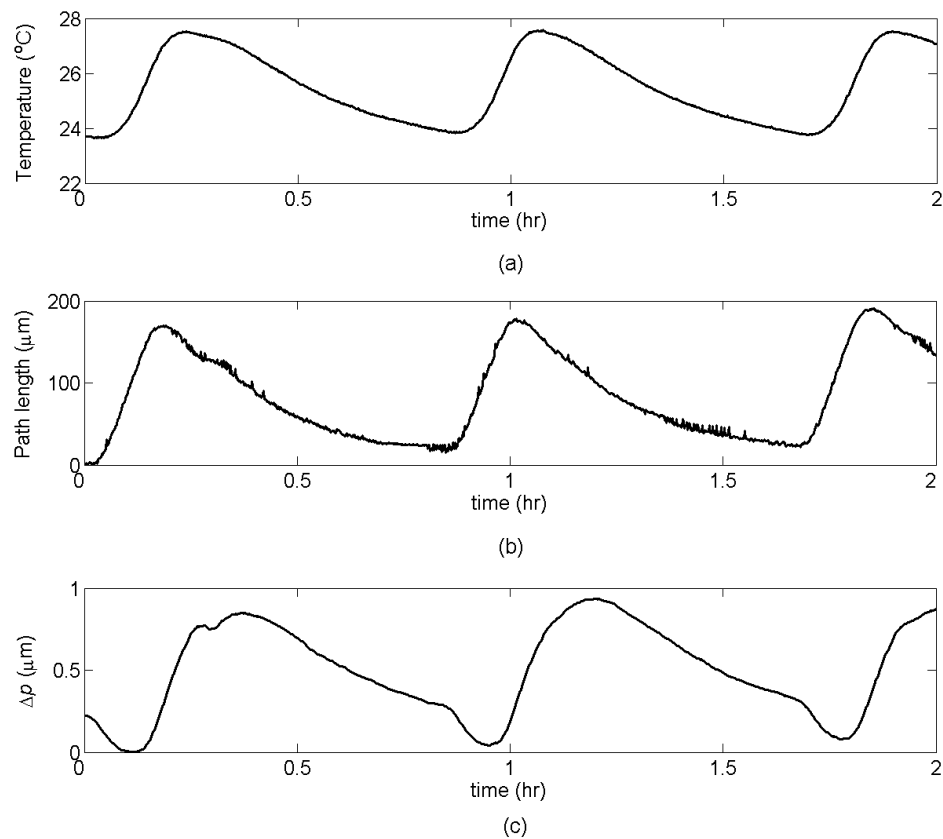


Figure 2.11: Perturbation of temperature change on the fiber system: (a) measured temperature in the box enclosing the fiber system, (b) axial shift of the coherence functions, and (c) relative movement of coherence functions (i.e., differential path length change).

corresponding shift of the coherence functions, and the change in differential path length (Δp). The shift in the coherence functions is measured by detecting the position of maximum value of the coherence function envelope in each depth scan. Relative movement of the coherence functions (Δp) is measured by calculating the phase difference between the two coherence functions.

In Figure 2.11, a temperature change of 4° C resulted in a 170 μm shift of coherence functions axially, and approximately 0.85 μm relative path length drift between the polarization channels. Magnitude of the temperature related drifts are believed to depend on the PM fiber length, mismatch between fiber lengths in reference and sample arms, and birefringence of the PM fiber segments.

Phase stability of PS-OLCR is demonstrated by continuous measurement of the system over an eight hour time period. Analysis of the acquired depth-scans of a sample mirror indicate that drift in differential phase signal ($\Delta\phi$) is less than a radian (Figure 2.12). The corresponding drift in the differential path length (Δp) is demonstrated on the right side of Figure 2.12. It should be noted that temperature change of the environment is normally a slow process. Because PS-OLCR yields very fast (in milliseconds) measurements, variations in environmental temperature are usually not problematic in many applications.

2.4.3.2 Vibration

Vibration is a common problem in optical interferometers. To test system resistance to mechanical vibrations, two audio speakers of 140 W each are placed on the optical table and faced toward the PS-OLCR system. While recording

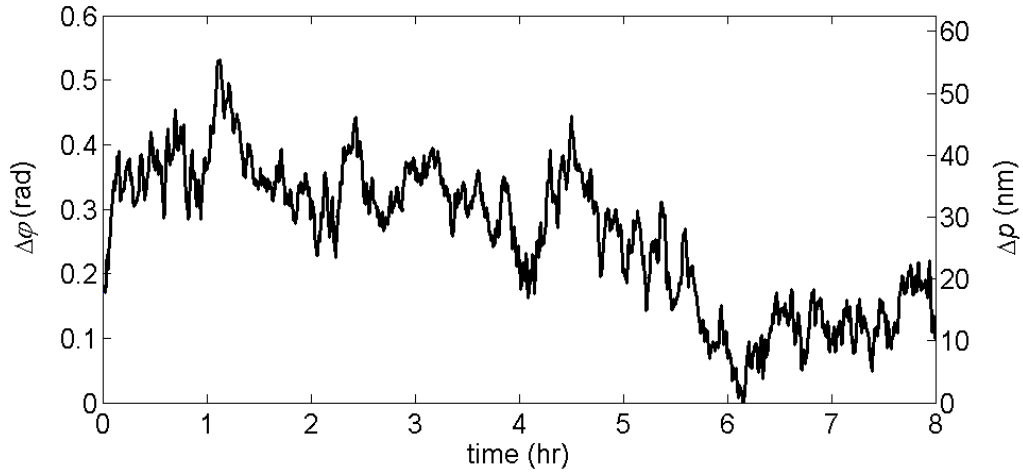


Figure 2.12: Long-term stability of the PS-OLCR.

sinusoidal fringes from a sample mirror with LiNbO_3 phase modulation, the speakers are driven by a 100 Hz sinusoidal signal at maximum amplitude. Figure 2.13 illustrates path length fluctuations of individual PS-OLCR channels and the perturbation on the differential path length (Δp). As shown in Figure 2.13, variation of individual path lengths ($\pm 8 \mu\text{m}$, peak-to-peak) due to vibration is largely reduced from the differential path length ($\pm 6 \text{ nm}$, peak-to-peak) by common mode rejection. Therefore, three orders of magnitude improvement ($\sim 30 \text{ dB}$) is obtained in the vibration related path length changes. This measurement also confirms the common-mode-rejection-ratio of PS-OLCR that is reported in Section 2.4.2.

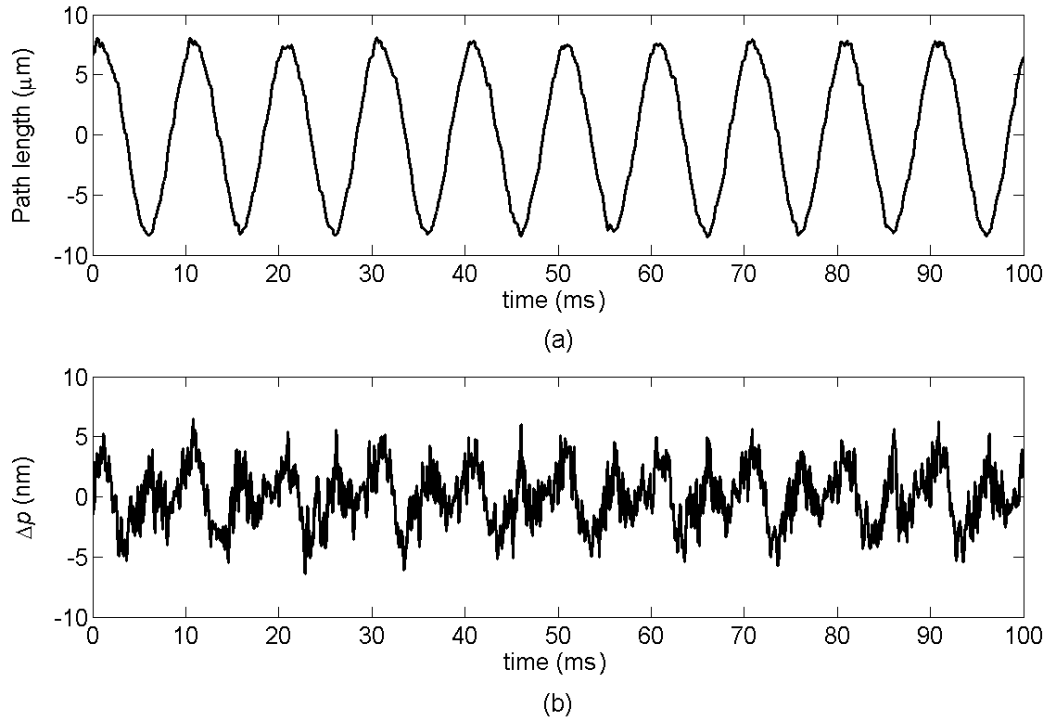


Figure 2.13: Common-mode rejection of mechanical vibrations: (a) individual path length fluctuations, and (b) change in differential path length.

2.5 DISCUSSION

Performance of PS-OLCR depends on many factors that require optimization. The environmental perturbations such as thermal drift and vibration are presented in Section 2.4.3. In the following subsections, I discuss polarization mode dispersion (Section 2.5.1), modulation scheme (Section 2.5.2) and ghost lines around the coherence functions (Section 2.5.3). Improvement of the PS-OLCR performance and solutions of ghost line problems are presented.

2.5.1 Polarization Mode Dispersion

Dispersion itself, if not compensated, can affect the phase difference along the coherence functions, especially when the two coherence functions are not overlapped perfectly. If the fast (or slow) channel experiences same dispersion in the reference and sample arms, the fast (or slow) channel is not affected from the dispersion. Correspondingly, minimum width of the coherence function in the fast (or slow) channel is achieved.

Dispersion imbalance between the polarization channels is described as polarization mode dispersion. In this case, the dispersion cannot be compensated independently for each channel by the RSOD. Because the polarization mode dispersion alters the relative shape and phase of the coherence functions in each channel asymmetrically, it affects the phase difference along the coherence functions.

Figure 2.14 shows a trend in the phase difference along the coherence functions. The ringing in phase difference is correlated with the fringe frequency, and can be reduced by filtering or a moving average window. When fringes are monitored by LiNbO_3 phase modulation, the working region within the coherence functions can shift slightly due to the environmental factors. The differential phase noise can be correlated to those individual phase/path length perturbations, if a phase trend is present along the coherence functions. Magnitude of differential phase noise depends on amount of the individual phase fluctuations, working region within the coherence functions, and corresponding polarization mode dispersion in that region.

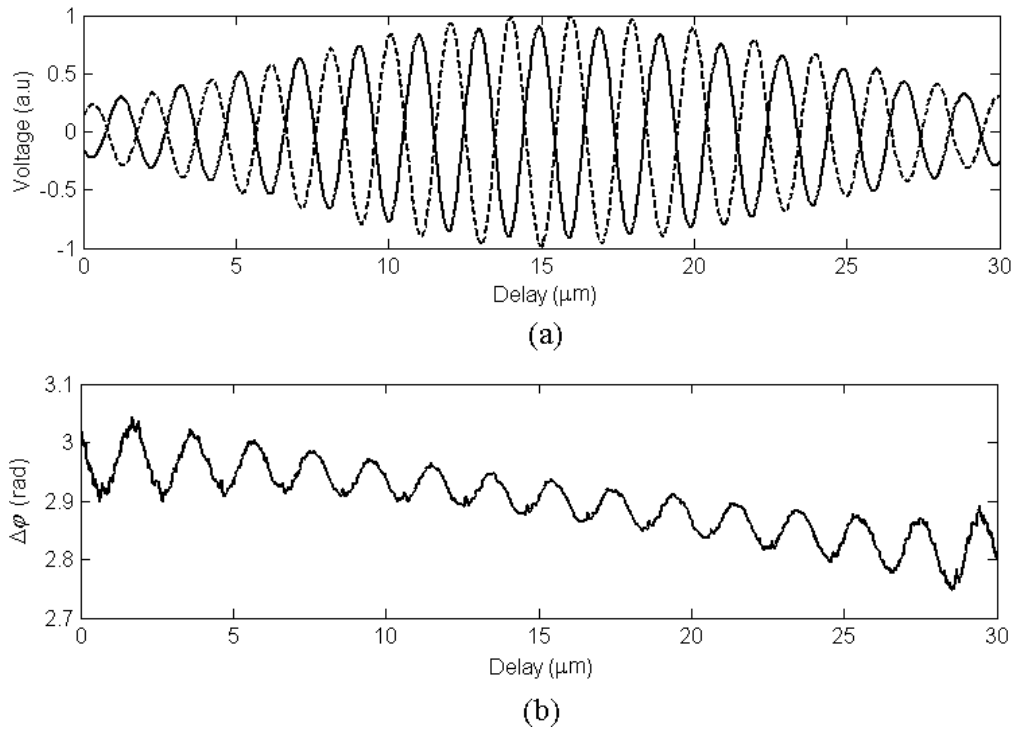


Figure 2.14: Coherence functions of the two PS-OLCR polarization channels (a), and a slope in phase difference along the coherence functions (b).

I noticed that changing the grating-lens separation in the RSOD alters the phase slope along the coherence functions. The grating-lens separation, which adjusts the dispersion compensation, is adjusted to reduce the phase slope. In this case, the PS-OLCR coherence functions may not necessarily have the minimum width. Also, an increase in intensity of input source light reduces the phase slope along the coherence functions. The reason is probably a reduction in spectral width of the source light associated with increased light intensity.

This section demonstrated the effects of polarization mode dispersion on the differential phase signal. The resulting perturbation on phase difference may be reduced by changing the grating-lens separation in the RSOD, or decreasing the spectrum width (depth resolution) of the broad band light source, or using PM fiber segments with similar beat lengths. Use of short PM fiber segments in the reference and sample arms should reduce the polarization mode dispersion, but ghost lines that are described in Section 2.5.3 may be more problematic.

2.5.2 Modulation Scheme

A slight imperfection of the sinusoidal fringes may be observed at the discontinuities of the saw-tooth waveform that drives the LiNbO₃ phase modulator. The amount of distortion depends on quality of the drive signal (sharp transitions), location of the transition in a fringe, and width and envelope of the coherence functions (usually Gaussian). If the photo-detector can detect higher frequencies, then a spike at the transition might be observed.

If fringes in both channels are superposed by a variable delay element such as a liquid-crystal variable retarder in the sample path, then effects of imperfect transition region, which is normally negligible, may be completely eliminated by the common mode rejection. Usually filtering in analog and digital domains removes the spike and smoothes the transition region, and sufficient to obtain almost perfect sinusoidal interference fringes.

2.5.3 Ghost Lines

Ghost lines are unwanted fringe patterns on or around the coherence functions. Depending on the cause, ghost lines may indicate unique features such as having or not having a mirror image on the opposite side of the coherence functions. Because ghost lines can cause misinterpretation of tissue structures, they are usually problematic in imaging applications. Hence, they must be removed or relocated far from the coherence functions.

The first PS-OLCR version (Davé *et al.*, 2001) we reported was not suitable for imaging applications, because of a significant number (~15) of ghost lines in the proximity of coherence functions. Therefore, an image of a single tissue layer was corrupted by approximately 15 additional layers. The magnitude of those ghost lines were as large as one tenth of the main layer limiting the signal to noise ratio (10 dB).

I simulated the expected ghost line patterns using a cross correlation technique, and found the sources of each ghost lines by comparing the simulations with experimental data. Then the ghost line sources are experimentally confirmed. The first version of the PS-OLCR contained a Lyot-depolarizer, which divides the power equally into the fast and slow axes with a 45° splice of the PM fiber in the source arm (Davé *et al.*, 2001). But, the Lyot-depolarizer was doubling the number of ghost lines in the interference pattern. Therefore, it is detached from the fiber system at the expense of slightly unequal powers between the channels. As an alternative, a polarizer can be placed in the input arm to

adjust powers coupled into the polarization channels. The remaining ghost lines are analyzed and relocated as described in the following subsections.

2.5.3.1 Ghost Lines Due to the Coupler

Since mixing of fast and slow components occurs equally at the 45° splice, interference of these projections with the cross coupling in the 2×2 PM coupler creates ghost lines. The ghost line may be displaced from the main coherence function by increasing the fiber length between the coupler and the 45° splice ($x_{c3}+x_{r1}$). Indeed, the separation depends on the beat length and actual length of the PM fiber segment. The beat length (2-3 mm) is the PM fiber length that induces one wavelength (λ) of delay between fiber channels.

2.5.3.2 Ghost Lines Due to the LiNbO₃ Phase Modulator

Similar to the previous case, interference between each projection of the 45° splice and cross coupling due to the LiNbO₃ phase modulator introduce a ghost line. The amount of cross coupling depends on misalignment of LiNbO₃ waveguide propagation axis with respect to the fiber axis. Stress applied to the PM fiber in fiber devices can contribute to cross coupling as well. The corresponding ghost line is one-sided, and can be displaced from the main fringe by choosing a longer fiber length of x_{r2} .

2.5.3.3 Ghost Lines Due to 90° Splice

Fiber axis misalignments and splicing process can yield cross coupling between the orthogonal channels. Analysis and experiments showed the 90° splice, which couples the slow channel into the fast channel and vice-versa, is crucial. In this case, the fiber length x_{s2} and its beat length determine the location of the corresponding ghost line. Length adjustments of the fiber segments may require additional splices, because to align the two coherence functions at the same spatial position, the condition in (2.5) must be satisfied.

2.5.3.4 Ghost Lines Due to Fiber Connectors

Another perturbation that may cause undesired fringe pattern is due to the sample fiber connector. Although fiber connectors make the system alignment easy, cross coupling between the orthogonal channels may occur. Such effect may be the result of non-uniform stress on the PM fiber applied by the connector. Unlike the previous types, the corresponding ghost lines are hidden in the main coherence function and decreases isolation of the channels.

The amount of cross coupling can be quantified by placing a polarizer in the sample path that blocks one of the fiber channels. An alternative way of seeing the cross coupling is to place two coherence functions at different locations by abandoning the condition given in (2.5), or to use the longitudinally displayed polarization channels by a pair of birefringent wedges (Figure 2.4c). In this case, the cross coupling term appears between the two main coherence functions. Since only one polarization mode propagates through the LiNbO₃ modulator, the

reference connector does not cause the same problem. The connector effect suggests that even if the polarization axis alignment is perfect in PM components (i.e. coupler and LiNbO₃ modulator), then the input/output ports of these fiber-based devices, which stabilize the fiber, may cause ghost lines.

2.6 CONCLUSION

PS-OLCR, which is a dual channel fiber-based differential phase interferometer, is described with nanometer accuracy and Angstrom sensitivity. Basic theory of optical low-coherence interferometry, PS-OLCR sample path configurations, signal processing and measurements demonstrating system phase accuracy and sensitivity are explained. Factors affecting system performance are stated together with experimental results and associated solutions. Common-mode-rejection of environmental perturbations in PS-OLCR is demonstrated for vibration and temperature change. Polarization mode dispersion, modulation scheme and a study of ghost lines in the interferometer design are discussed, and improvements in PS-OLCR performance are presented.

A well-characterized and optimized PS-OLCR is now available to investigate a variety of biomedical research problems. In the next chapters, PS-OLCR is applied to measurement of analyte concentrations, surface profilometry, measurement of tissue response to external stimuli, birefringence measurements and optical detection of neural activity. It is found that PS-OLCR has potential to aid engineers and scientists in investigating important phenomena in biomedical engineering and developing useful diagnostic and therapeutic imaging tools.

Chapter 3: Measurement of Analyte Concentrations

3.1 ABSTRACT

Measurement of analyte concentrations in a clear and turbid media is an important need in various biomedical assays. For instance, concentrations of physiological substances in blood such as glucose are directly related to health, and are reliable indicators of a patient's condition. An application of phase sensitive optical low-coherence reflectometer (PS-OLCR) for measuring analyte concentrations is studied. Methods with sub-milliMolar (sub-mM) sensitivity are introduced.

3.2 INTRODUCTION

Concentration or density of substances is one factor altering the refractive index of materials. Since commonly used refractometric systems are limited to clear or near-clear media and are not suitable for noninvasive applications, an accurate noninvasive technique capable of detecting ultra-small variations in refractive index in clear and turbid media is needed. Measurement of analyte concentrations in turbid media such as skin or blood is particularly important in assessing physiological conditions. For example, non-invasive measurement of glucose concentration is crucial, since estimated number of people suffering diabetes is more than 150 million and the current glucose sensing techniques involve a finger puncture for blood analysis. Optical techniques suggested for

non-invasive measurement of glucose concentration have limitations associated with low sensitivity and accuracy in the physiological range (3-30 millimolar).

Application of conventional OCT for noninvasive monitoring of blood glucose concentration in skin has been reported (Esenaliev *et al.*, 2001, Larin *et al.*, 2002, Larin *et al.*, 2003). These studies measure changes in tissue scattering coefficient and report that variation of glucose concentration changes the refractive index mismatch between the extracellular fluid and scattering centers in tissue and thereby affects tissue scattering properties. I have learnt from Dr. Larin that their approach could resolve 2-3 mM change in glucose concentration.

In this chapter, a highly sensitive method for measuring analyte concentrations is investigated with PS-OLCR. Phase shifts due to concentration changes of major body analytes are measured in clear media and turbid media. The samples used in the study are glucose, calcium chloride, magnesium chloride, sodium chloride, potassium chloride, urea, bovine serum albumin and bovine globulin solutions. The PS-OLCR measurements are compared with the values given in literature at visual wavelengths and found similar. Preliminary results demonstrated that sub-mM sensitivity in measurement of analyte concentrations is possible using a PS-OLCR measurement.

3.3 MATERIALS AND METHODS

Aqueous solutions used in this study are D-glucose ($C_6H_{12}O_6$), calcium chloride ($CaCl_2$), magnesium chloride ($MgCl_2$), sodium chloride ($NaCl$), potassium chloride (KCl), urea (CH_4N_2O), bovine serum albumin, and bovine γ -

globulin. Different concentrations of aqueous solutions are prepared by diluting stock chemicals (Sigma-Aldrich Chemical Corp, Bellefonte, PA) with pure water.

The sample solutions are injected into a glass cell having an inner wall separation of approximately 485 μm . Polarization channels are delayed by a pair of calcite wedges as previously described in Figure 2.4c, so coherence functions from front and back cell walls overlap with each other. After alignment of coherence functions, the longitudinal galvanometer in PS-OLCR reference arm is stopped, and sinusoidal fringes are produced by the LiNbO_3 phase modulator. In this way, the polarization channels monitor the front and back walls of the cell, simultaneously.

The interferometric fringes are recorded when the glass cell is filled first with water, and then with a known sample solution. The procedure is repeated five times for each concentration. Change in the phase difference ($\Delta\phi_{\text{sample}} - \Delta\phi_{\text{water}}$), which is proportional to the optical path length change (Δp) given in (2.8) or equivalently the change in refractive index of the sample, is measured. [$\Delta p = (n_{\text{sample}} - n_{\text{water}})t$; n - refractive index, t -inner wall separation of the cell].

Additional experiments are performed using aqueous suspensions of polystyrene microspheres (Bangs Laboratories, Inc., Fishers, IN) in glucose solutions. The polystyrene spheres have negligible absorption in the near-infrared spectral region, and simulate tissue scattering. Solutions of polystyrene spheres are useful for phantom studies because of the stability of their optical properties and simplicity to compute the scattering coefficient. The spheres had a diameter of 760 nm. Sphere concentrations were chosen according to the calculations

performed on the basis of Mie theory of scattering (Van de Hulst, 1981; Bohren and Huffman, 1983). Glucose concentrations with scattering coefficients of $\mu_s \cong 50 \text{ cm}^{-1}$ (a typical value for tissues in near-infrared spectral region) and $\mu_s \cong 100 \text{ cm}^{-1}$ are prepared at the PS-OLCR operating wavelength ($\lambda=1.31 \text{ }\mu\text{m}$). The reference water solutions are prepared with the same scattering coefficients. Therefore, experimental errors due to sphere concentrations are avoided [$\Delta\varphi=\Delta\varphi_{\text{glucose+water+spheres}}-\Delta\varphi_{\text{water+spheres}}$]. Polystyrene microsphere concentrations in the sample solutions were 0.8% and 1.6% (weight/ weight) for $\mu_s \cong 50 \text{ cm}^{-1}$ and $\mu_s \cong 100 \text{ cm}^{-1}$, respectively.

3.4 RESULTS

Phase shifts due to concentration change of major body analytes in translucent media are shown in Figure 3.1. While other analyte concentrations are given in mM, bovine serum albumin and globulin concentrations are in mg/dL as indicated in Figure 3.1d. Mean values of data (five measurements per a given concentration) are fit to a straight line by using a linear least-squares algorithm. Bars indicate standard deviation of the five measurements. Average standard deviation of phase in glucose measurements (Figure 3.1.a) is found to be 0.128 radians. The standard deviations of the PS-OLCR measurements can be greatly reduced by changing the experiment procedure to allow faster recording of data. Alternative methods are discussed in the next section.

Slopes of the straight lines in Figure 3.1 yield phase shift per unit concentration ($d\varphi/dC$). The $d\varphi/dC$ values and the corresponding refractive index

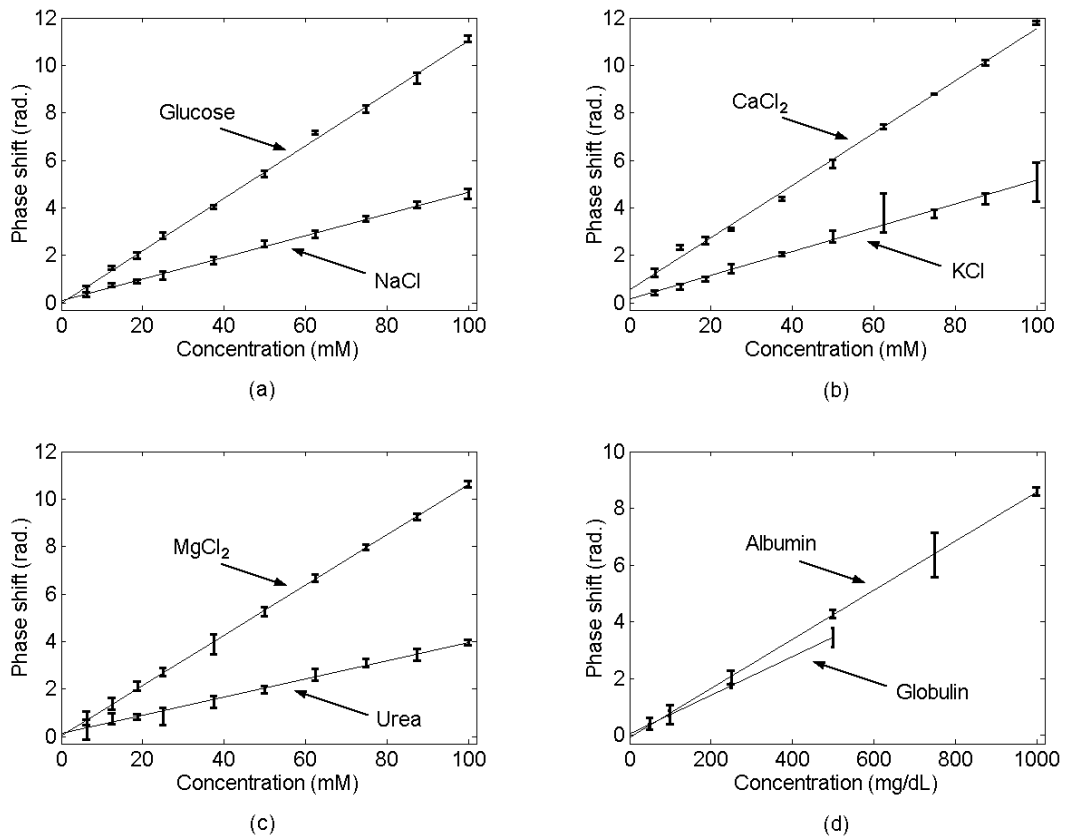


Figure 3.1: Phase shift due to concentration changes: (a) glucose and NaCl, (b) CaCl₂ and KCl, (c) MgCl₂ and urea, and (d) albumin and globulin. Straight lines are the linear fit using a least-squares algorithm, and bars indicate the standard deviation of the measurements.

changes (dn/dC) are given in the second and third columns of Table 3.1, respectively. The fourth column of Table 3.1 shows the previously reported changes in refractive indices per unit analyte concentration (dn/dC)_{lit} using white-light refractometers. The literature values are calculated from refractive index data obtained from Huglin (1972) for albumin and globulin ($\lambda=436$ nm), and Weast (1989) for other analytes ($\lambda=589$ nm).

Table 3.1 Phase shift ($d\phi/dC$) and refractive index change (dn/dC) per unit analyte concentration. dn/dC values are extrapolated from literature at visible wavelengths, physiological ranges, and corresponding maximum phase shifts are given. (*) $d\phi/dC$, dn/dC , and C_{physiol} values for albumin and globulin are in rad/(mg/dL), $\times 10^{-5}/(\text{mg/dL})$, and mg/dL, respectively.

Analyte	$\left[\frac{d\phi}{dC}\right]_{\text{exp}}$ rad/mM	$\left[\frac{dn}{dC}\right]_{\text{exp}}$ $\times 10^{-5}/\text{mM}$	$\left[\frac{dn}{dC}\right]_{\text{lit}}$ (visible) $\times 10^{-5}/\text{mM}$	$C_{\text{physiol.}}$ mM	$\Delta C_{\text{physiol.}} \times \frac{d\phi}{dC}$ rad
Glucose	0.1105	2.38	2.55	3-30	2.9835
CaCl ₂	0.1100	2.36	2.48	2.1-2.6	0.0550
MgCl ₂	0.1058	2.27	2.25	0.7-1.0	0.0317
NaCl	0.0456	0.98	0.98	135-145	0.4560
KCl	0.0501	1.08	0.96	3.5-5	0.0751
Urea	0.0382	0.82	0.85	2.9-8.9	0.2292
*Albumin	0.0087	0.19	0.20	0.35-0.45	0.0190
*Globulin	0.0068	0.15	0.19	0.26-0.41	0.0225

The experimental results performed at $\lambda=1310$ nm with the PS-OLCR are in good agreement with the values obtained from literature (3rd and 4th columns of Table 3.1). The slight difference between the two dn/dC values may be due to the wavelength and temperature dependence of refractive index. Concentration errors in the sample preparations may contribute to the difference, as well.

The fifth column of Table 3.1 shows normal reference laboratory values of physiological changes in concentrations of the substances (Kratz and Lewandrowski, 1998). Multiplication of the measured phase change per concentration ($d\phi/dC$ values in the 2nd column) and the reported physiological range (5th column) results in the maximum possible influences of these substances on the phase measurement (the last column). The effect of glucose found to be considerably greater than the other analytes studied.

The method is experimentally tested in scattering media. Since scattering reduces light back reflected from deeper regions, the sample beam is focused on the back wall of the cell. Five glucose concentrations from 20 mM to 100 mM are prepared with aqueous suspension of polystyrene microspheres yielding scattering coefficients of $\mu_s \cong 50 \text{ cm}^{-1}$ and $\mu_s \cong 100 \text{ cm}^{-1}$. Because the amount of reference water solution prepared with microspheres was not sufficient, the experimental procedure was slightly altered. Instead of five consecutive measurements of water and glucose solutions, the order of recording was changed to [G W G G W G G], where G and W represent glucose and reference water samples, respectively. Consequently, the phase data obtained from glucose solutions were compared with the closest reference water measurement [$\Delta\phi = \Delta\phi_{\text{glucose+water+spheres}} - \Delta\phi_{\text{water+spheres}}$]. This change in experimental procedure is believed to increase experimental errors and standard deviations of the measurements.

Figure 3.2 shows phase shifts due to concentration changes in scattering media. The $d\phi/dC$ values calculated from the linear fits are found to be 0.1010

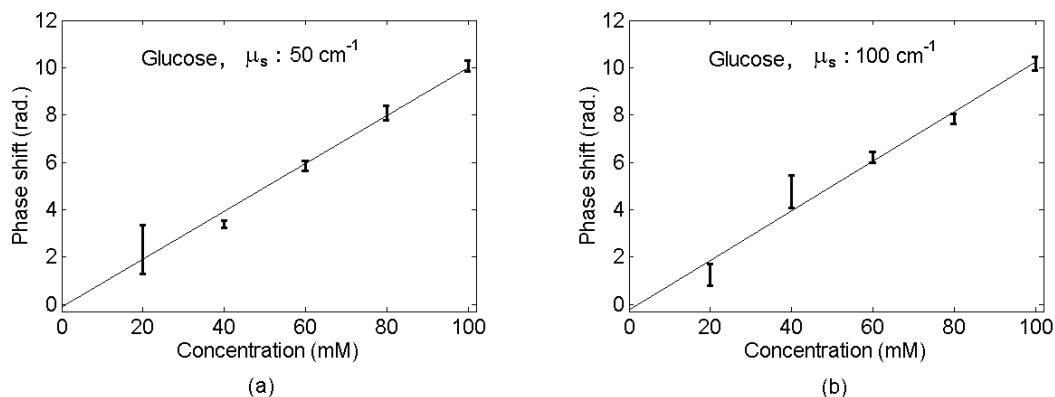


Figure 3.2: Phase shift due to change in glucose concentrations in scattering media with scattering coefficients of (a) $\mu_s \cong 50 \text{ cm}^{-1}$ and (b) $\mu_s \cong 100 \text{ cm}^{-1}$. Straight lines are the linear fit using least-squares algorithm, and bars indicate standard deviation of the measurements.

radian/mM and 0.1047 radian/mM for $\mu_s \cong 50 \text{ cm}^{-1}$ and $\mu_s \cong 100 \text{ cm}^{-1}$, respectively. The linear slopes in Figure 3.2 are similar to that of the clear media (0.1105 radian/mM), as well. These results indicate that applicability of this technique for sensing and monitoring analyte concentrations in scattering media is feasible.

3.5 DISCUSSION

In Chapter 2, I demonstrated that phase resolution of PS-OLCR is approximately 1 milliradian. Considering the $d\phi/dC$ values in Table 3.1, the system phase resolution can easily yield sub-mM sensitivity in analyte concentration measurements. Therefore, the standard deviations shown in Figure 3.1 and Figure 3.2 do not reflect the system sensitivity. Factors contributing to errors are mainly due to the experimental procedure, which requires replacement

of water (reference measurement) inside the glass cell with the sample solution. Because the time between the two measurements was nearly 30 s, the slow drift in phase difference due to environmental factors (see Section 2.4.3) and temperature dependence of refractive index of sample undermined the expected system performance.

PS-OLCR allows fast measurements on the order of milliseconds; therefore, the perturbation can easily be removed by scanning a dual-channel cell, which contains a reference (water) and sample solutions. If these sub-cells are positioned laterally, scanning of the sample or sample beam(s) is required. An alternative cell design may include two longitudinally placed cells. In this case, scanning the reference galvanometer may be adequate. Cells having micro-fluidic type channels may be used for stable measurements. Furthermore, it is noticed that the glass cell used in the experiments did not have perfectly parallel surfaces, which can result in path length variations due to mechanical bumps during the injection process.

Although physiological range and refractive index change per unit concentration of glucose may yield larger phase shifts than the other analytes, the measurement may be problematic in areas having different combination and concentration of analytes. If glucose or any other analyte is selectively excited by a stimulus such as light at a specific wavelength causing absorption in the analyte, then temperature induced refractive index change may be a good candidate to determine the analyte concentration in the complex tissue structures.

3.6 CONCLUSION

This chapter demonstrated the feasibility of using PS-OLCR to detect small path length differences due to concentration change of analytes in clear and turbid media. Translucent solutions of glucose, calcium chloride, magnesium chloride, sodium chloride, potassium chloride, urea, bovine serum albumin and bovine γ -globulin are used. Glucose experiments were repeated in scattering media for two different scattering coefficients, $\mu_s \cong 50 \text{ cm}^{-1}$ and $\mu_s \cong 100 \text{ cm}^{-1}$, and the results demonstrated applicability of the technique in tissues. The results obtained from several analytes are consistent with the results previously reported in literature. Moreover, results obtained from scattering media indicate that PS-OLCR performance in turbid media (i.e. tissue) is feasible.

Considering the physiological range (3-30 mM) and refractive index change per unit concentration ($2.38 \times 10^{-5} / \text{mM}$), the change in glucose concentration may dominate the change in other analyte concentrations given in Table 3.1. Hence, the technique may be used for direct measurement of glucose levels in tissue. In conclusion, the differential phase measurement provides a noninvasive, high sensitive (sub-mM), and accurate tool to monitor analyte concentrations, and has potential use in clinical studies.

Chapter 4: Imaging Surface Topography

4.1 ABSTRACT

Imaging surface characteristics yields important information about surface quality and defects in materials. Phase sensitive optical low-coherence reflectometer (PS-OLCR) with its dual-beam differential phase operation is presented for non-contact characterization of surface structures. Nanometer scale features on chromium film samples are imaged with PS-OLCR.

4.2 INTRODUCTION

Non-contact methods of imaging surface topography are essential in many applications. Since stylus-profiling techniques may be deleterious to the surface, alternative instruments have been developed. Non-contact techniques for measuring surface roughness include the scanning electron microscope, light scattering, light sectioning, and various interferometric techniques, such as fringes of equal chromatic order, Nomarski and differential interference contrast, Tolansky multiple beam interferometry, and two-beam interferometry based on Michelson, Linnik, and Mirau (Bhushan *et al.*, 1985). A survey on techniques for surface roughness measurements can be found in Bhushan *et al.*, 1985.

In this chapter, differential phase measurement of PS-OLCR for imaging surface topography is demonstrated. Images of chromium film surfaces are acquired with nanometer scale sensitivity. Measurement of discontinuities on

surface topography and extension of the technique to image biological structures are discussed.

4.3 MATERIALS AND METHODS

The sample path configuration in Figure 4.1 illustrates lateral scanning of a sample surface with two spatially separated PS-OLCR beams. While one beam scans a flat reference surface the other beam scans the sample surface to monitor topographic information. When fringes are formed by light reflecting from the sample surface, path length in the reference arm of the interferometer (depth-scan) is fixed and not scanned. The LiNbO_3 phase modulator produces the interferometric fringes. Calculation of the path length difference (Δp) from the differential phase data using (2.8) yields nanometer scale surface variations on the sample.

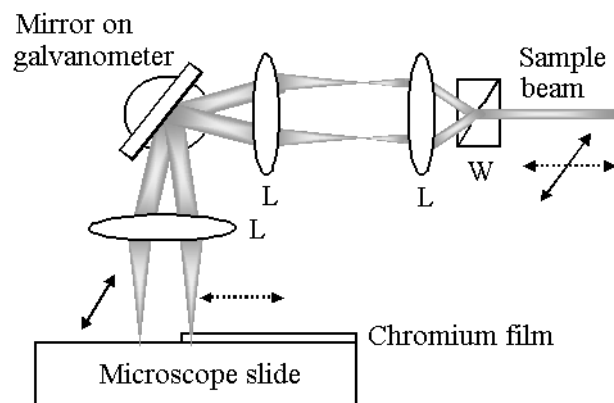


Figure 4.1: Sample path configuration to scan spatially separated polarization channels laterally on the sample, where L- lens, W-Wollaston prism, and arrows indicate polarization states.

Two samples consisting of nanometer scale surface features are prepared. The first sample is a thin chromium film layer deposited on one part of a microscope slide. Using the galvanometer scan shown in Figure 4.1, PS-OLCR measures surface variations on the transition region of the chromium film sample.

The second sample consists of two chromium film layers. After depositing a thin chromium film layer on a glass substrate, a second layer of chromium is deposited on one half of the sample to obtain a chromium-chromium step. The sample is used in the accuracy measurement (Section 2.4.1), as well. In addition to the galvanometer scan, a motorized stage that translates the sample orthogonal to the galvanometer scan direction is used. Therefore, three-dimensional image of the surface topography is recorded.

4.4 RESULTS

Figure 4.2 demonstrates a line scan indicating three regions, which are (i) both beams from the glass portion of the microscope slide, (ii) the probe beam tracing the chromium film while the other beam still reflecting from the microscope slide, and (iii) both beams from the chromium film layer. Beam separation on the sample was 550 μm . The dashed ovals in Figure 4.2 indicate the same surface variation of the transition region; however, one is inverted because of the negative sign in differential phase calculation ($\Delta\varphi = \varphi_2 - \varphi_1$).

Figure 4.2 also points out an issue in dual beam experiments. In these experiments, having the reference and probing beams on the sample may cause errors in the interpretation of results. This may happen, if the reference beam is

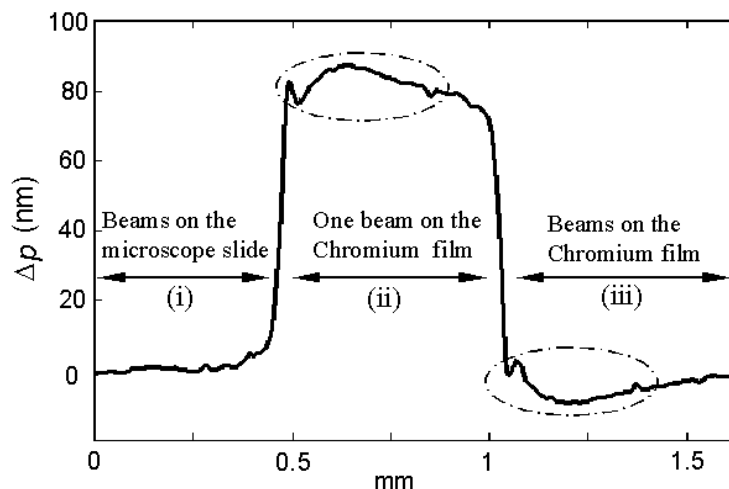


Figure 4.2: Surface features on a chromium film. The dashed ovals indicate the same feature in the transition region. One is inverted due to the negative sign in differential phase calculation.

affected unexpectedly during the measurements (i.e., a swelling may be identified as a shrinkage). Therefore, the reference beam reflected from a fix surface can eliminate confusions, and help better understanding of mechanisms.

Figure 4.3 shows a three-dimensional image of a chromium-chromium step. Separation of the laterally displaced beams was 1.14 mm, and only one of the beams passed over the step. Lateral scans of 800 μm were provided by the galvanometer scan, while a motorized stage under the sample was moving slowly ($\sim 100 \mu\text{m/s}$). Duration of the recording was 0.8 s. PS-OLCR channels with 50 kHz interference fringe frequency were acquired at 5 Ms/s sampling rate. In Figure 4.3, not only the step ($\sim 150 \text{ nm}$), but also smaller surface features in the order of 10 nm are visible. An Atomic Force Microscope confirmed the measured step height (Section 2.2.4.1) and the existence of smaller surface features.

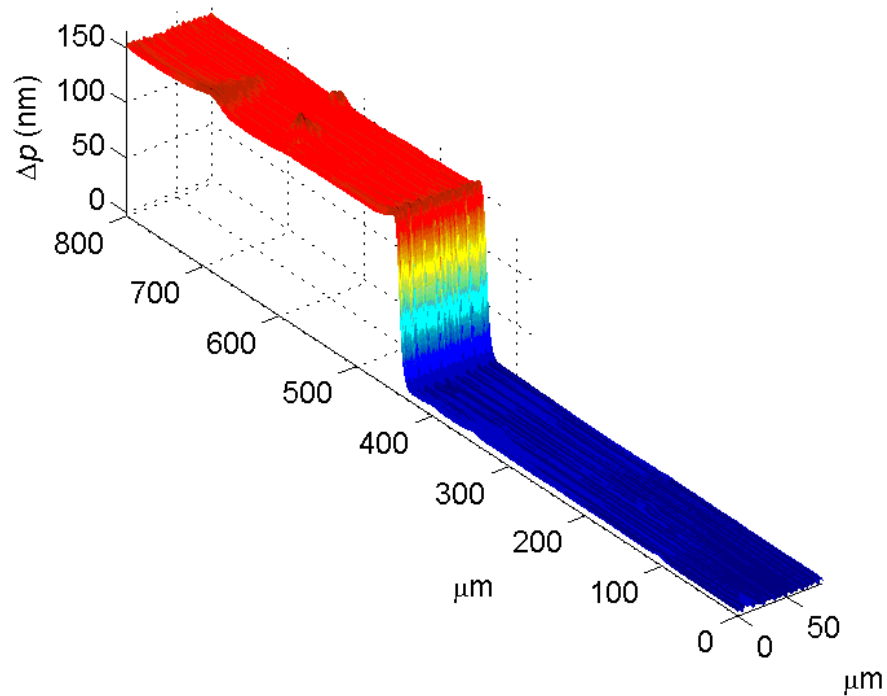


Figure 4.3: Three-dimensional image of a chromium step (~ 150 nm). Smaller surface features in the order of 10 nm exist.

4.5 DISCUSSION

Step like discontinuities on the sample may be problematic if the step height is greater than $\lambda/4$ (327.5 nm). A path length of $\lambda/4$ corresponds to π radians (2.8). Since one is unable to distinguish between $+\pi$ radian and $-\pi$ radian, the phase extraction algorithm can yield errors. For example, a step height of $+400$ nm would result in a computed height of -255 nm, which is within $\pm\lambda/4$. In this case, $\lambda/2$ (equivalently 2π radians) needs to be added to find the real step height. If the range of step height is an unknown, a depth scan should be recorded to obtain the number of phase wraps and wrapping direction. While phase

difference of interferometric fringes in the coherence functions is used for high resolution, the envelopes can be cross-correlated to determine how many times $\lambda/2$ needs to be added/subtracted. The problem exists only when sharp steps greater than $\lambda/4$ exist.

An alternative imaging setup can be constructed by delaying the two polarization channels longitudinally. In this case a reference glass surface is positioned just above the sample. Such an arrangement is employed for monitoring surface displacements described in the next chapter. Three-dimensional images can be acquired faster by replacing the motorized stage with an additional galvanometer.

The technique may be applied to bio-structures and biomaterials. Existence of multi-layer structures within the small coherence volume might affect the PS-OLCR phase signal. However, specular reflection of the top surface usually dominates the interference signal contributed by inner boundaries, which makes surface analysis of biological samples feasible.

4.6 CONCLUSION

Differential phase measurement using PS-OLCR is demonstrated for surface characterization of chromium film samples. The experimental results suggest that non-contact measurement of surface topography is accessible with nanometer scale sensitivity. Lateral resolution of the images depends on the beam diameter, and can be enhanced by using high NA lenses in combination with shorter wavelength sources.

Chapter 5: Cartilage Surface Response to Electrical Stimulation

5.1 ABSTRACT

Tissue response to thermal, electrical or chemical stimuli is important in the health and survival of tissue. In this chapter, surface displacement of cartilage tissue in response to electrical stimuli is explored. Dependence of cartilage response on the stimulus amplitude and frequency is studied. Experimental results demonstrate that phase sensitive optical low-coherence reflectometer (PS-OLCR) has potential use to monitor tissue response for diagnostic applications.

5.2 INTRODUCTION

Osteoarthritis, a common pathology in cartilage, is characterized by progressive loss of articular cartilage. In osteoarthritis, loss of proteoglycans decreases the ability of cartilage to withstand compressive loading and results in a tissue that is softer and more susceptible to wear and fibrillation (Maroudas, 1979; Grodzinsky, 1983). Many mechano-electrochemical phenomena in cartilage such as anomalous osmosis and electro-osmosis, ion-induced swelling, and streaming potential and current are attributed to the electrostatic and frictional interactions between the fixed charged groups and mobile ions (Sun *et al.*, 1999).

Electrokinetic transduction in cartilage has its origin in the fixed charged groups, primarily the proteoglycans. Either mechanical deformation or streaming fluid tends to separate the mobile ions from the fixed negatively charged groups.

This charge separation creates an electric field collinear to the fluid flow and proportional to the fluid velocity in the extra cellular matrix. Conversely, when a current-generated stress is applied to cartilage, an applied electric field can exert a force on the ionic space charges in the fluid phase and produce concomitant electrophoretic motion of the proteoglycans. These electroosmotic and electrophoretic effects can cause mechanical deformation and stress in the tissue.

Since an electric field applied to cartilage creates current-generated stress and deformation, measurement of surface displacement in stimulated cartilage may be a reliable indicator of cartilage viability. Electromechanical surface analysis providing a measure of cartilage material properties has been presented by measurement of current-generated stress using a piezoelectric sensor positioned against the cartilage surface (Berkenblit *et al.*, 1994). Non-contact measurements of the surface displacements can be achieved by using the PS-OLCR. The system has been used to study displacements in the infrared-sensitive thoracic pit organ of *Melanophila acuminata* (Hammer *et al.*, 2002).

In this chapter, non-contact measurements of surface displacements resulting from electrokinetic response of electrically stimulated cartilage are demonstrated by using the longitudinally displaced PS-OLCR channels. Cartilage response to different stimulus amplitudes and frequencies are studied. The results reported in this chapter have been published (Akkin *et al.*, 2003), and a related study with laterally displaced PS-OLCR channels by Youn *et al.* (2004) is accepted for publication.

5.3 MATERIALS AND METHODS

A pair of platinum stimulation electrodes (a conductive biocompatible material) is inserted in freshly harvested porcine nasal cartilage. The electrodes are 1.5 mm in diameter and separated by approximately 3 mm (center to center). An electrical function generator supplying sinusoidal output for stimulation is connected to the electrodes.

Figure 5.1 illustrates the experimental setup for measuring surface displacements in electrically stimulated cartilage. The PS-OLCR sample path configuration of longitudinally displaced channels was described in Section 2.3.2, and also used in Chapter 3. A pair of birefringent wedges delays the two polarization channels (arrows) longitudinally. The two channels are delayed so that PS-OLCR monitors a reference glass and cartilage surfaces simultaneously. The LiNbO_3 phase modulator provides interference fringes of 50 kHz that are acquired at 5 Ms/s sampling rate. The records are equally divided into 1000 segments each of which consists of 0.2 ms recordings. Each data segment yielded a single value of phase difference. No digital filters are used in signal processing.

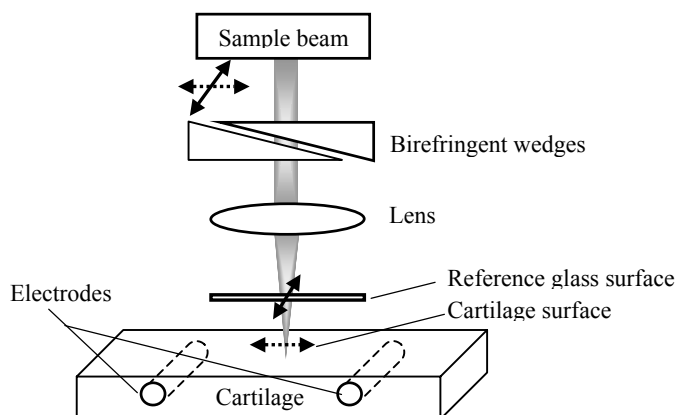


Figure 5.1: Experimental setup used in surface displacement of cartilage.

5.4 RESULTS

Three different stimulation frequencies (1 Hz, 0.5 Hz and 0.2 Hz) with two different voltage amplitudes (5 Volts and 10 Volts) are applied to cartilage. Figure 5.2 and Figure 5.3 show surface displacements in electrically stimulated cartilage. Dashed lines in the figures represent sinusoidal stimulation waveforms with arbitrary amplitudes.

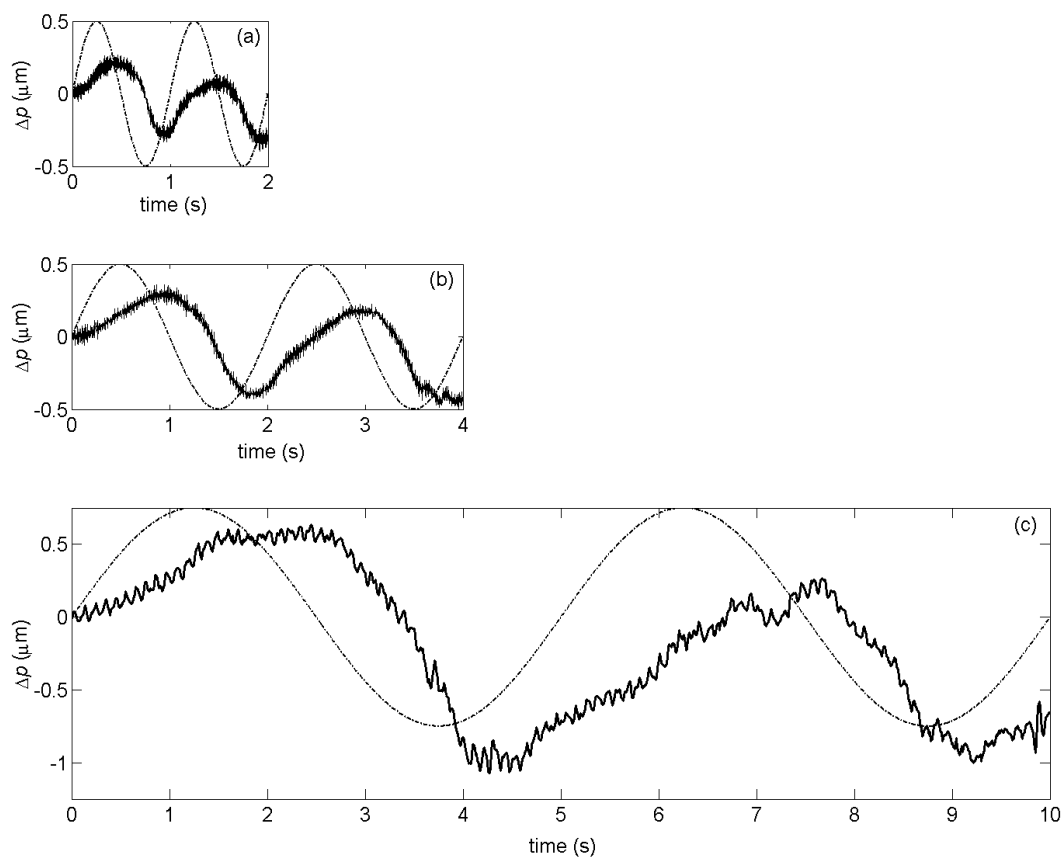


Figure 5.2: Surface displacements of electrically stimulated cartilage. Stimulation amplitude: 5 V, stimulation frequencies: (a) 1 Hz, (b) 0.5 Hz, and (c) 0.2 Hz. Dashed lines indicate the stimuli with arbitrary amplitudes.

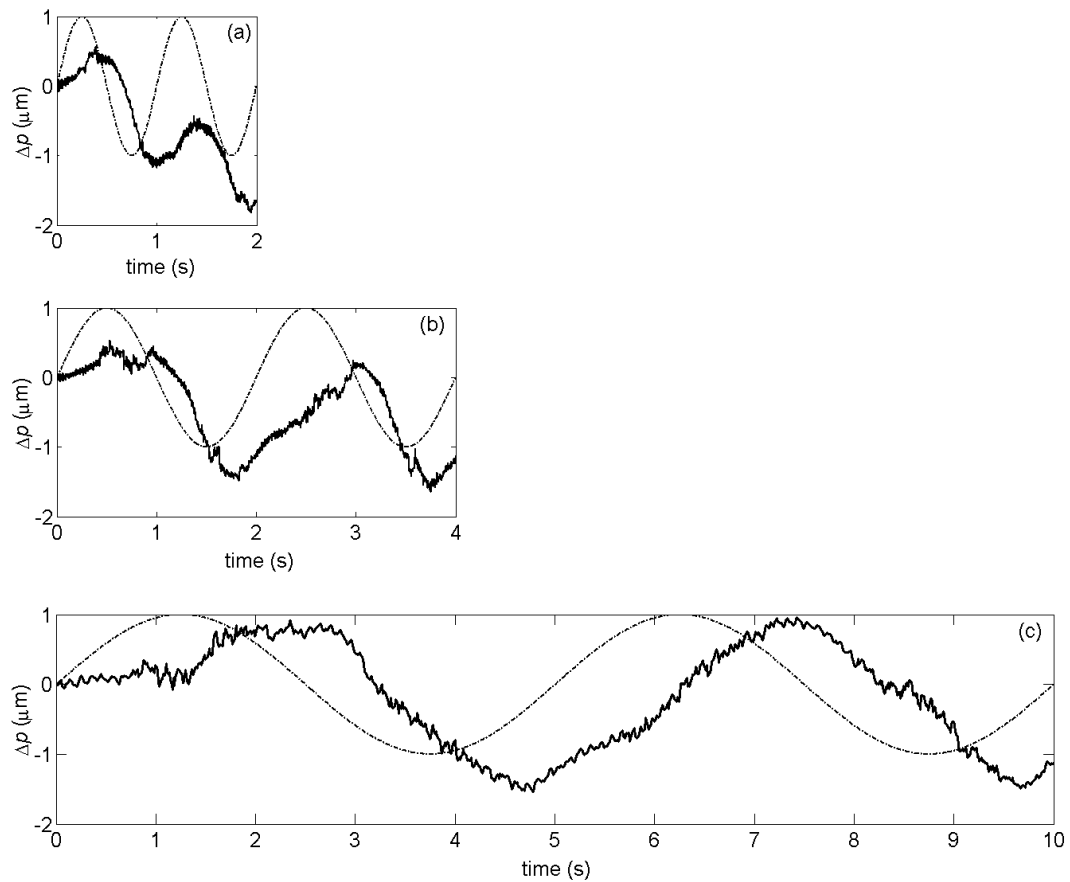


Figure 5.3: Surface displacements of electrically stimulated cartilage. Stimulation amplitude: 10 V, stimulation frequencies: (a) 1 Hz, (b) 0.5 Hz, and (c) 0.2 Hz. Dashed lines indicate the stimuli with arbitrary amplitudes.

Maximum surface displacements occurred around the zero-crossings of the electrical stimulation, when the polarity of the electrodes changes. The plots clearly show that lower stimulation frequencies cause larger surface displacements that are probably due to a longer integration. The gradual decrease in the cartilage surface level indicates shrinkage. The shrinkage may be due to

dehydration caused by an Ohmic temperature increase in the electrically stimulated cartilage. Moreover, an increase in stimulus amplitude resulted in larger displacements (Figure 5.3). These findings of cartilage surface displacement are consistent with the experimental and theoretical results demonstrated by Frank and Grodzinsky (1987a), Frank and Grodzinsky (1987b), and Berkenblit *et al.* (1994).

5.5 DISCUSSION

Since surface displacement of cartilage depends on stimulation frequency, a pulsed or chirped waveform consisting of stimulation frequencies may be applied for frequency domain analysis of the cartilage response. To deliver electrical current to cartilage, surface contact electrodes are preferred to needle electrodes. But, electrical stimulations of cartilage may not be desired in clinical applications due to safety considerations and invasive nature of electrodes.

Application of laser pulses that generate photothermal related changes in tissue is suggested as an alternative stimulation method. For instance, the next chapter presents laser-induced changes in arterial tissue. Temperature rise due to the absorption of laser pulses can induce stress and deformation in cartilage. The measurement of cartilage surface response using laterally displaced PS-OLCR channels does not require a reference glass surface, and deals with relative displacement between two laterally distinct points on the cartilage surface. Another application in stimulated cartilage could be the measurement of stress-induced birefringence change, which suggests a PS-OLCR single beam operation.

5.6 CONCLUSION

In cartilage, lower frequency and higher amplitude electrical stimulation produced larger surface displacement. Experimental results suggest PS-OLCR can measure transient variations of tissue surface deformation with nanometer scale sensitivity. Because of the non-contact measurements, the technique may allow non-invasive or minimally invasive evaluation of cartilage viability.

Chapter 6: Arterial Tissue Response to Photothermal Stimulation

6.1 ABSTRACT

An intensity modulated laser beam with emission wavelength absorbed by specific tissue chromophores can stimulate tissue. In this chapter, laser-induced photothermal changes inside arterial tissue are investigated. Nanometer scale path length changes between two points in arterial tissue in response to photothermal stimulation are measured.

6.2 INTRODUCTION

Accurate detection of vital arterial plaques may require an imaging technique that monitors a thin fibrous cap overlying a large lipid core and measures mechanical properties of the plaque. Optical techniques that provide micrometer depth resolution are promising methods to detect plaque. Fiber-based construction of such instruments can allow in-vivo applications using endoscopic fiber probes.

Arterial response to photothermal stimulation can be useful in assessing tissue health, particularly for atherosclerosis. Absorption of laser radiation results in a localized temperature increase that stimulates photothermal response of tissue. Analysis of laser-induced photothermal response can provide important information about optical and thermal laser-tissue interactions, which may be used in diagnostic and therapeutic applications.

Pulsed photothermal radiometry was used to measure, *in vitro*, the optical absorption of normal and diseased human artery at four wavelengths (308, 351, 488, and 532 nm) (Long and Deutsch, 1987). Mathematical models to predict temperature rises in biological tissue including normal human aorta has been investigated during laser irradiation by comparing calculated values with experimental measurements in which surface temperatures were monitored with an IR camera (Torres *et al.*, 1993). A more detailed description of optical and thermal response of laser-irradiated tissue can be found in the book edited by Welch and van Gemert, 1995.

In this chapter, rabbit arterial tissue with a plaque buildup on the arterial wall is stimulated *ex-vivo* by periodically modulated laser radiation at the wavelength of 532 nm. First, the PS-OLCR produced depth-resolved intensity images to detect location of the plaque. Then, the desired regions of tissue are probed by recording PS-OLCR differential phase measurements. Due to laser excitation, small variations in the optical path length between two points in the arterial tissue are detected. The experimental results, which have already been published (Akkin *et al.*, 2003), demonstrate that the PS-OLCR provides a non-invasive, depth-resolved and highly sensitive tool to identify laser-induced thermal changes in tissues. Additional work by Telenkov *et al.* that uses differential phase system to detect depth-resolved photothermal response in tissue (hair and rodent skin) will be published in 2004.

6.3 MATERIALS AND METHODS

To induce arterial plaques, a rabbit was fed a high cholesterol diet for 120 days. After harvesting tissue from the rabbit, the sample is placed on a motorized stage for lateral scanning. The luminal site was facing upwards. If galvanometer in the PS-OLCR reference arm is scanned while the motorized stage moves the sample, the resulting image will show depth resolved cross-sectional features in the arterial tissue. After precise determination of plaque location using PS-OLCR intensity images, desired regions of the tissue are probed by differential phase measurements.

Figure 6.1 illustrates the experimental setup used for detecting photothermal response of an atherosclerotic rabbit artery due to laser excitation. The periodically modulated laser radiation at the wavelength of 532 nm is used for stimulation. The excitation light having a power of 170 mW is focused on a

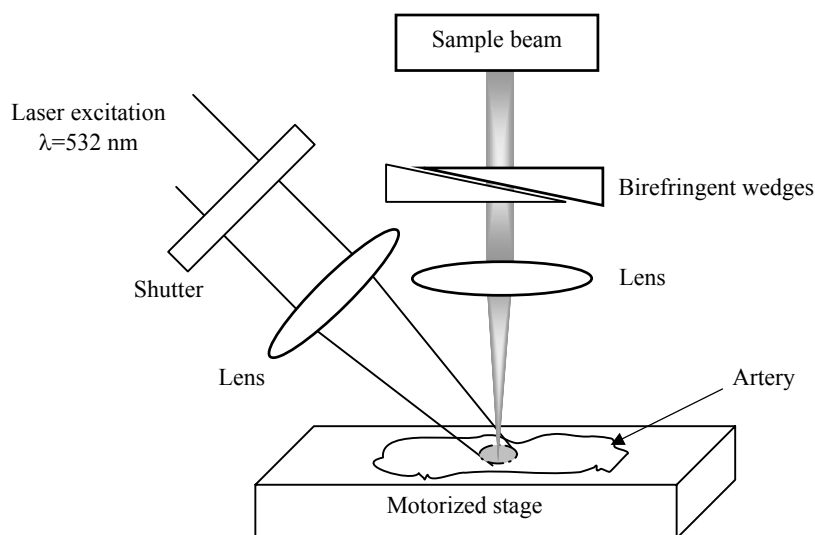


Figure 6.1: Experimental setup used in measurement of photothermal response of an atherosclerotic artery.

large spot (2 mm in diameter), and modulated at 1 Hz by a mechanical shutter. The sample path configuration of longitudinally displaced PS-OLCR channels was described in Section 2.3.2, and used in Chapter 3 and Chapter 5. Birefringent wedges in Figure 6.1 are aligned with the PM fiber axes to delay the two polarization channels longitudinally. Therefore, the system can monitor two longitudinally separated points inside the tissue, allowing detection of small optical path length variations between those two points by the differential phase measurement.

6.4 RESULTS

Figure 6.2 illustrates a depth-resolved cross-sectional image of an ex-vivo thoracic artery of a rabbit using amplitude demodulation of a PS-OLCR channel.

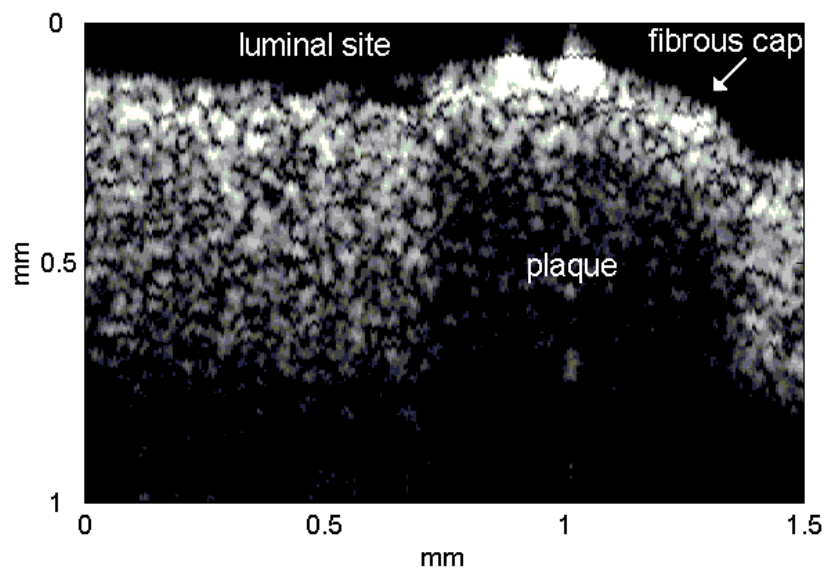


Figure 6.2: Depth resolved intensity image of an atherosclerotic rabbit artery.

Because the rabbit was on a high cholesterol diet, a fibrous cap and a plaque buildup underneath are visible. After recording the cross-sectional image (Figure 6.2), differential phase measurements from two regions, one from healthy area and the other above the plaque, are performed.

Figure 6.3 illustrates nanometer scale variations in the individual ($p1$, $p2$) and differential (Δp) path lengths between two points in the arterial tissue in response to laser stimulation. Path lengths denoted by $p1$ and $p2$ are simultaneously recorded from 100 μm and 200 μm below the luminal surface, respectively. The rectangular waveforms in Figure 6.3 indicate the shutter modulation where positive cycles represent stimulation by the laser excitation.

Experimental results, one from healthy area (Figure 6.3a and Figure 6.3b, $x=0.5$ mm, where x indicates the horizontal axis in Figure 6.2) and the other above the plaque (Figure 6.3c and Figure 6.3d, $x=1$ mm), show that optical path lengths of individual channels vary about 500 nm per excitation. However, differential path length changes between the two longitudinal points are less than 100 nm. Thermal expansion and refractive index change contribute to the magnitude of path length variations. The slow decay in individual path length plots may denote shrinkage due to dehydration of the arterial tissue. Because the upper channel ($p1$) is affected more from the shrinkage, the differential path length plots (Δp) have the similar trends, meaning that $p1$ and $p2$ are slowly getting closer. It should be noticed that environmental noise, which are present in the individual path lengths, are cancelled in the differential path length curves.

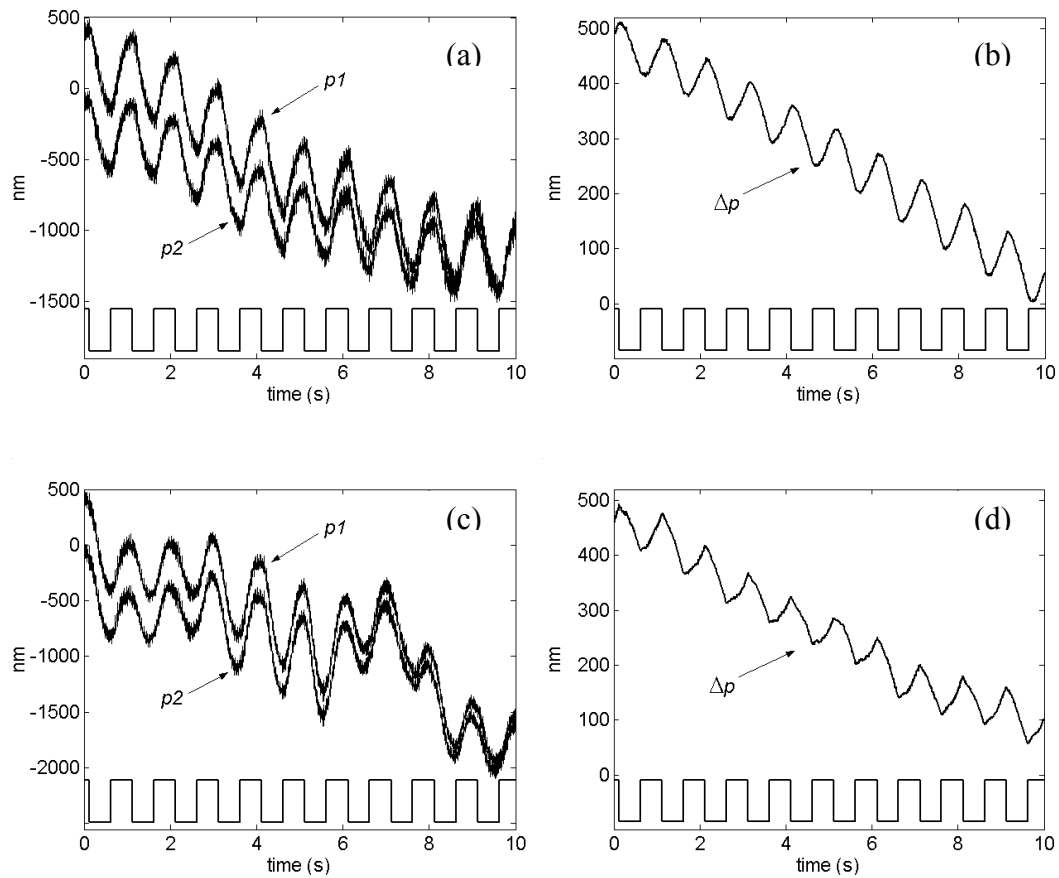


Figure 6.3: Individual ($p1$, $p2$) and differential (Δp) path length variations between two points in arterial tissue in response to laser excitation. $p1$ and $p2$ are recorded from 100 μm and 200 μm below the luminal surface, respectively. (a) and (b) from healthy area, and (c) and (d) from above the plaque. Positive cycles of rectangular waveforms indicate laser excitation.

6.5 DISCUSSION

Light scattering, non-uniform distribution of chromophores (hemoglobin), and temperature diffusion alter tissue responses, which may be difficult to

interpret. However, we know that when light is absorbed, a temperature increase is produced near specific chromophores, which induce photothermal related changes. In the experiment, blood was the target chromophore absorbing excitation light (532 nm). Although spatial distribution of hemoglobin in the sample was unknown, blood in the deeper regions (media and adventitia) that nourishes the vessel was observed with the unaided eye. Therefore, temperature increase due to light absorption originates mainly in the deeper regions, and diffuses towards the measurement site. Increased temperature at the measurement site produces thermo-elastic and thermo-refractive variation in optical path length. Measurement of surface temperature using a thermocouple or an IR camera may aid better understanding of temperature related response in arterial tissue.

6.6 CONCLUSION

PS-OLCR provides a non-invasive tool to image depth-resolved features as well as to detect nanometer scale path length changes between two points in arterial tissue in response to laser stimulation. Fiber-based implementation of PS-OLCR suggests *in-vivo* applications through catheter and endoscopic probes. The photothermal response of atherosclerotic artery may be used to measure mechanical properties of plaque. Such a response is believed to be different in healthy and atherosclerotic arteries. Development of this technique to diagnose plaques will require further investigation.

Chapter 7: Birefringence Measurement of Nerve

7.1 ABSTRACT

Tissue birefringence can be quantified in reflection mode by differential phase measurements. A crayfish ventral nerve cord is imaged to study birefringence measurements using the phase sensitive optical low-coherence reflectometer (PS-OLCR). System performance is tested at several sample angular orientations.

7.2 INTRODUCTION

Birefringence, the difference between refractive indices for light polarized parallel and perpendicular to optical axis, is an optical property shared by many biological structures, such as muscle, nerve, bone and cartilage. Origin of birefringence is the orientation of submicroscopic structural elements. Total birefringence in tissue is due to three different origins: *Intrinsic birefringence* is due to molecules or macromolecules with anisotropic polarizability oriented in a direction; *form birefringence* occurs if isotropic structural elements are oriented and spaces are filled with an isotropic substance having different refractive index; and *accidental birefringence* occurs if the degree of freedom of valence electrons is reduced by stress, pressure, electric or magnetic fields (von Muralt, 1975).

Depth resolved birefringent imaging of biological tissue has been presented by using polarization sensitive optical coherence tomography (de Boer

et. al., 1997). In this chapter, performance of PS-OLCR for measuring birefringence of biological tissue is investigated. Images of a crayfish ventral nerve cord are recorded at several angular orientations. An angle-independent PS-OLCR configuration for measuring linear birefringence is discussed.

7.3 MATERIALS AND METHODS

Ventral nerve cord of a crayfish is dissected and placed on a microscope slide. The microscope slide was on a rotational stage allowing different nerve orientations. Figure 7.1 illustrates the PS-OLCR sample path configuration to image the nerve. Cross-sectional images are obtained by scanning two galvanometers one in the reference path (depth scan) another in the sample path (lateral scan). The sample galvanometer was scanning slowly (1 scan/s) while the reference galvanometer operated at 100 scans/s. As a result, acquisition of a cross-sectional image took one-second. The reference galvanometer provided

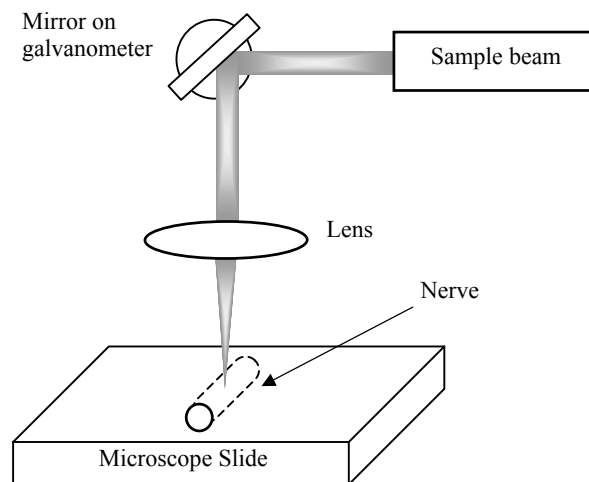


Figure 7.1: Sample path configuration of PS-OLCR to image a crayfish nerve.

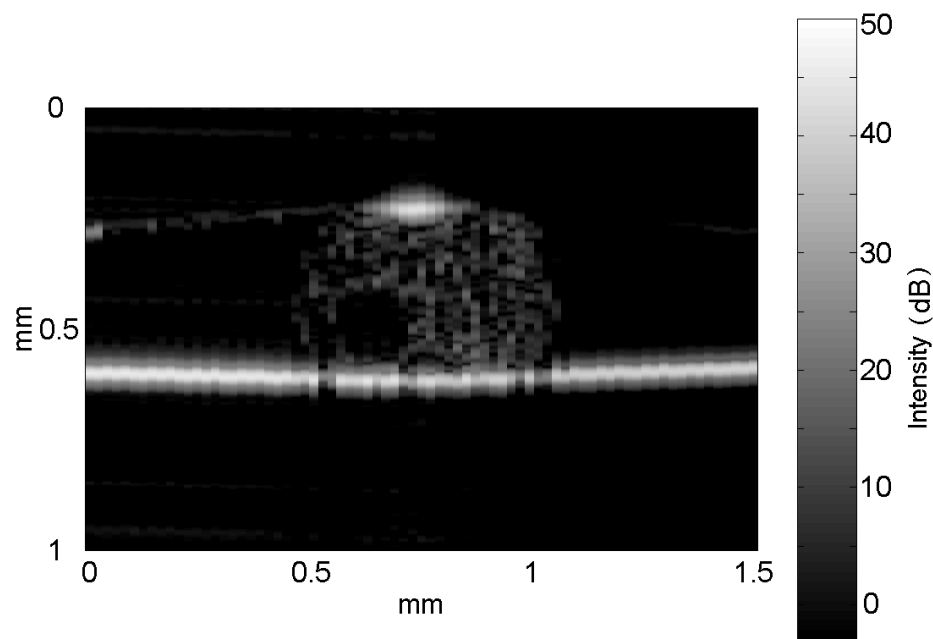
only a group delay, while a LiNbO₃ phase modulator produced interferometric fringes at a precise center frequency (100 kHz). Digital signals in horizontal and vertical channels are acquired at 5 Ms/s sampling rate.

7.4 RESULTS

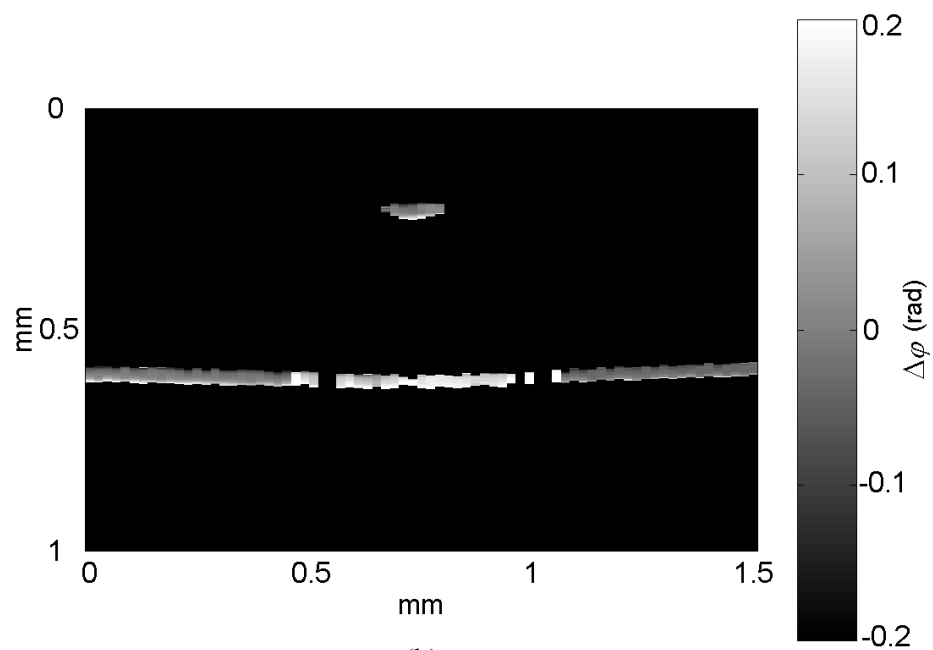
Figure 7.2 shows images constructed from intensity and phase information of the PS-OLCR channels. The nerve was aligned parallel to one of the polarization channels. Because of higher reflectance from boundaries, top surface of the nerve and microscope slide underneath are clearly visible. Although structures appear inside the nerve in intensity image (Figure 7.2a), higher resolution is needed. A water-air interface is noticeable as well. Coherence functions in this experiment had side-lobes; as a result, surface of the microscope slide appear larger than the coherence length.

Phase calculation is performed where the signal has reached a certain threshold. So that, only the microscope slide and top surface of the nerve is visible in Figure 7.2b. When the beam goes through the nerve, one PS-OLCR channel was delayed with respect to the other due to the birefringence of nerve.

Retardation caused by birefringence is extracted using the light back reflected from microscope slide. Figure 7.3 illustrates the maximum relative phase shift between the PS-OLCR channels, when the nerve was aligned along one of the polarization channels (0° orientation). The same information is color-coded in grayscale in Figure 7.2b. Average phase shift across the nerve is found to be 0.173 radians that corresponds to an optical path length difference of 18 nm



(a)



(b)

Figure 7.2: Depth resolved intensity and phase images of a crayfish nerve.

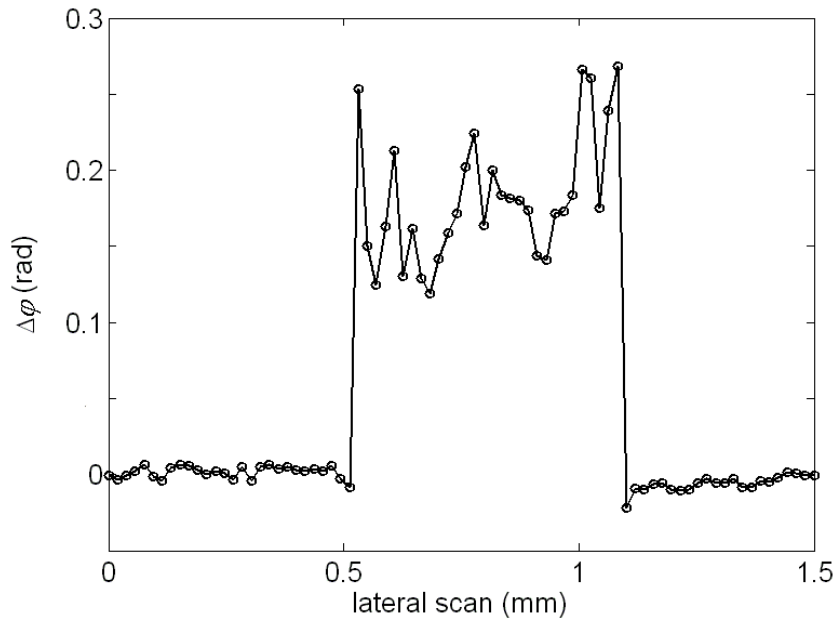


Figure 7.3: Maximum phase retardation due to birefringence of a crayfish nerve. Measurement is performed when the nerve was along one of the polarization channels (0° orientation).

between the orthogonal axes of the nerve. If the sample thickness (d) is known, birefringence can be calculated [$\Delta n = \Delta\phi \lambda / (4\pi d)$]. Assuming the refractive index of nerve to be 1.4, nerve thickness is estimated from the intensity image as $280 \mu\text{m}$. Then, birefringence of the crayfish ventral cord is found to be 6.4×10^{-5} .

The experiment is repeated for different angular orientations of the nerve. Figure 7.4 shows measured average phase retardations as a function of angular orientation. When the nerve is aligned 45° to the polarization channels, the measured phase difference is zero. Therefore, sample orientation with respect to the polarization channels makes the birefringence measurement angle-dependent when utilizing the described PS-OLCR configuration.

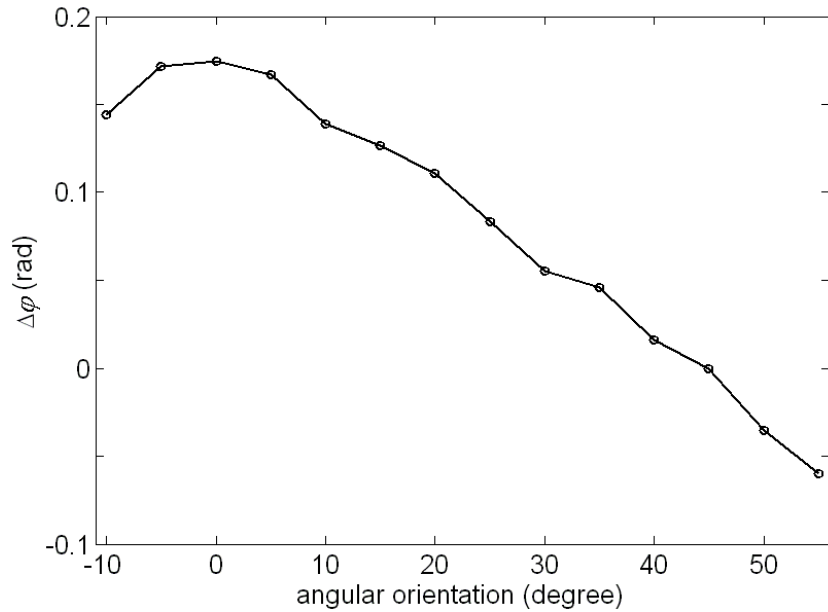


Figure 7.4: Measured phase retardations as a function of nerve orientation.

7.5 DISCUSSION

An angle-independent PS-OLCR configuration for measuring linear birefringence has been recently demonstrated (Davé *et al.*, 2003). In that configuration, linearly polarized light is coupled into fast or slow axis of the input PM fiber, and a quarter-wave-plate with axis oriented 45° to the system channels is placed into the sample path. Therefore, circularly polarized light is incident upon the sample. Because of sample birefringence, back reflected light becomes elliptically polarized. In the analysis, retardation can be calculated from the ratio of envelopes of the amplitude modulated fringe signals in the two channels, whereas sample orientation can be found using the phase difference.

7.6 CONCLUSION

Birefringence measurement of PS-OLCR is studied using a crayfish ventral nerve cord, and the birefringence is found to be 6.4×10^{-5} . Angle dependency of PS-OLCR utilizing linearly polarized channels incident on the sample is demonstrated. An angle independent configuration using circularly polarized light incident on the sample is discussed.

Chapter 8: Optical Detection of Neural Activity

8.1 ABSTRACT

If transient changes associated with action potential propagation are detectable using back-reflected light, early detection of neural diseases may be achieved non-invasively. This chapter explores transient changes in stimulated nerves and demonstrates experimental results obtained from the differential phase measurements of phase sensitive optical low-coherence reflectometer (PS-OLCR). Nerves dissected from crayfish walking legs resulted in approximately 1 nm surface displacement associated with action potential propagation. Because no chemicals or reflection coatings that may harm the nerve were applied, the technique may be used for early detection of neural diseases such as glaucoma, multiple sclerosis and Alzheimer's.

8.2 INTRODUCTION

Neural studies especially in the active state have been the subject of considerable research. Volume changes due to swelling and shortening, birefringence, optical rotation, fluorescence and turbidity are some of the changes observed with action potential propagation that can indicate structural changes in the nerve. Measurement of these changes in the excited nerve may yield diagnostic tools for various neuropathies. Because neural diseases such as glaucoma, multiple sclerosis and Alzheimer's are debilitating, and nerve cell death

is irreversible, non-invasive detection of neural activity for early detection is extremely important.

Over the last fifty years many studies have been reported for optical detection of neural activity. In 1950, D. K. Hill studied volume change of a single nerve fiber from cuttlefish, and reported swelling as well as an initial shrinkage using repetitive stimulation. In 1968, Cohen *et al.* demonstrated light scattering and birefringence changes during neural activity with nerve bundles from walking legs of crabs and squid giant axons. In the same year, Tasaki *et al.* (1968) published results demonstrating fluorescence, turbidity and birefringence changes with nerve trunks from the legs of lobsters and spider crabs, and with squid fin nerve. These transient optical changes also occur in the electric organ of *Electrophorus electricus* (Cohen *et al.*, 1969), olfactory nerve of pike (von Murallt, 1975), crayfish axons (B. C. Hill, 1977), and olfactory nerve of garfish (Tasaki and Byrne, 1992). More detailed description of previous studies is presented in Section 8.3.3.

This chapter presents a review of neurophysiology including anatomy, action potential propagation and associated transient changes in volume and birefringence, and experimental results of PS-OLCR for detecting neural activity. The experiments are performed on crayfish and squid (*Lolliguncula brevis*) nerves, and designed to measure transient changes in surface displacement, retardation and optical path length. Using PS-OLCR, nearly 1 nm displacement of neural surface is measured from nerves dissected from front walking legs of crayfish without introducing any chemicals or reflection coatings. The surface

displacements are approximately 1 ms in duration and occurred about the action potential arrival to the optical measurement site. Together with the optical measurements, electrical action potential and histology of the nerves are presented and discussed. Results reported in this chapter indicate that PS-OLCR is a good candidate for non-invasive measurement of changes in an excited nerve.

8.3 LITERATURE REVIEW

Section 8.3.1 describes structural elements in the nerve. Then, Section 8.3.2 presents action potential propagation. A review of transient changes in volume and birefringence during neural activity is given in Section 8.3.3.

8.3.1 Nerve Anatomy

Although several types of neurons exist, typically they have been divided into four main components. These are (i) the *cell body* also called soma, which consists of a nucleus and perikaryon; (ii) *dendrite*, which carries information toward the cell; (iii) *axon*, which transmits information away from the cell body, and (iv) *synaptic terminals*, which transfer action potential. Around the neurons, Glial cells serve as supporting elements and also separate and insulate groups of neurons. Oligodendrocyte and Schwann cells, which form myelin, are the two types of the glial cells in the central and peripheral nervous systems, respectively. Some axons of both sensory and motor neurons are myelinated. Unmyelinated axons exist in the human retina and in some animals such as squid.

Most of the protein made in neurons is synthesized in the cell body. As in other cells, most of the protein formed in neurons is cytosolic. Proteins consist of two groups in the cell: (i) the fibrillar elements, and (ii) the numerous enzymes that catalyze metabolic reactions in the cell. Fibrillar proteins of the cytoskeleton are responsible for the shape of neurons. Various types of fibrillar elements exist. Main constituents of the cytoskeleton are microtubules, neurofilaments, and microfilaments together with their associated proteins.

Microtubules, the thickest of the neuron's cytoskeletal fibers, are long polar polymers usually constructed of 13 protofilaments packed in a tubular array with an outside diameter of 25-28 nm. In the axon, microtubules are arranged in parallel, with the plus end pointing away from the cell body and the minus end facing the cell body.

Neurofilaments, 10 nm in diameter, are the most abundant fibrillar components in axons. Three to ten times more neurofilaments than microtubules are present in an axon. Neurofilaments consist of fibers (monomers) that twist around each other. Unlike microtubules, neurofilaments are very stable and almost totally polymerized.

Microfilaments, 3-5 nm in diameter, are polar polymers of globular actin monomers wound in a two-stranded helix. Unlike the microtubules and neurofilaments actin filaments form short polymers. For details on neural physiology, the book 'Principles of neural science' by Kandel *et al.* is suggested.

8.3.2 Action Potential

Gated and non-gated ion channels in the nerve membrane control current flow. Non-gated channels, which are always open, are primarily important in maintaining the resting membrane potential. Gated channels, in contrast, can open and close. Most gated channels are closed when the membrane is at rest. Probability of opening is greatly enhanced by change in membrane potential, ligand binding and stretch of the membrane.

Changes in the relative membrane permeabilities to Na^+ , K^+ and Cl^- ions alter the membrane potential during action potential propagation. At rest, the membrane is most permeable to K^+ . However Na^+ permeability is dominant in the active state. According to the Hodgkin and Huxley hypothesis, the movements of ions across the membrane through voltage-gated (Na^+ , K^+) channels produce the action potential. This active state works as an 'all or none' rule. An action potential is not generated until the membrane potential reaches a threshold value. At the threshold voltage, the net ionic current changes from outward to inward, depositing positive charge on the inside of the membrane. Action potential is usually generated at the axon hillock, which contains the highest density of Na^+ channels. After the action potential propagation, an increase in membrane potential occurs because K^+ channels that open in the later phase require a few milliseconds to return to the closed state.

The action potential is an indication of information transfer, and a product of structural changes in the active nerve. Although this voltage difference can be recorded using intra-cellular or extra-cellular electrodes, electrodes can easily

damage the nerve. A non-invasive technique for measuring neural activity is needed.

8.3.3 Previous Studies on Neural Activity

Optical properties of the nerve change during action potential propagation. These optical changes are due to structural and biochemical changes in the nerve such as molecular reorientations in the membrane, influx and outflux of ions, and change in axon diameter. Investigation of neural structural changes accompanying action potential propagation are ongoing, and better understanding is dependent on optical methods employed. In 1973, Cohen published a review paper on changes in neuron structure during action potential propagation and synaptic transmission. In the review paper, Cohen discusses birefringence, fluorescence, light scattering, absorption and emission, chemical composition, and volume changes. In the next subsections, previous studies on volume and birefringence changes are presented.

8.3.3.1 Volume Changes

In 1950, D. K. Hill investigated volume change due to stimulation of cuttlefish axons mounted on a microscope with dark field illumination. By imaging one edge of the axon focused at a parallel slit in the objective image plane, light intensity passing through the slit was expected to change in response to a volume change. In the article, Hill reported that an increase in radius of a single cuttlefish nerve fiber was about 100 nm for 10,000 impulses of repetitive

stimulation at 200 stimuli/s. Interestingly, in some cases, Hill observed an initial shrinkage before swelling.

Crab and lobster leg nerves shorten as a result of stimulation (Bryant and Tobias, 1955). The measurement setup employed a platinum reflector hanging on the nerve, which redirects incoming light to a photocell through a slit. In the experiments, change in light intensity resulting from reflector movement was analyzed. Since cuttlefish axons (Hill, 1950) also shortened when their volume increased in hypotonic solutions in response to action potential propagation, the shortening may be due to an increase in axon volume (Cohen, 1973).

B. C. Hill *et al.* (1977) used a laser interferometer to examine small rapid changes in the diameter of a crayfish giant axon. The giant axon was about 180 μm in diameter. Their experiments with gold particles positioned on the axon resulted in rapid changes in the axon diameter with a period of about 1 ms, and amplitude of 1.8 nm. An interesting finding by Hill *et al.* is that results of their experiments are presented as contraction of the diameter followed by a slow expansion.

In 1980, Iwasa and Tasaki studied mechanical changes accompanying action potential propagation in squid giant axon. They measured pressure changes in the axon using a stylus attached to a piezo-ceramic bender, and surface displacements using a fiber sensor. In their surface displacement experiments, gold particles were placed on the axon, and the fiber sensor measured change in back-reflected light. Iwasa and Tasaki reported that swelling (~ 0.5 nm, 1 ms) was the primary event taking place in squid giant axon due to action potential

propagation. To compare results of their recording device with the results reported by Hill *et al.* (1977), they examined mechanical response of crab and crayfish axons, and indicated that crustacean axons also expand during the depolarization phase of the action potential.

Rapid mechanical changes were reported in the garfish olfactory nerve (Tasaki *et al.*, 1989). Sudden release of pressure associated with action potential propagation was detected by a stylus, which was glued on a piezoceramic bender. The other end of the bender was connected to an operational amplifier. The swelling signal started nearly at the onset of the action potential and reached a maximum simultaneous with the peak of the action potential. In addition, by introducing the olfactory nerve vertically in a chamber and connecting the upper end of the nerve to the stylus, they observed a decrease in length of the neural fibers. Duration of this mechanical response was significantly longer than the swelling signal, possibly due to slow conduction of the impulse along the nerve. Moreover, the authors reported a summation of shortening for repetitive stimulation.

Tasaki and Byrne (1990) published results on volume expansion using garfish olfactory nerve. In their experiment, rapid change in the hydrostatic pressure in a watertight chamber was measured by using a mechanoelectric transducer. They demonstrated volume of the nerve increased in response to electrical stimulation. Therefore, shortening and swelling events were not compensating each other in volume changes associated with neural activity. In another publication, Tasaki and Byrne (1992) reported swelling, pressure and

birefringence changes in response to stimulation of garfish olfactory nerve, and suggested that swelling, pressure and birefringence changes were a different manifestation of the same structural changes.

More recently, surface displacement of lobster nerve bundles and *Nitella* internodes was demonstrated using an optical lever recording (Yao *et al.*, 2003). Their optical setup requires a reflecting surface with one edge resting on the surface of the nerve, and the other edge resting on a knife-edge as a reference point. Therefore, if swelling occurs, the reflecting surface tilts and deflects a light beam detected by a position detector. They reported swelling of the lobster nerve between 0.1 nm and 0.8 nm. They observed an initial swelling of the *Nitella* internodes between 5 nm and 15 nm, and a large shrinkage between 50 nm and 150 nm.

8.3.3.2 Birefringence Change

Birefringence (Δn) is introduced in Chapter 7.2. Many studies reported in the literature use a common optical setup to measure relative light intensity change ($\Delta I/I$) associated with a transient change in birefringence. The apparatus consists of two crossed polarizers (polarizer and analyzer) at 90° orientation, while the nerve under study is placed between these components typically at 45° to the axes, which yields maximum intensity change. Measured intensity change (ΔI) during action potential propagation is due to a transient change in retardation (ΔR). The relation between the relative change in measured light intensity ($\Delta I/I$) and the calculated change in retardation is,

$$\Delta R = \frac{1}{2} R \frac{\Delta I}{I}, \quad (8.1)$$

where R is the retardation due to the resting birefringence, and I is the resting intensity of light (Cohen *et al.*, 1970).

The retardation (R) is the product of birefringence (Δn) and sample thickness (d), ($R = \Delta n \times d$). Therefore, the measured retardation change may be directly attributed to the birefringence change, if the nerve thickness does not vary. Because the retardation equation includes the sample thickness, which itself can change the form birefringence, the related PS-OLCR measurements are called retardation change experiments in this dissertation. However, the term ‘birefringence change’ has been frequently used in literature as reviewed below.

In 1968, Cohen *et al.* used the crossed polarizer setup to record birefringence change during action potential propagation. The amount of light passing through the crossed polarizers with the nerve placed at 45° to these polarizers decreased temporarily by $(1-9) \times 10^{-4}$ in crab nerves and by $(3-11) \times 10^{-6}$ in squid giant axons. For the crab nerve 25-200 recordings, and for the squid axons 3,000-25,000 recordings were averaged to obtain a reasonable signal to noise ratio. In the same year, Tasaki *et al.* (1968) reported changes in birefringence associated with neural activity using nerve trunks harvested from crab legs and squid giant axon. In birefringence experiments, when the nerve is positioned parallel to the principle axis of the polarizer or analyzer, no clear optical signal was observed (Cohen *et al.*, 1968; Tasaki *et al.*, 1968).

If all physical changes related to the optical signal occur in the membrane, two mechanisms exist to obtain a larger signal: (i) measurement of membrane-

specific properties such as fluorescence of a dye that specifically binds to membranes, or (ii) use of smaller axons (Cohen, 1973). The latter case may be explained by considering a squid giant axon and a crab nerve that consists of many axons (average axon diameter is $\sim 1 \mu\text{m}$). The squid axon membrane comprises only 10^{-4} of the axon's dry weight, whereas axon membrane in the crab nerve makes up about 10^{-2} of its dry mass (Cohen, 1973). Therefore, assuming thickness of the axon membranes are the same, the change in membrane properties in the crab nerve would be 2 orders of magnitude larger than in squid giant axon of the same size. For example, olfactory nerve of freshwater pike used by von Muralt (1975, 1976) has 4 million nerve fibers of an average diameter of $0.2 \mu\text{m}$, and caused almost 10^3 times larger relative intensity change ($\Delta I/I$) compared to the giant axon. The olfactory nerve of pike resulted in a relative intensity change of $\Delta I/I = 3.3 \times 10^{-3}$, and could be recorded with a single sweep on the oscilloscope (von Muralt, 1975).

Cohen *et al.* (1970) reported that the average resting retardation measured at the center of six squid axons (mean diameter of $850 \mu\text{m}$) was measured 56 nm using white light, which represents a birefringence of $\Delta n = 6.6 \times 10^{-5}$. This number may be compared with the birefringence of crayfish ventral nerve cord (6.4×10^{-5}) measured in Chapter 7. Most of the resting retardation at the center of the axon is contributed by longitudinally oriented fibrils and tubules in the axoplasm, because removal of the axoplasm and perfusion with potassium fluoride solution reduced the resting retardation through the center by about 90%. At the edges of the axon the resting retardation was unaffected by perfusion.

When probing the edge of the squid giant axon, Cohen *et al.*, (1970) calculated the retardation change (ΔR) in response to neural stimulation as 5.6×10^{-4} nm (=0.56 pm). The given retardation change corresponds to a phase difference of the two components of elliptically polarized light of approximately one millionth of a wavelength ($\lambda \sim 550$ nm). Cohen *et al.* (1969) stated that the retardation changes are 0.2 pm for a squid axon, 10 pm for a crab leg nerve and 60 pm for an electric organ of *Electrophorus Electricus*. A retardation change of 41 pm is given for a pike olfactory nerve (von Muralt, 1975).

In experiments involving squid giant axon, time courses of retardation change and action potential were similar (Cohen *et al.*, 1970). Therefore, retardation change could be dependent on membrane potential, but not on ionic currents or permeability. Further investigation was carried out by measuring retardation change during voltage clamp steps (Cohen *et al.*, 1971). Although Cohen (1973) stated the retardation change was potential dependent, he addressed limitations of their conclusion related to experimental constraints.

Cohen (1973) also stated that the physical origin of the observed retardation change remained obscure. One mechanism, he mentioned, could be the large change in the potential gradient, which would reorient membrane molecules. If these molecules were anisotropic, their reorientation would change birefringence (Kerr effect). The second mechanism stated for retardation change might be electrostriction. Charges creating membrane capacity would compress the membrane, and make the membrane thinner. The thinning itself could change the birefringence, or it would induce birefringence change indirectly by

reorienting membrane molecules. Sato *et al.* (1973) mentioned a third mechanism proposed by Tasaki that a transient decrease in birefringence originates from the longitudinally oriented fibrous material found near the axonal membrane.

Sato *et al.* (1973) examined birefringence changes in squid giant axons, which were flattened after removal of axoplasm. They suggested that there were changes in refractive index for linearly polarized light with its electric vector directed parallel to the long axis of the axon. Landowne (1985) used internally perfused squid giant axons, and found the time course of birefringence changes related to many properties of the gating currents. The birefringence response resembles the time integral of the gating current, and its magnitude suggests several hundred peptide bonds per channel reorient during neural activity (Landowne, 1993). Therefore, reorientation of dipoles within the membrane could produce both the gating currents and the birefringence response.

8.4 MATERIALS AND METHODS

Section 8.4.1 presents the nerve preparation. A nerve chamber consisting of an optical read out area and platinum electrodes for creating and recording action potentials is described. Optical measurements and associated sample path configurations are explained in Section 8.4.2.

8.4.1 Preparation

The animal models used in this chapter are crayfish and squids (*Lolliguncula brevis*). Crayfish are obtained locally, and nerve bundles harvested

from front walking legs are used. The squids are obtained from the National Resource Center for Cephalopods at the University of Texas Medical Branch, Galveston, TX, by overnight shipping. The nerve dissected from squids usually consists of a giant axon and a fin nerve, which consists of a few hundreds smaller axons.

All dissections are performed under a surgical microscope. In crayfish nerve experiments an extracellular solution of 205 mM NaCl, 5.3 mM KCl, 13.5 mM CaCl₂·2H₂O, and 2.45 mM MgCl₂·6H₂O with pH adjusted to 7.4 is used. However, 900 milliOsmole artificial seawater is used in squid experiments.

Figure 8.1 illustrates a nerve chamber machined from plexiglass that can create and record action potentials. Vertical component of the plexiglass is attached to a three-dimensional (xyz) stage for easy alignment in the PS-OLCR optical setup. The chamber consists of several pools that are connected to a groove. The groove, in which a nerve is positioned, is 20 mm in length and approximately 1 mm wide. Stimulation and recording electrodes made of platinum are placed into the pools, and fixed with epoxy. A piece of cover glass is attached on the groove between the recording electrodes. The cover glass provides an optical reference signal in the surface displacement and path length change experiments. A non-conductive reflecting surface is placed under the optical measurement area. The reflecting surface provides a stable surface that increase back-reflected light in retardation change and optical path length change experiments. Therefore, the nerve was passing through the gap between the cover glass and underlying reflecting surface.

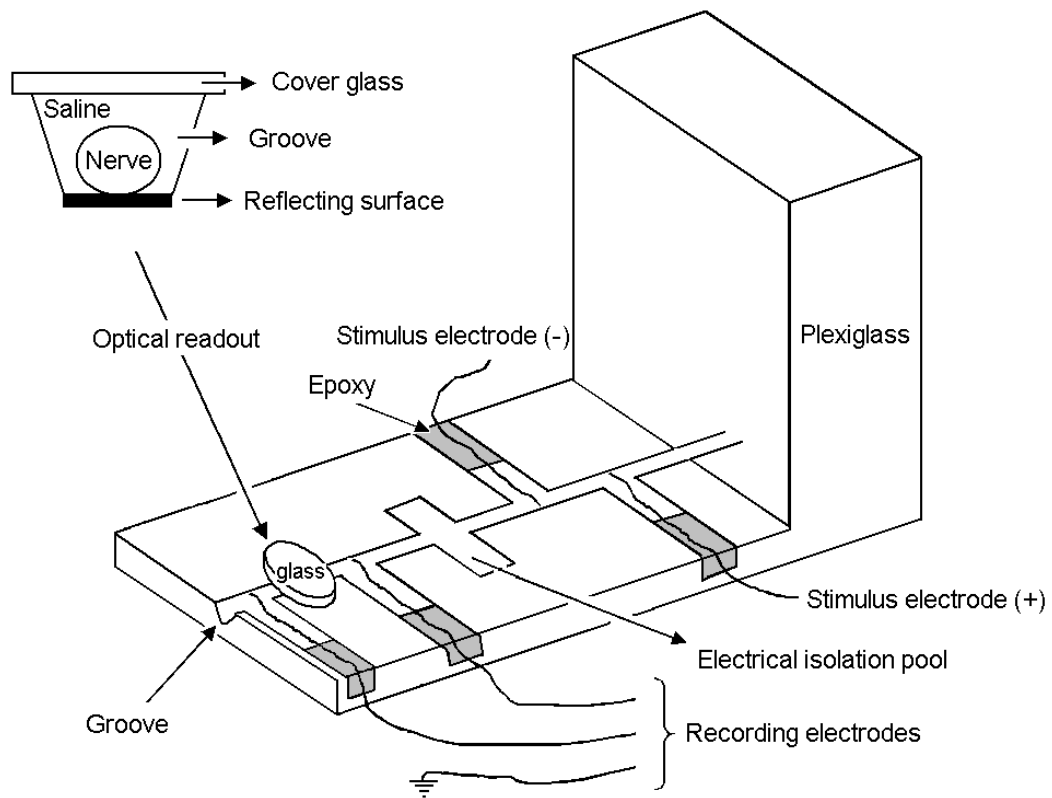


Figure 8.1: Nerve chamber

At least one end of the nerve is tied with a suture, which prevents leakage of axoplasm and helps guiding the nerve through the channel. The other end of the nerve is either tied with another suture, or kept connected to the animal that was sacrificed. After placing the nerve into the groove, pools containing saline solutions are electrically isolated from each other by surrounding each pool with vaseline. Moreover, the electrical isolation pool, which is placed between the stimulation and recording sites, is filled with vaseline for further electrical isolation. A cover glass (not shown) is placed on top of the stimulation site, and

pressed gently to fill small spaces with vaseline. In the optical recording area, the gap between the cover glass and reflecting surface is filled with saline solution, and then sealed with vaseline.

Electrical stimulation pulses applied to the nerve are 50 μ s in duration. The stimulus amplitude is adjusted to create action potential propagations. Time interval between each stimulus is approximately 1 s (0.973 Hz). A differential amplifier with cut-off frequencies set to 10 Hz and 10 kHz, measures the action potentials. A digital oscilloscope, which is synchronized with stimuli, records action potentials.

8.4.2 Measurement Setup

Figure 8.2a illustrates optical configuration of the PS-OLCR sample path for measuring surface displacement in the excited nerve. Translating the birefringent wedges varies relative path length of the polarization channels. The beam is focused on the nerve using a 20X microscope objective. Beam diameter at focus was 4 μ m. Using PS-OLCR depth scans, the nerve and cover glass surfaces are detected and the birefringence wedges are translated to overlap the coherence functions of these two surfaces. Because the nerve was in saline solution, the interference fringes are recorded using reflections from the cover glass-saline interface (reference channel), and the saline-nerve interface (probing channel). After stopping the reference galvanometer (depth-scan), the LiNbO₃ phase modulator produces the sinusoidal fringes at 50 kHz. Analog band-pass filters with cut-off frequencies of 3 kHz and 100 kHz are used to de-noise the

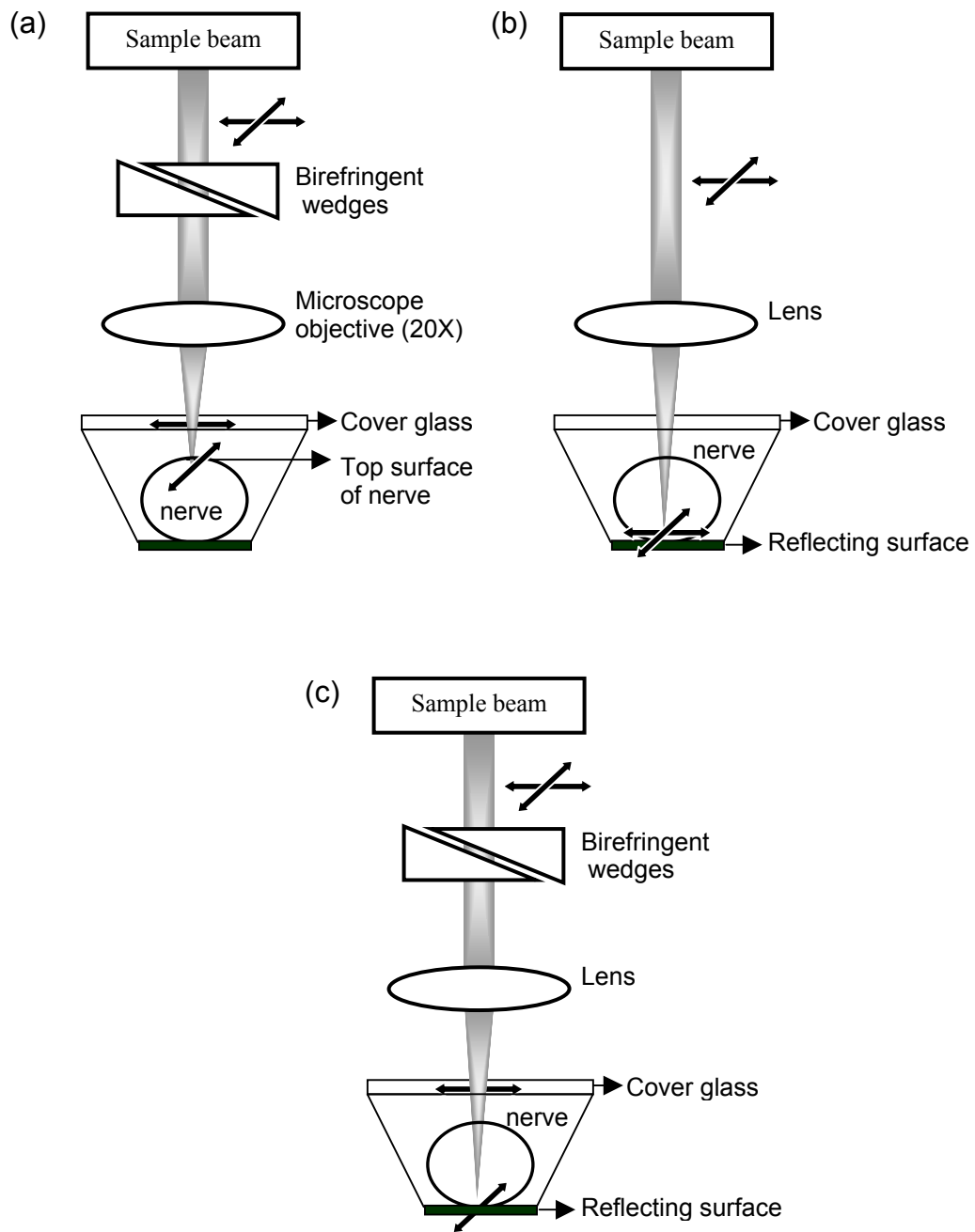


Figure 8.2: Sample path configurations of PS-OLCR for measuring (a) surface displacement, (b) retardation change, and (c) optical path length change of an excited nerve.

photo-receiver outputs. Fringe signals in horizontal and vertical channels are acquired at 5 Ms/s sampling rate.

Figure 8.2b shows the optical setup used for measuring retardation change associated with neural activity. Because both PS-OLCR polarization channels are required to pass through the nerve, the experimental setup does not include the birefringent wedges. The interference fringes are recorded from the reflecting surface underneath the nerve. In retardation change measurements, the nerve was placed parallel to one of the PS-OLCR polarization channels.

The PS-OLCR sample path configuration to measure a change in optical path length is shown in Figure 8.2c. Instead of a 20X microscope objective that gives sharper focus, a 10X microscope objective is used. The interference channels are recorded using reflections from top surface of the cover glass and the reflecting surface underneath the nerve.

8.5 RESULTS

Section 8.5.1 presents experimental results of neural surface displacement associated with action potential propagation using PS-OLCR. Section 8.5.2 and Section 8.5.3 demonstrate PS-OLCR measurements to detect changes in retardation and optical path length due to neural activity, respectively. The electrical action potentials and histology sections of the crayfish and squid (*Lolliguncula brevis*) nerves are given in each section.

8.5.1 Surface Displacement

Surface displacement due to neural excitation is studied using crayfish and squid nerves. Recorded interference fringes with carrier frequency of 50 kHz are post-processed as described previously in Section 2.3.3. Because the cut-off frequencies of differential amplifier that measures the electrical action potential set to 10 Hz and 10 kHz, a 10 kHz bandwidth of the digital band-pass filter is chosen for signal processing (Figure 2.7). After extracting the differential phase signal, optical path length changes are calculated according to (2.8).

Figure 8.3 shows a gray scale trichrome staining of a crayfish nerve. (For histological structure of nerve fibers in crustacea and cephalopods, see Young, 1936). Several nerve bundles as well as the larger axons ($\sim 20 \mu\text{m}$) are visible in the cross-section of the nerve. A portion of the nerve is magnified to show smaller axons and thin sheaths around the axons. Experimental results demonstrated in Figure 8.4 are recorded from this nerve.

Figure 8.4 illustrates optical path length changes due to the neural surface displacement associated with action potential propagation. 500 optical responses are averaged in each trace. Top surface of the nerve was a few tens of micrometers below the cover glass (Figure 8.2a). The upward and downward features of the optical signal indicate swelling and shrinkage directions, respectively. It is interesting that Figure 8.4a shows a swelling while Figure 8.4b represents shrinkage of the same nerve. However, the PS-OLCR signals are recorded from close ($< 1 \text{ mm}$), but spatially distinct points on the nerve. Therefore, the measurements may indicate responses of different axons or axon

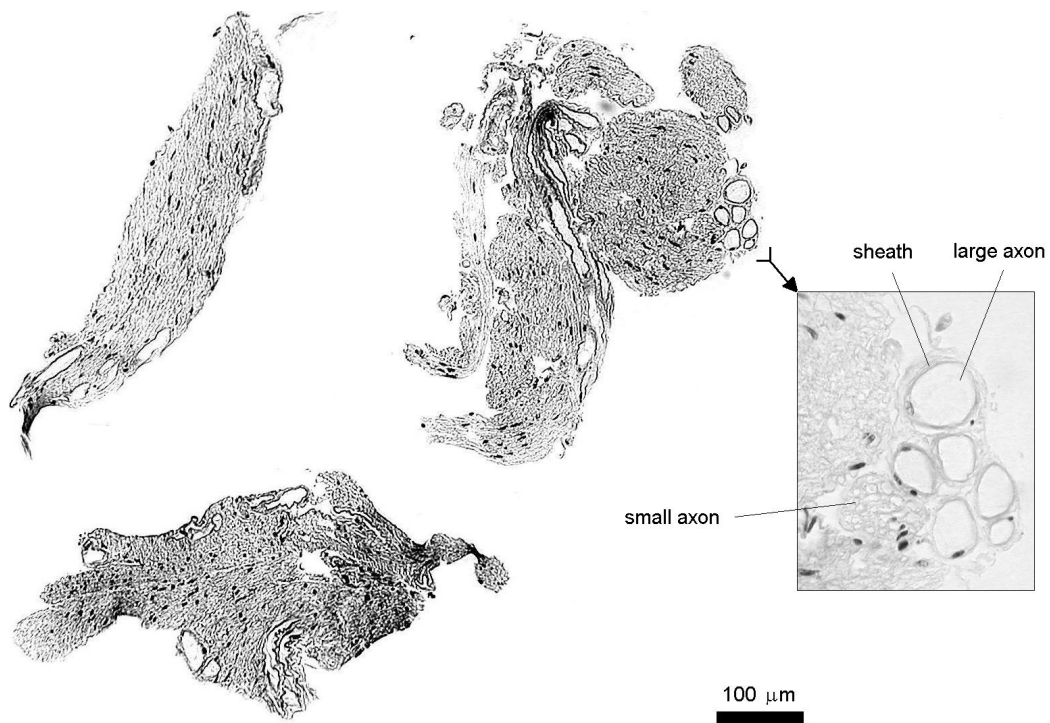
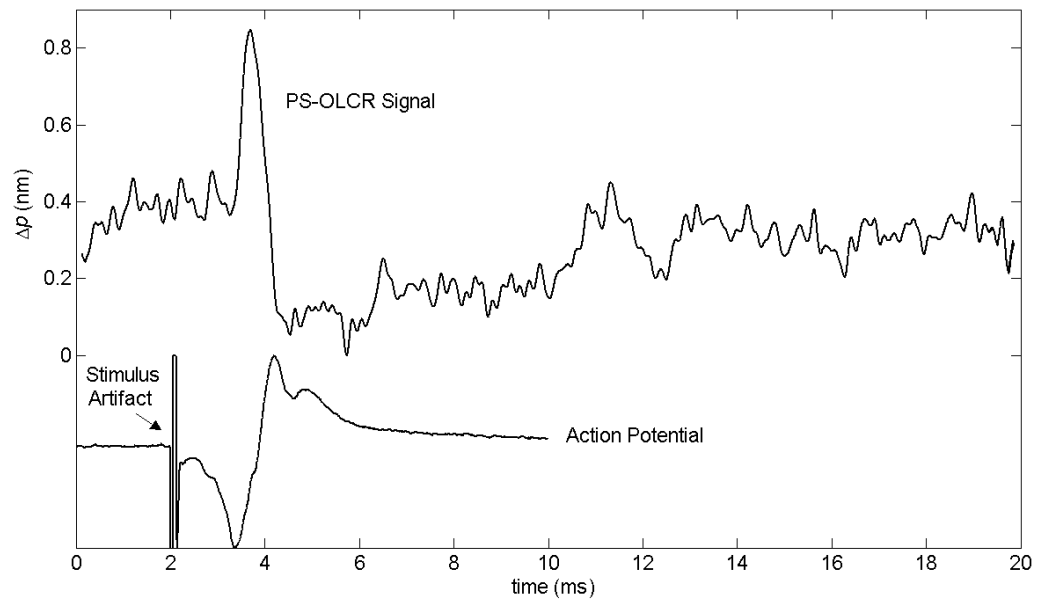


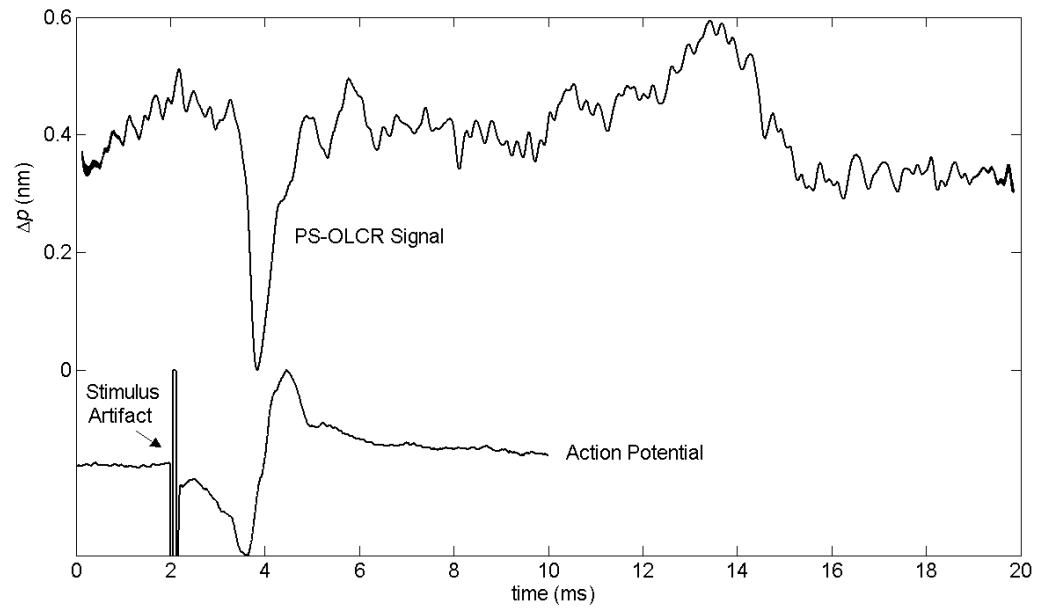
Figure 8.3: Histology (trichrome staining) of a crayfish walking leg nerve.
 Experiment data shown in Figure 8.4 are recorded from this nerve.

bundles. Magnitudes of swelling and shrinkage are similar and approximately 0.5 nm. Swelling and shrinkage mechanisms are discussed in Section 8.6.1.

Figure 8.4 also shows the electrical action potentials. Stimulus (current pulses: 300 μA , 50 μs) is presented at 2 ms, and resulted in a localized artifact in the electrical signal. Because action potentials are recorded differentially using a pair of platinum electrodes placed in the nerve chamber (Figure 8.1), the action potential is thought to arrive at the first and second recording electrodes at the negative and positive peaks of the electrical signal, respectively. Consequently,



(a)



(b)

Figure 8.4: Optical path length change due to surface displacement of a stimulated crayfish leg nerve. Action potentials are in arbitrary units. Stimulus ($300 \mu\text{A}$, $50 \mu\text{s}$) is at 2 ms. (a) and (b) are recorded from spatially close ($<1 \text{ mm}$) but different points on the nerve. Optical signals are average of 500 responses.

the zero-crossing of the electrical signal should indicate time of arrival of the action potential to the optical measurement area, which is between the recording electrodes. The displacements measured by PS-OLCR occurred around the zero-crossing of action potential records (Figure 8.4); hence, the optical signals are most likely due to a neural activity.

Figure 8.5 shows another gray scale trichrome staining of a crayfish nerve. Results shown in Figure 8.6 are recorded from this nerve. In the nerve chamber, the separation between the top surface of the nerve and the cover glass is measured from the PS-OLCR depth scans, and found to be 280 μm . Current excitation pulses (300 μA , 50 μs) are presented at 2 ms in the records.

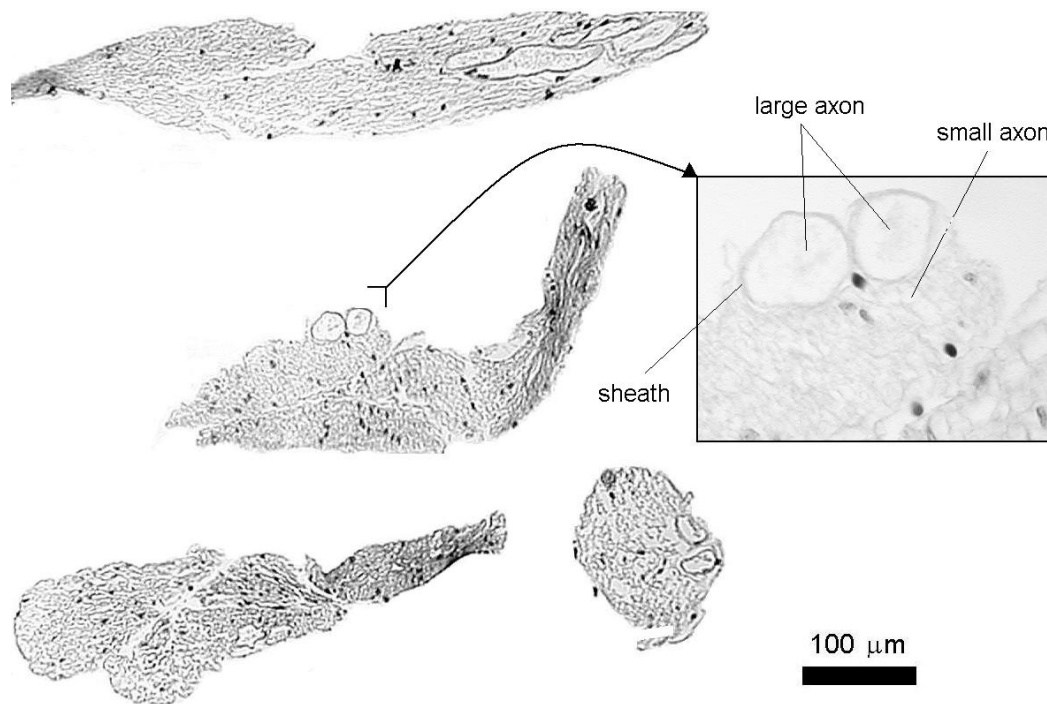


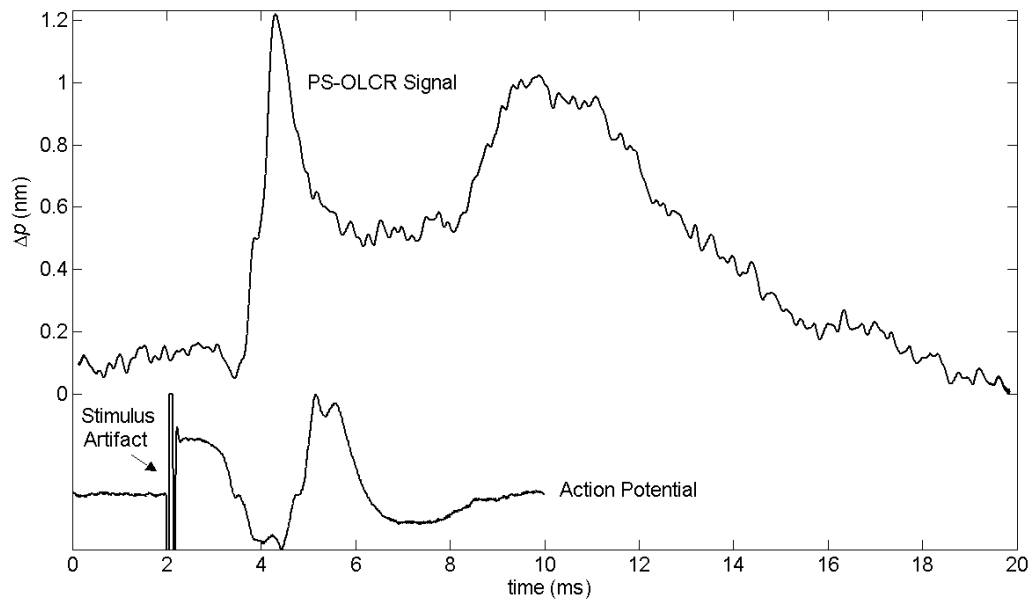
Figure 8.5: Histology (trichrome staining) of a crayfish walking leg nerve.
Experiment data shown in Figure 8.6 are recorded from this nerve.

An average of 500 optical responses recorded from the top surface of the nerve is shown in Figure 8.6a. When the action potential reaches the optical measurement area (approximately zero-crossing of the action potential trace), corresponding change in optical path length occurs. The sharp peak in PS-OLCR signal represents 1.1 nm swelling of the nerve surface. Following the sharp peak, Figure 8.6a contains a feature between 8-12 ms. Because the delayed feature occurs after the action potential record, origin is unclear.

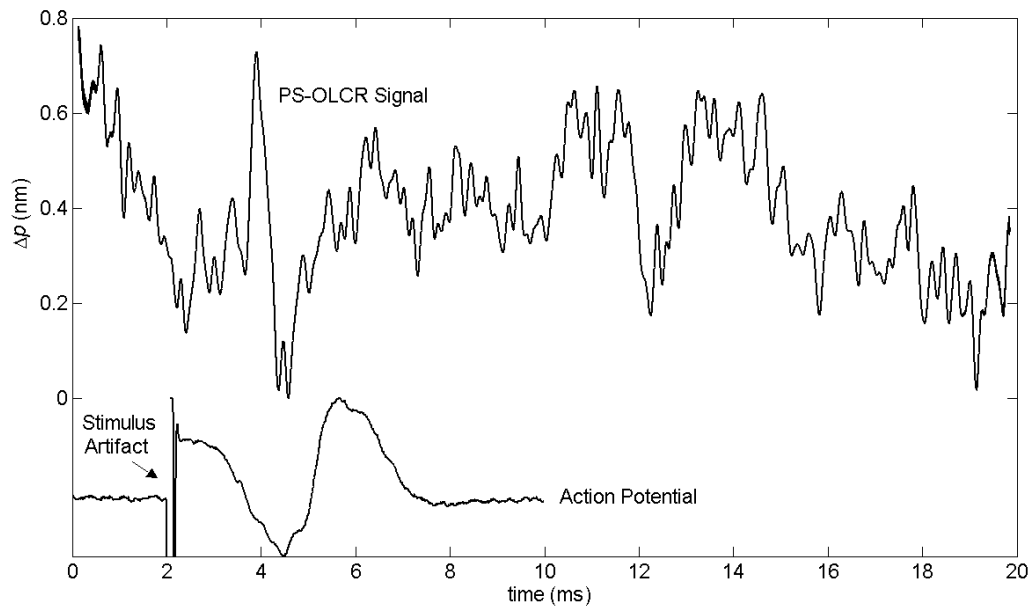
Without changing lateral position of the nerve specimen, a position 15 μm below the nerve surface is probed by a PS-OLCR channel. Figure 8.6b shows an average of 250 optical responses. Although a feature is observed around the zero-crossing of action potential record, and probably reversed compared to the sharp peak of Figure 8.6a, the PS-OLCR signal amplitude from the deeper region is smaller than the one recorded from the top surface. However, additional experiments may be required to compare depth-resolved response of the nerve.

Using the third crayfish nerve, a control experiment is performed. Figure 8.7 shows a portion of the histology section. Different sizes of crayfish axons and sheaths around the axons are clearly visible. Experimental data shown in Figure 8.8 and Figure 8.9 are recorded from this nerve.

Figure 8.8 illustrates results of neural stimulation with stimulus amplitude below and above the activation threshold, which is needed to create an action potential. In the experiment, when the amplitude of current pulses was 60 μA , an action potential was not produced (Figure 8.8a and Figure 8.8c). However, current pulses with amplitude of 100 μA resulted in action potential propagation



(a)



(b)

Figure 8.6: Optical path length change due to surface displacement of a stimulated crayfish leg nerve. Action potentials are in arbitrary units. Stimulus ($300 \mu\text{A}$, $50 \mu\text{s}$) is at 2 ms. (a) and (b) are recorded from top surface (average of 500 responses), and $15 \mu\text{m}$ below the top surface (average of 250 responses) of the nerve, respectively.

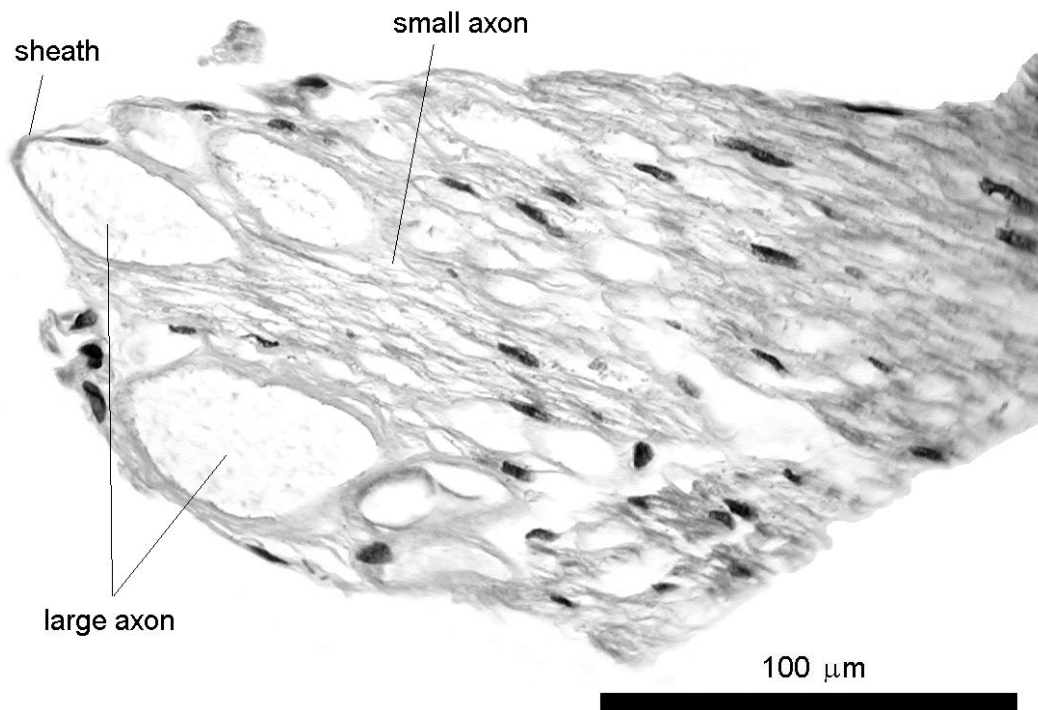


Figure 8.7: Histology (trichrome staining) of a crayfish walking leg nerve. Experimental data shown in Figure 8.8 and Figure 8.9 are recorded from this nerve.

(Figure 8.8b and Figure 8.8d). The stimuli with 50 μ s in duration are presented at 2 ms in all presented records, and correspondingly, stimulus artifacts are visible in the electrical measurements.

The top surface of the nerve is 75 μ m below the reference (cover glass) surface. Optical signals of Figure 8.8 are averages of 100 responses. When an action potential is not observed in the electrical measurement (Figure 8.8a and Figure 8.8c), surface displacement in optical records is not observed, either. However, both electrical and optical records show presence of neural activity

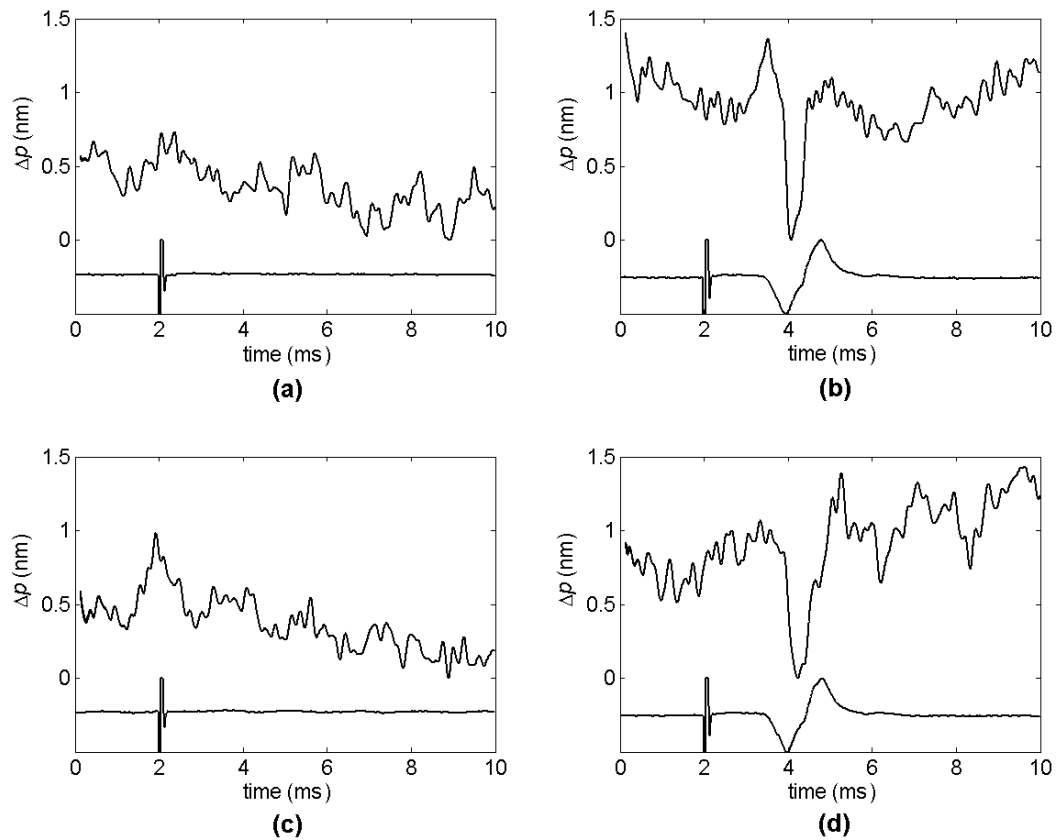


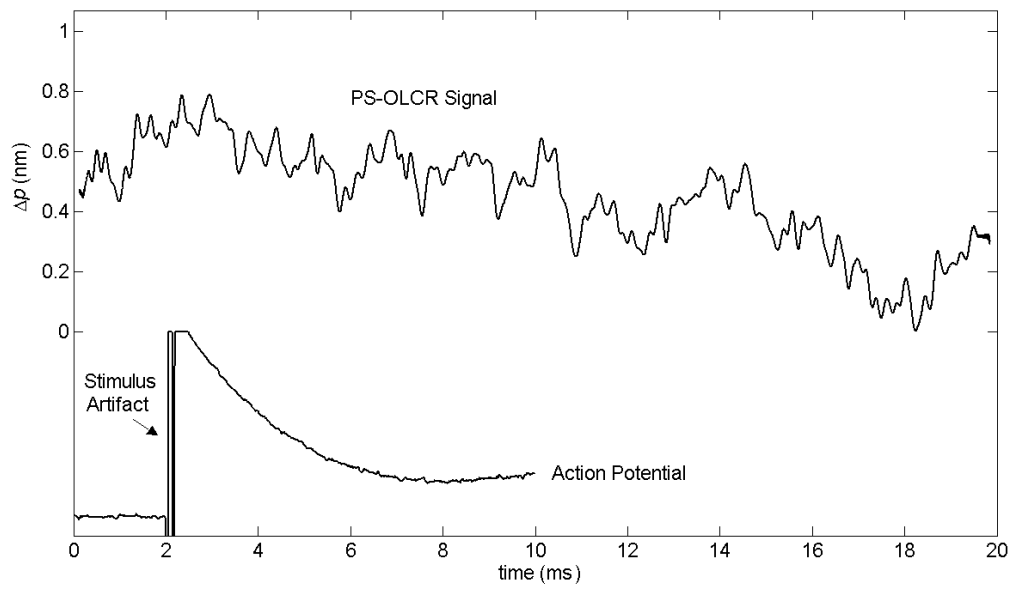
Figure 8.8: Control experiment of surface displacement with stimulus amplitude below and above the action potential threshold. Action potentials are in arbitrary units. Stimulus duration is $50 \mu\text{s}$ and presented at 2 ms. (a) and (c) with stimulus amplitude of $60 \mu\text{A}$, and (b) and (d) with stimulus amplitude of $100 \mu\text{A}$. Optical signals are average of 100 responses, and recorded from top surface of a crayfish leg nerve.

when the amplitude of the current pulses is $100 \mu\text{A}$ (Figure 8.8b and Figure 8.8d). The measured surface displacements indicate shrinkage in the order of 1 nm. This experiment is repeated several times with stimulus amplitude below ($60 \mu\text{A}$) and above ($100 \mu\text{A}$) the threshold, and each time the outcome was similar to the results shown in Figure 8.8.

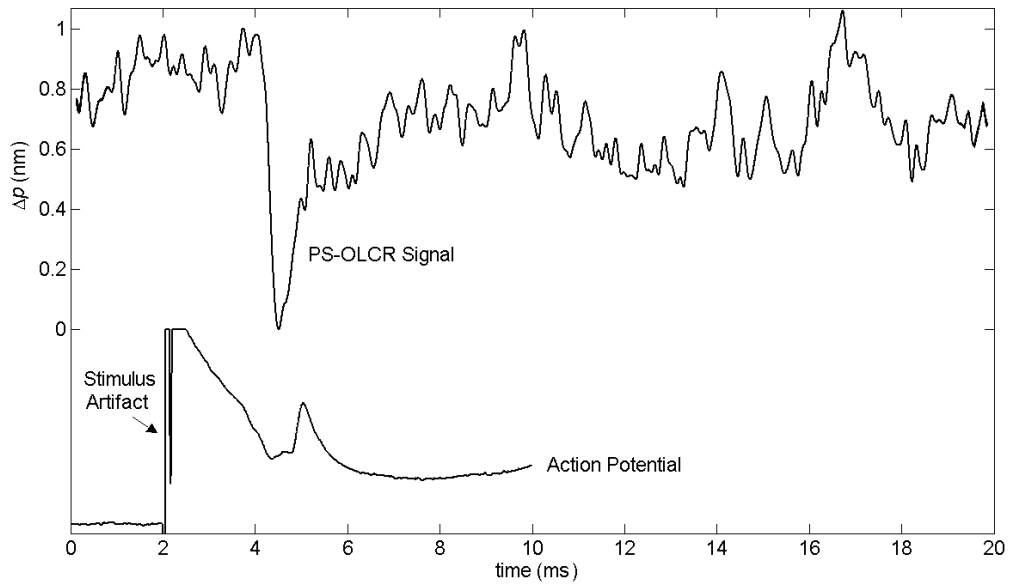
To show that the results are not due to a stimulation artifact, the control experiment is resumed after 2 hours. The new threshold for action potential creation was considerably increased. The position of the nerve was not altered; hence, PS-OLCR was detecting the same spatial point used in the previous experiment (Figure 8.8). Figure 8.9 illustrates averages of 200 optical responses recorded with stimulus amplitude below and above the increased threshold value of neural activation. As in the other nerve experiments, the stimulus duration was 50 μs .

Figure 8.9a shows the measurements taken with stimulus amplitude of 1.4 mA. Because the differential amplifier was saturated with the given stimulus strength, the electrical signal contains an exponential recovery period. Nevertheless, it is obvious that current pulses of 1.4 mA, which is fourteen times larger than 100 μA of the previous experiment, did not produce an electrical action potential. Correspondingly, surface displacement of the nerve was not observed in the PS-OLCR signal.

Then, the stimulus amplitude is increased to 3 mA. Even though the electrical signal is saturated after stimulation, action potential is visible in Figure 8.9b. As a result, the PS-OLCR signal indicates a surface displacement of 1 nm in the shrinkage direction. The magnitude and timing of the optical response is similar to the ones shown in Figure 8.8. Results of the control experiments (Figure 8.8 and Figure 8.9) suggest that the surface displacements are due to neural activity.



(a)



(b)

Figure 8.9: Control experiment of surface displacement with stimulus amplitude below and above the action potential threshold. Action potentials are in arbitrary units. Stimulus duration is 50 μ s and presented at 2 ms. (a) with stimulus amplitude of 1.4 mA, and (b) with stimulus amplitude of 3 mA. Optical signals are average of 200 responses, and recorded from top surface of a crayfish leg nerve.

Surface displacement experiments are performed on squid nerves, too. Figure 8.10 shows a trichrome staining of a nerve dissected from a *Lolliguncula brevis*. Usually, the dissected nerve consists of a giant axon, fine nerve and connective tissue called perineurium around the nerve. Typically, the giant axons in *Lolliguncula brevis* is 150-200 μm in diameter. The fin nerve contains a few hundred small axons. In the experiments, the perineurium could not be removed completely (see Figure 8.14 for a better section). Structure of nerve fibers in crustacea and cephalopods (Young, 1936) and the sheath components of squid giant axons (Bear et al., 1937) were studied many years ago.

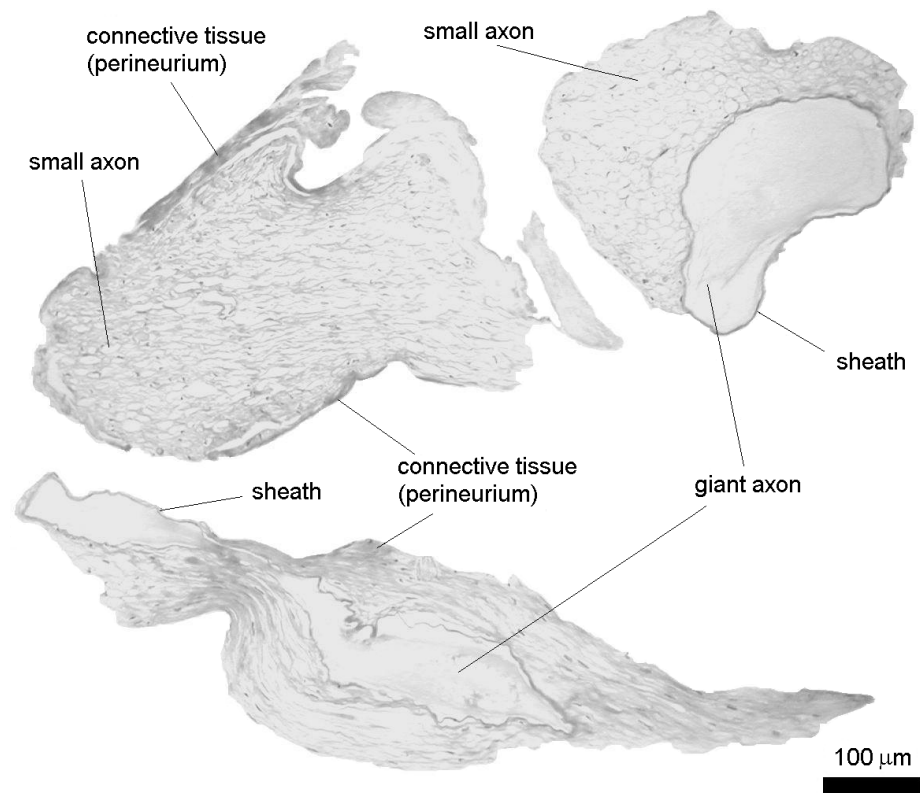


Figure 8.10: Histology (trichrome staining) of a squid (*Lolliguncula brevis*) nerve. Experimental data shown in Figure 8.11 is recorded from this nerve.

Figure 8.11 illustrates results of a surface displacement experiment using the squid nerve shown in Figure 8.10. Stimulus (current pulses: 4 mA, 50 μ s) is presented at 2 ms. The stimulus amplitude is considerably higher than the values used for the crayfish nerves (\sim 300 μ A). The reason is probably a thick perineurium around the nerve. An average of 500 optical responses did not yield a surface displacement associated with neural activity. Because the axons could not be isolated from the connective tissue in the dissection, the nerve preparation is believed to reduce or diminish the surface displacement of the stimulated axons. The perineurium in the squid model is emphasized in Figure 8.14.

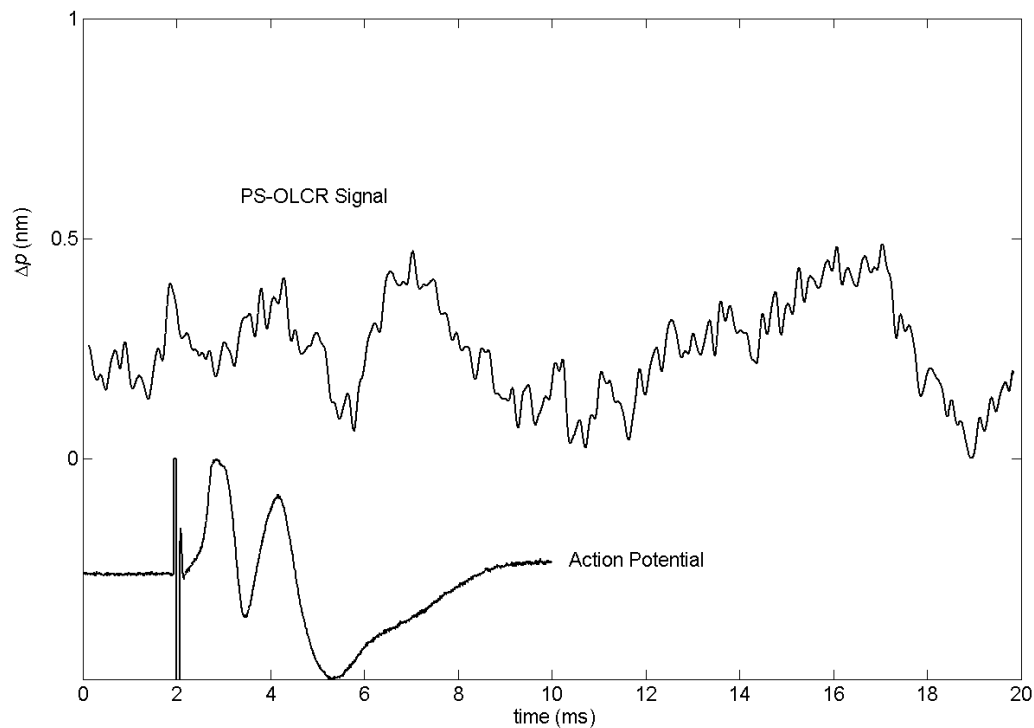


Figure 8.11: Optical path length change of a surface displacement experiment performed on a stimulated squid nerve. Action potential is in arbitrary unit. Stimulus (4 mA, 50 μ s) is at 2 ms. 500 optical responses are averaged.

8.5.2 Retardation Change

Retardation (R) is the product of birefringence (Δn) and sample thickness (d), ($R=\Delta n \times d$). Nanometer range surface displacements demonstrated in Section 8.5.1 imply that the nerve thickness alters due to neural stimulation. Moreover, the retardation changes (ΔR) during neural activity were measured in transmission mode experiments by many authors, and attributed to a change in birefringence. This section aims the detection of retardation change in stimulated crayfish and squid nerves using the reflection mode measurements of PS-OLCR.

In retardation change experiments, nerve under investigation was placed parallel to one of the PS-OLCR polarization channels. The beam is focused on a non-conductive reflecting surface placed under the nerve (Figure 8.1 and Figure 8.2b). Interference signals of PS-OLCR channels are formed from this reflecting surface. The sample path configuration is previously described in Section 8.4.2. Recorded interference fringes are post-processed as described previously in Section 2.3.3. The digital band-pass filter used in signal processing (Figure 2.7) has a 10 kHz bandwidth. Correspondingly, the cut-off frequencies of differential amplifier that measures the electrical action potential set to 10 Hz and 10 kHz. The optical path length change due to a retardation change is calculated from the differential phase ($\Delta\phi$) signal according to (2.8).

Figure 8.12 shows a cross-sectional histology slide of a crayfish nerve. Axons of different size and sheaths are clearly visible. Experimental data illustrated in Figure 8.13 is acquired from this nerve.

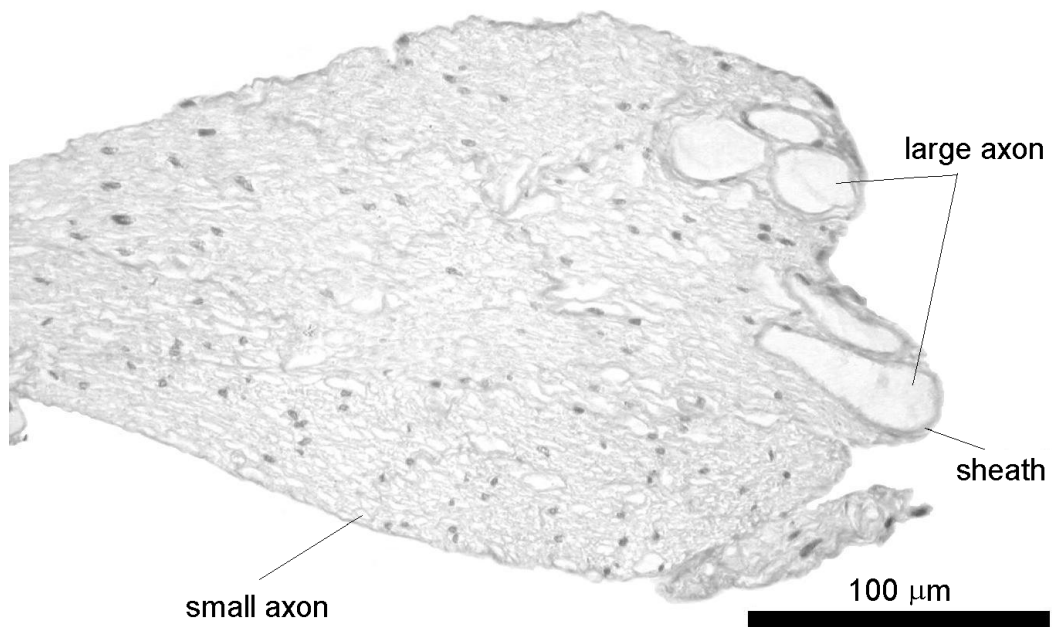


Figure 8.12: Histology (trichrome staining) of a crayfish walking leg nerve.
Experimental data shown in Figure 8.13 is recorded from this nerve.

Figure 8.13 shows the electrical action potential and optical path length variations between the PS-OLCR channels. Current pulses ($300 \mu\text{A}$, $50 \mu\text{s}$) are applied to the nerve at 2 ms, where there is a stimulus artifact in the electrical signal. The action potential appeared at 4 ms in the record.

In the experiment, interference fringes at frequency of 50 kHz are acquired at 5 Ms/s sampling rate. Although 500 optical responses are averaged and a few tens of picometer (pm) change in optical path length is detectable with the given signal to noise ratio, the optical signal in Figure 8.13 shows no indication of neural activity. The low frequency fluctuations in PS-OLCR signal are due to environmental noise, and are not consistent with the averages of sub-groups.

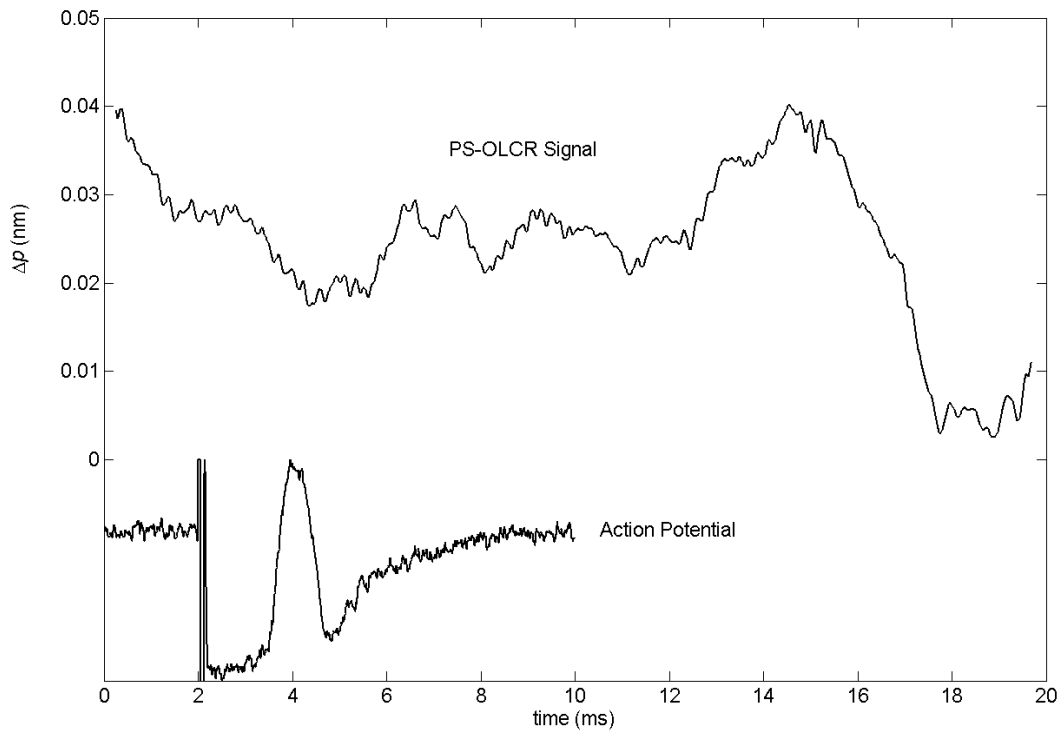


Figure 8.13: Optical path length change of a retardation change experiment performed on a stimulated crayfish nerve. Action potential is in arbitrary unit. Stimulus ($300 \mu\text{A}$, $50 \mu\text{s}$) is at 2 ms. 500 optical responses are averaged. There is no indication of neural activity in the given range of PS-OLCR signal.

The retardation change experiment is repeated using a squid nerve. Figure 8.14 shows a cross-sectional gray scale trichrome staining of the squid nerve. Small diameter fin nerves, a giant axon, and a thick connective tissue (perineurium) around the nerve are clearly visible. Figure 8.14 suggests that there are approximately 20-30 axons along the path of the PS-OLCR beam. Multiple axons with similar propagation speeds should increase the detected retardation change, if the response is cumulative.

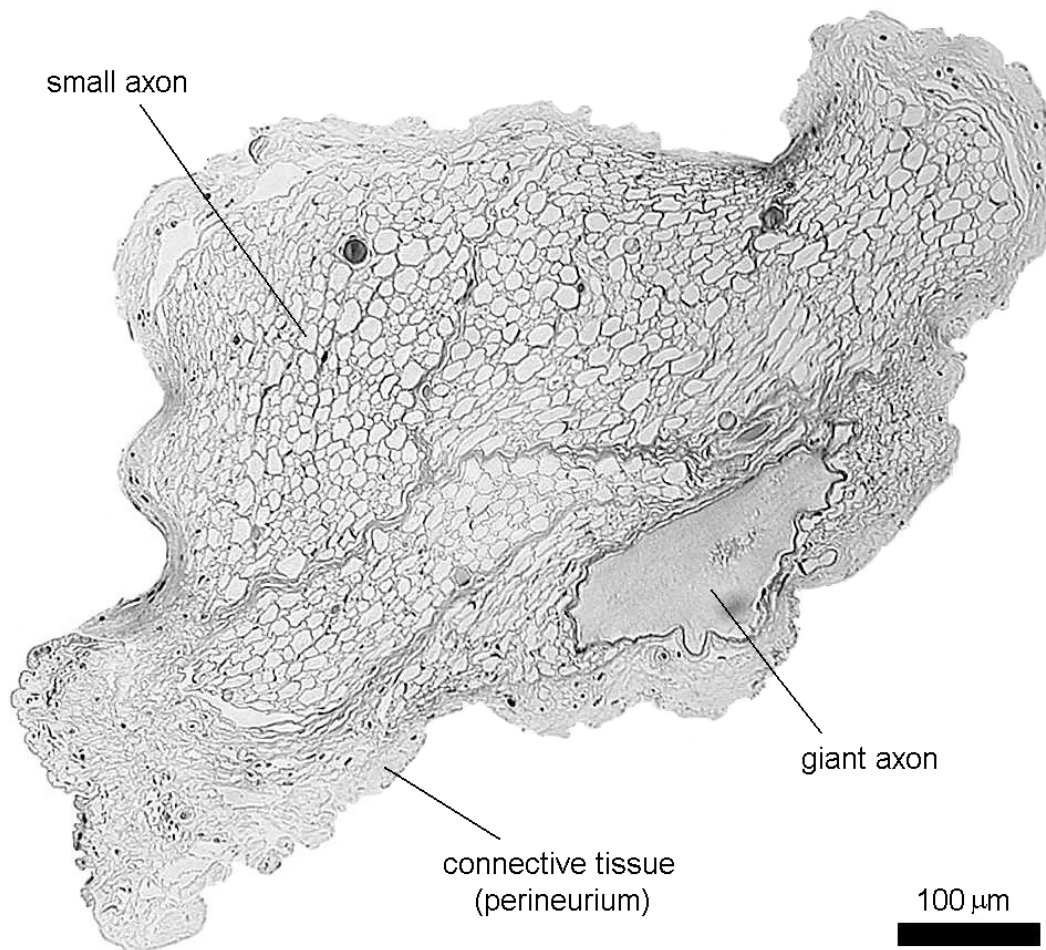


Figure 8.14: Histology (trichrome staining) of a squid nerve. A giant axon, fin nerve (small axons), and perineurium are indicated. Experimental data shown in Figure 8.15 is recorded from this nerve.

Figure 8.15 illustrates data recorded in the retardation change experiment of the squid nerve (Figure 8.14). Current pulses with stimulus amplitude of 3 mA and duration of 50 μ s are applied to the nerve at 2 ms in the records. As a result,

an action potential signal is observed after the stimulation. While acquiring the optical data at 5 Ms/s sampling rate, interference fringe frequency was 20 kHz. However, the bandwidths of both electrical and optical signals are again 10 kHz as displayed in previous experiments.

Although 1500 optical responses are averaged, path length change due to a change in retardation is not observed from the squid nerve. Figure 8.15 suggests that a path length change (or retardation change) of 10 pm would be resolved in this experiment.

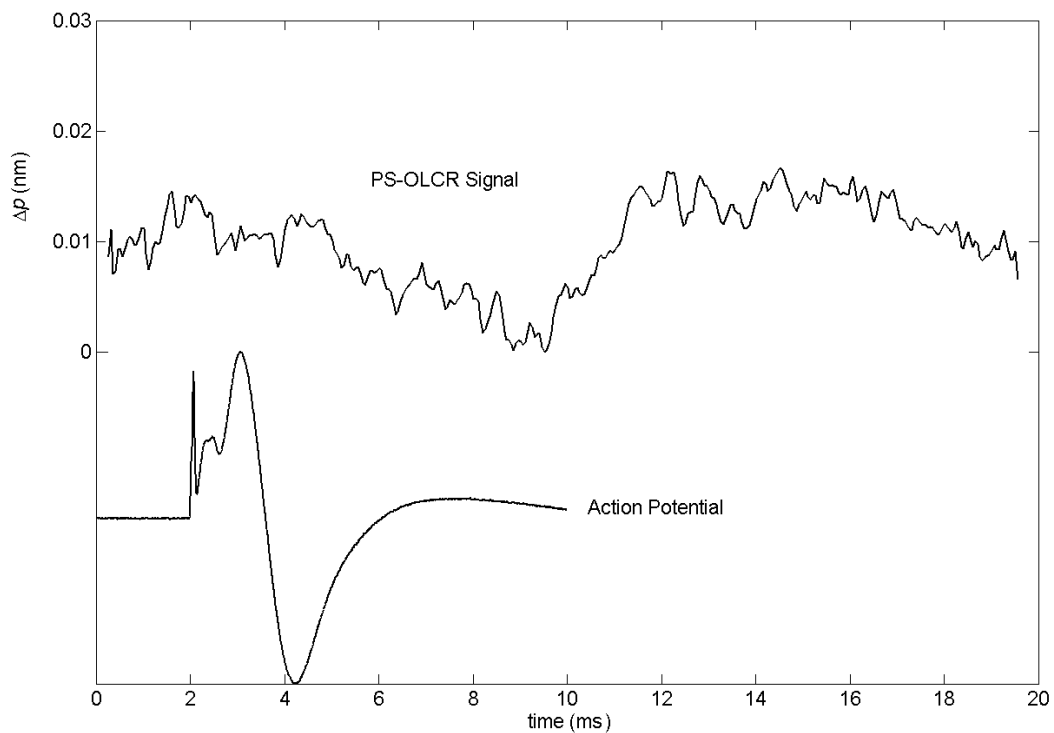


Figure 8.15: Optical path length change of a retardation change experiment performed on a stimulated squid nerve. Action potential is in arbitrary unit. Stimulus (3 mA, 50 μ s) is at 2 ms. 1500 optical responses are averaged. There is no indication of neural activity in the given range of PS-OLCR signal.

8.5.3 Optical Path Length Change

Optical path length (p) is the product of refractive index (n) and sample thickness (d), ($p=n \times d$). By measuring optical path length variations due to surface displacement, Section 8.5.1 demonstrated nanometer scale thickness changes using stimulated crayfish nerves. Then, the retardation change (ΔR) associated with neural stimulation was investigated in Section 8.5.2. PS-OLCR with a certain number of averages (500 for crayfish nerve, 1500 for squid nerve) could not detect an indication of neural activity. Previously reported retardation changes were extremely small (<10 pm). Because the refractive index change due to neural stimulation may be larger than a change in birefringence, this section explores a PS-OLCR use for detecting optical path length change itself. Moreover, by measuring the optical path length changes of the two orthogonal directions separately, the retardation change may be investigated further.

The PS-OLCR sample path configuration is described in Figure 8.2c. A 10X microscope objective (focal length of 14 mm) is used in crayfish nerve experiment. In the nerve chamber (Figure 8.1), the top surface of the cover glass and the reflecting surface underneath the nerve produce the interference signals. The polarization channel that oscillates along the long axis of the crayfish nerve is the probing channel; hence, its interference pattern is formed by the reflecting surface underneath the nerve. Interference fringe frequency is 50 kHz, and the channels are acquired at 5 Ms/s sampling rate. Digital signal processing is as described in Figure 2.7.

Histology slide of this crayfish nerve is not available. The dissected nerve had a few nerve bundles, which were visible using a surgical microscope. Neural stimulation with 300 μA , 50 μs current pulses resulted in action potential. Stimulus is presented at 2 ms and a corresponding electrical action potential is observed at 4 ms in Figure 8.16.

Figure 8.16 shows an average of 500 optical responses. Even though the signal to noise ratio in Figure 8.16 allows detection of 10-20 pm in optical path length change, an indication of neural activity could not be seen. This experiment on crayfish nerve is performed only once, and may be repeated in the future.

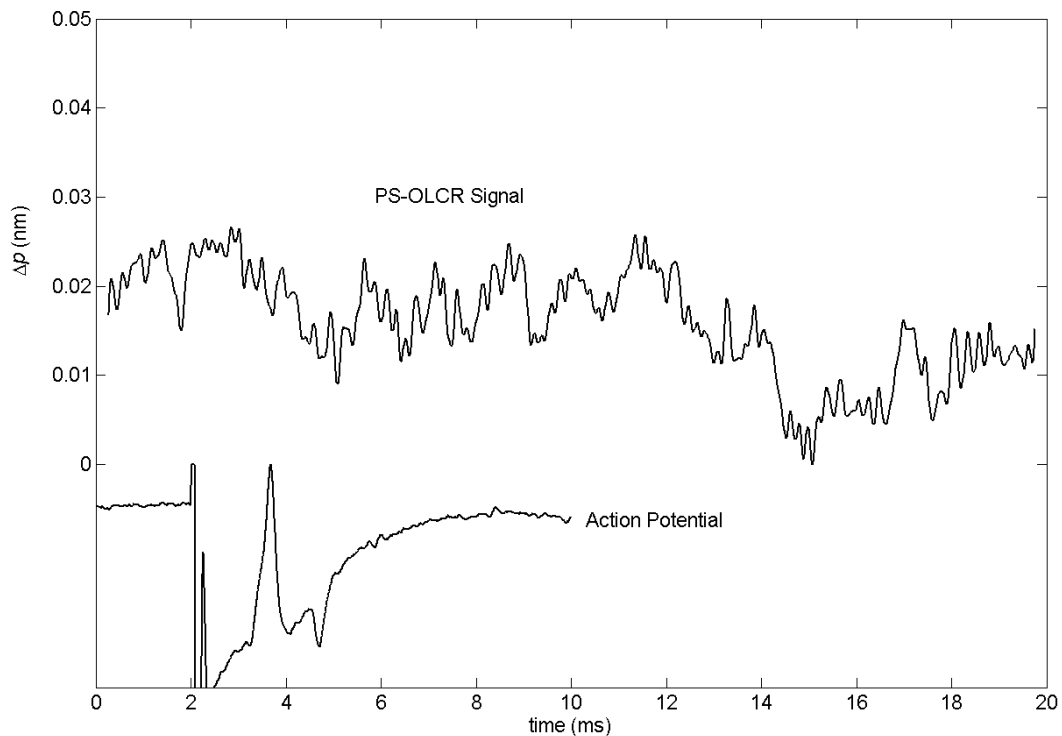


Figure 8.16: Optical path length change experiment performed on a stimulated crayfish nerve. Action potential is in arbitrary unit. Stimulus (300 μA , 50 μs) is at 2 ms. 500 optical responses are averaged. There is no indication of neural activity in this figure.

The second experiment to detect optical path length change is performed on a squid nerve. Although the squid giant axon is tried to be isolated, small axons of the fin nerve and a connective tissue exist in the histology section (Figure 8.17). Experimental data illustrated in Figure 8.18 are recorded from this nerve.

In Figure 8.18, the current pulses ($50\ \mu\text{s}$ in duration) are presented at $1\ \text{ms}$. Action potential is not recorded, but is expected to be observed at about $2\ \text{ms}$. Because the nerve remained attached to the squid mantle, the stimulation caused muscle twitching. Stimulus amplitudes are $75\ \mu\text{A}$ for the lower trace, and $300\ \mu\text{A}$ for the upper trace. Probably because the axons are not completely covered by perineurium, the stimulus amplitudes are smaller than the amplitudes used in the previous squid nerve experiments.

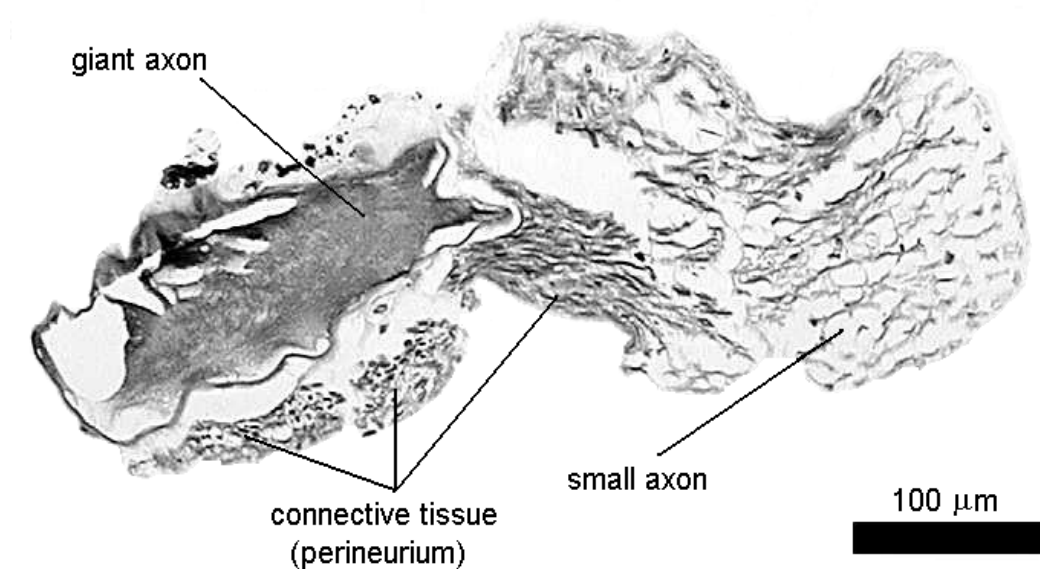


Figure 8.17: Histology (trichrome staining) of a squid nerve. A giant axon, fin nerve (small axons), and perineurium are indicated. Experimental data shown in Fig. 8.18 are recorded from this nerve.

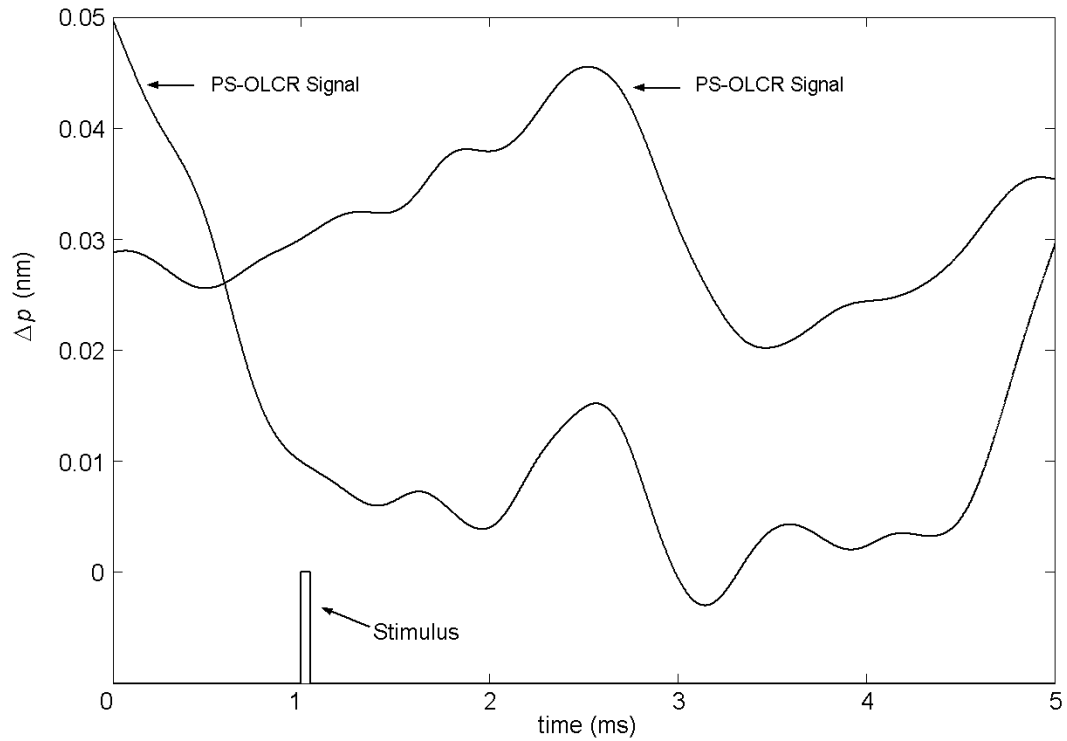


Figure 8.18: Optical path length change experiment performed on a stimulated squid nerve. Stimulus ($50 \mu\text{s}$) is $75 \mu\text{A}$ for the lower trace and $300 \mu\text{A}$ for the upper trace, and presented at 1 ms. Optical traces are average of 250 responses that are recorded from different regions of the nerve. Action potentials are not available.

The two traces of optical path length variations illustrated in Figure 8.18 are recorded from the edge and middle of the squid nerve shown in Figure 8.17. However, precise location of regions that light passed through are not known. In the sample path, a lens with 30 mm focal length is used. In signal processing (Figure 2.7), the bandwidth of the digital band-pass filter is 3 kHz. Each optical trace is average of 250 responses.

Approximately 20 pm changes in the optical path length traces (middle features in Figure 8.18) may be due to action potential propagation. Because the fluctuations in PS-OLCR signals are relatively large, no decision can be made. In other words, the features may be noise and the timing may be a coincidence. Action potential recording and further investigation is needed. Comparison and discussion of the experimental results associated with neural activity are presented in Section 8.6.3.

8.6 DISCUSSION

Section 8.6.1 presents possible mechanisms of neural surface displacement. Because PS-OLCR signals in swelling and shrinkage directions are observed due to the neural activity (Section 8.5.1), related results reported previously are restated. Section 8.6.2 compares timing of electrical and optical records. Finally, Section 8.6.3 discusses experimental results of this chapter.

8.6.1 Mechanisms to Explain Surface Displacements

In Section 8.5.1, the PS-OLCR optical measurements demonstrated nanometer scale displacements of crayfish nerve surface due to neural activity. Surface displacements in swelling or shrinkage directions are obtained in different experiments. Interestingly, B. C. Hill *et al.* (1977) reported a rapid contraction of a stimulated crayfish axon followed by a slow and small expansion. In another study, D. K. Hill (1950) observed an initial shrinkage of cuttlefish axons followed by a large swelling phase in response to repetitive stimuli.

The initial shrinkage and also the swelling mechanisms are not easy to explain. D. K. Hill (1950) pointed out that potassium remains associated with its hydration water, which accompanies the ion through the membrane, whereas the sodium ion is forced to part with its hydration water. This may shrink the nerve in the beginning of the repetitive excitation, and the reversal rate will depend on the permeability of the membrane to water. However, D. K. Hill added that the observed shrinkage might be too large to be explained by this mechanism. In his second explanation, the nerve swells because the sodium and chloride enter the fiber due to a sudden increase in sodium permeability. If the interior of the nerve fiber is initially under hydrostatic pressure, there will be a tendency for the nerve fiber to shrink, which could cause a rapid extrusion of potassium and chloride ions in the active state. Therefore, the net ionic exchange may be inwards at the beginning. In my experiments, tying the nerve ends with sutures helps guiding the nerve through the optical readout channel and prevents leakage of axoplasm, but it may also cause a pressure increase in the axons.

Tasaki and Byrne (1989) stated that the swelling observed in the squid giant axon was more than two orders of magnitude greater than the value expected from the process of $\text{Na}^+ - \text{K}^+$ ion exchange during excitation. Tasaki and Byrne (1990) suggested that the mechanical and electrical changes in the excited nerve fiber arise from replacement of divalent cations (Ca^{2+}) bound to multianionic sites of the membrane macromolecules with univalent cations (Na^+ and K^+). Such a cation-exchange process may convert compact layers in and near the membrane into swollen, low-density structures, and give rise to a development of repulsive

electrostatic force between fibrous macromolecular elements near the membrane. As a result, it may contribute to a rise in lateral expansion of the nerve fiber.

8.6.2 Comparison of Optical and Electrical Signals

Action potential is an indication of information transfer, and a product of structural changes in the active nerve. Electrical current pulses can initiate action potential propagation using intra-cellular or extra-cellular electrodes. Similar electrodes can be used to record voltage difference due to action potential propagation. But, use of such electrodes in many applications is not feasible, and not desirable because of a potential damage to the nerve fibers. Therefore, a non-invasive technique for measuring neural activity is needed. The optical differential phase measurements of PS-OLCR are applied to detect neural activity for the same reason.

The surface displacements of crayfish leg nerve reported in Section 8.5.1 are compared with the electrical recording of action potential. Because these two measures are different manifestations of the neural activity, the comparison of the electrical and optical signals may be difficult. For example, the electrical signal is a compound action potential produced by many axons (~1-20 μm in diameters for crayfish nerve). However, PS-OLCR signal may only come from a few axons because of a small (4 μm) beam spot on the nerve.

The timing of electrical signal is used to predict arrival of action potential at the optical recording site. In the nerve chamber, two platinum wires measured the electrical action potential, differentially. The action potential is thought to

arrive at the first and second recording electrodes (platinum wires) at the negative and positive peaks of the electrical action potential signal, respectively. Because the optical readout is performed between these two electrodes, the zero-crossing of the electrical signal should indicate time of arrival of the action potential to the optical measurement area. The PS-OLCR signals indicating the optical measurement of surface displacement occurred around the zero crossing of the electrical signal.

8.6.3 Detectable Signals

Surface displacements in the order of 1 nm in amplitude and 1 ms in duration are measured from stimulated crayfish nerves using PS-OLCR (Section 8.5.1). The amplitude and duration of surface displacement is consistent with the results reported by Hill *et al.* (1977). They used gold particles positioned on a crayfish giant axon (180 μm in diameter) and observed changes in the axon diameter with an amplitude of 1.8 nm and a period of about 1 ms.

Although 0.5 nm swelling of squid giant axon associated with action potential propagation was measured using a fiber sensor again with gold particles placed on the axon (Iwasa and Tasaki, 1980), surface displacement from squid nerve could not be detected in PS-OLCR experiments. The reason is most likely due to the nerve preparation. Histology sections showed that diameters of giant axons in *Lolliguncula brevis* are nearly 150-200 μm , which makes the dissection difficult. Therefore, the giant axon could not be isolated. In fact, the dissected nerve was a compound and included smaller axons of fin nerve and a thick

connective tissue (perineurium) around the axon bundles. Probably because of the connective tissue, surface displacements of the squid nerve could not be detected by PS-OLCR. Given a limited experience on dissections, if squid specimens having larger axons were accessible, the giant axon would be isolated from the connective tissue.

Section 8.5.2 investigated neural activity using retardation change measurements of PS-OLCR. Although 10-20 pm resolution is achieved by averaging, PS-OLCR could not detect a retardation change in squid and crayfish nerves. The retardation changes reported by Cohen *et al.* (1969) are 0.2 pm for a squid axon, 10 pm for a crab leg nerve and 60 pm for an electric organ of *Electrophorus Electricus*. 41 pm change in retardation was reported for a pike olfactory nerve (von Muralt, 1975). Therefore, the retardation change due to excitation of a single axon is extremely small, and may not be detected by the PS-OLCR differential phase measurements with a reasonable number of averages. Since olfactory nerves of pike and garfish, and walking leg nerves of crab, crayfish and lobster consist of many axons, the PS-OLCR experiment may be repeated using such nerves with increased number of averages. These experiments are important, because the basis of previously reported results (Section 8.3.3.2 Birefringence Change) that indicate neural activity are still not clear.

If the refractive indices in two orthogonal directions were change equally during neural activity, the birefringence ($\Delta n = n_2 - n_1$) would not change even though the optical path length might vary considerably. Section 8.5.3 aimed to detect a transient change in the optical path length, but could not conclude the

measurements in which 10-20 pm resolution was achieved. Analysis of such a response in the two orthogonal directions ($n_1 \times d$ and $n_2 \times d$, where d is sample thickness) may yield the retardation ($R = \Delta n \times d$) change using a simple subtraction. But, the thickness, which varies during neural activity, is still coupled in the equation. If surface displacement contributes to the birefringence signal reported in previous years, it needs to be quantified. Moreover, the nerve is a birefringent tissue and surface displacement could directly change the form birefringence. Hill (1950) reported that neural surface displacement in response to rapid repetitive stimuli could be as large as 100 nm. The repetitive stimulation is not expected to increase birefringence signal caused by reorientation of membrane molecules, because the action potential works with 'all or none' rule. Hence, effects of thickness change on these measurements can be investigated further.

The movements of ions across the membrane during action potential propagation should produce concentration changes in the axons. Such a concentration change results in a refractive index change (see Chapter 3), which alters optical path length. Presence of extracellular fluid (saline solution) and surface displacement are believed to reduce the optical path length variations due to concentration change. For example, if the extracellular and intracellular fluids along the light path are exchanged during neural activity, the resulting optical path length may not alter. An increase in thickness (d) should reduce the refractive index (n) due to a decrease in density. However, the thickness and refractive index variations may not compensate each other completely ($p = n \times d$).

8.7 CONCLUSION

Without introducing any chemicals or reflection coatings, PS-OLCR measured nearly 1 nm surface displacement associated with neural activity. The surface displacement recorded from crayfish walking leg nerve is approximately 1 ms in duration, and occurred about the action potential arrival to the optical measurement site. These findings are consistent with the results reported previously.

Use of PS-OLCR to detect neural activity is investigated using two different nerve models (crayfish and squid nerves) in three different configurations, which are designed to measure transient changes in surface displacement, retardation and optical path length. Among these changes, the surface displacement yields the largest signal that is detectable by PS-OLCR differential phase measurements. To verify neural activity, electrical action potentials are recorded and compared with the optical signals. Histology sections of the nerves used in the experiments are given, as well. The experimental results are discussed and compared with related studies that are reviewed in Section 8.3.

Since neural diseases are debilitating, and nerve cell death is irreversible, early detection of neuropathies is extremely important. Results reported in this dissertation suggest that PS-OLCR is a good candidate for non-invasive measurement of transient structural changes associated with neural activity. Since no chemicals or reflection coatings that may harm the nerve were applied, the PS-OLCR technique may be used for early detection of neural diseases such as glaucoma, multiple sclerosis and Alzheimer's.

Chapter 9: Summary, Future Directions and Conclusion

9.1 SUMMARY

A detailed description of the fiber-based phase sensitive optical low-coherence reflectometer (PS-OLCR) is given in *Chapter 2*. System performance is optimized, and Angstrom/nanometer scale measurement of optical path length changes is demonstrated. PS-OLCR differential phase measurements are applied to several areas in the following chapters.

Measurement of analyte concentration in clear and turbid media with sub-milliMolar sensitivity is presented in *Chapter 3*. The application is particularly important to monitor glucose concentration in blood. In *Chapter 4*, PS-OLCR application is applied to measure chromium nano-steps made of chromium films deposited on microscope slides. The aim of *Chapter 4* is to show non-contact imaging of surface topography with nanometer scale resolution. Phase calculation algorithm and possible extension of the technique to tissues or biomaterials are discussed.

Chapter 5 and *Chapter 6* concentrate on non-contact imaging of tissue response to external stimuli. Surface displacements in electrically stimulated cartilage are studied in *Chapter 5*. Stimulus with lower frequency and higher amplitude cause larger surface displacement of cartilage. Surface displacement of cartilage may differ between healthy and unhealthy cartilage. *Chapter 6* demonstrates depth resolved determination of tissue response to photothermal stimulation. Laser-induced photothermal changes inside an arterial tissue are

measured. The technique may be important in evaluating mechanical properties of arterial plaques.

Chapter 7 and *Chapter 8* focus on neural studies. In *Chapter 7* PS-OLCR is applied to measure nerve birefringence. In *Chapter 8* optical detection of neural activity using PS-OLCR is presented. Nanometer scale displacement of nerve surface is measured without introducing any chemicals or reflection coatings. Changes in retardation and optical path length are explored as well. Crayfish and squid nerves are used for each application. Among these, the surface displacement produced the largest signal that is detectable by PS-OLCR differential phase measurements. Electrical action potentials and histology sections are given. Results reported in *Chapter 8* suggest that PS-OLCR is a good candidate for non-invasive measurement of transient structural changes associated with neural activity. The PS-OLCR technique may be used for early detection of neural diseases such as glaucoma, multiple sclerosis and Alzheimer's.

9.2 FUTURE DIRECTIONS

Section 9.2.1 proposes a new PM fiber based system for differential phase measurements. Further improvement in the signal to noise ratio may be achieved because interference signals in each channel and cross terms are in different electrical frequencies. Section 9.2.2 presents achievement of sub-mM sensitivity in measurement of analyte concentrations. Section 9.2.3 and Section 9.2.4 discuss future studies of cartilage and arterial tissue response, respectively. Then, Section 9.2.5 recommends different experiments and supplementary work on detecting

neural activity, which may help understanding of transient changes in the active nerve and yield development of diagnostic tools for early detection of neural diseases. Section 9.2.6 points out some other applications of PS-OLCR.

9.2.1 Optical System

PS-OLCR is constructed using PM fibers designed for light at 1300 nm wavelength. Because water absorption at this wavelength is about one hundred times higher than water absorption at 800 nm, PS-OLCR may not be applied to retina to detect functionality. Therefore, a new system may be required for retinal applications. Moreover, signal to noise ratio in PS-OLCR's intensity images should be improved further. Current PS-OLCR intensity images may not compete with conventional OCT because of the relatively poor channel isolation in the PM fiber and interference of cross coupled light with a main component created by the 45° splice in the reference path.

A new PM fiber-based differential phase interferometer is designed at 800 nm, and aimed to obtain more information as well as higher signal to noise ratio. The system is called Frequency Multiplexed Optical Low-Coherence Reflectometer (FM-OLCR). Like PS-OLCR, FM-OLCR has two polarization channels, but each channel detects different fringe frequencies. By using digital band-pass filters, channel isolation in PM fiber would be less problematic.

Figure 9.1 illustrates a schematic diagram of the FM-OLCR whose channels correspond to the orthogonal polarization modes of the PM fiber. The input PM fiber segment creates two decorrelated linearly polarized modes (**f**- fast,

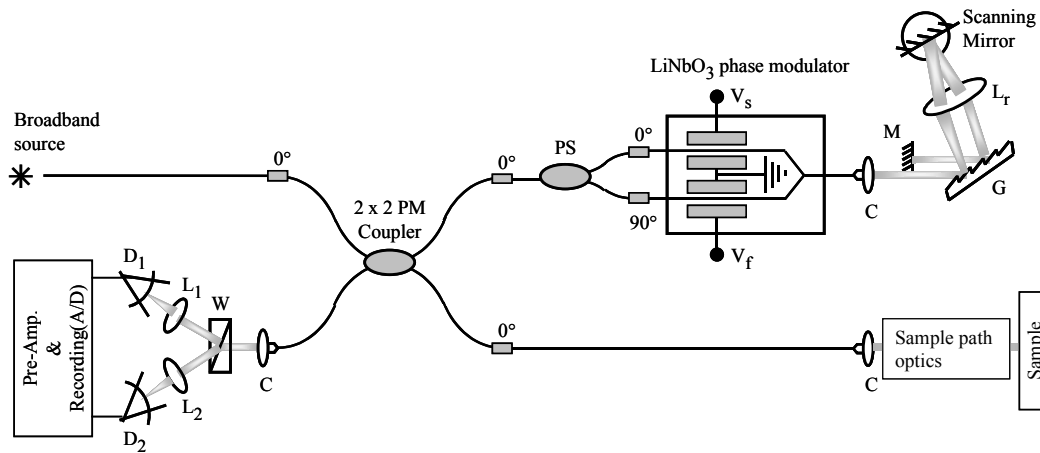


Figure 9.1: Frequency multiplexed optical low-coherence reflectometer. C- collimator, D- photo detector, G- diffraction grating, L- lens, M- mirror, PS- polarization splitter, V- modulation voltage, and W- Wollaston prism. Small rectangles indicate fiber splices and the values show the splice angle in degrees.

and s-slow) that propagate along the birefringent axes of the PM fiber. Light splits into the reference and sample paths at the 2 x 2 PM coupler.

A fiber polarization splitter (PS) in the reference arm splits **f** and **s** to modulate separately in the Lithium Niobate (LiNbO₃) Y-waveguide electro-optic phase modulator. If a fiber-based polarization splitter is not available, a polarization beamsplitter or Wollaston prism can be used. The LiNbO₃ phase modulator allows light propagation of one linearly polarized state (**s**); therefore a 90° splice is used to couple **f** into the slow axis of the modulator.

f and **s** are modulated by V_f and V_s saw-tooth waveforms of equal frequencies, but different voltage levels. Specifically, one path introduces 0 to

$\lambda/2$ ($V_s=V_\pi$) and the other path introduces 0 to $3\lambda/2$ ($V_f=3V_\pi$) linear phase delays. To synchronize the fringes, a single function generator should drive both waveguide segments. The modes are combined at the modulator output. The rapid scanning optical delay line (Tearney and Bouma, 1997) shown in the rest of the reference arm compensates the material and waveguide dispersion imbalance in the interferometer. **f** and **s** of back reflected light equally split in the LiNbO₃ phase modulator. Again, 0 to $\lambda/2$ and 0 to $3\lambda/2$ linear phase delays are added in the modulator. The polarization splitter combines the modes and delivers into the 2 x 2 PM coupler. Consequently, when LiNbO₃ phase modulator is driven by saw-tooth waveforms of frequency (f), the following components are created in the 2 x 2 PM coupler:

$f_1=f$: 0 to λ modulation (2π) of **s** in the slow axis,

$f_2=2f$: 0 to 2λ modulation (4π) of **s** in fast axis, and **f** in slow axes,

$f_3= 3f$: 0 to 3λ modulation (6π) of **f** in the fast axis of the PM fiber.

Because **f** and **s** must propagate equal path lengths in the reference and sample arms, a pair of birefringent wedges can be inserted into the sample path for aligning the coherence functions precisely. When reference and sample path lengths are equal, light back reflected from reference and sample arms form an interference signal in the 2 x 2 PM coupler.

The Wollaston prism in the detection path separates the two fiber polarization channels for signal detection. Output of each photo-detector is amplified and low-pass filtered to prevent aliasing. The digitized channels are stored in computer memory for signal processing.

In summary, the slow channel is detected by the slow detector at frequency f , the fast channel is detected by the fast detector at frequency $3f$, and cross terms are detected by each detector at frequency $2f$. It is important to note that frequency content of the interference fringes are precisely known, and differential phase measurement is possible. Moreover, changing the drive signals applied to the LiNbO₃ phase modulator allows different measurements. For example, the cross-terms can be removed optically by driving the fast channel at frequency $-f$.

9.2.2 Measurement of Analyte Concentrations

Measurements for analyte concentrations can be achieved in sub-mM sensitivity using PS-OLCR. Because slow drift in phase difference due to environmental factors and temperature dependence of refractive index of analytes, analyte concentrations should be measured fast (milliseconds). Scanning a dual-channel microfluidic cell, which contains a known reference solution and the sample analyte, can result in fast measurements. Moreover, if the sample solution circulates in the channel, continuous monitoring of analytes may be achieved. The sub-channels can be placed laterally that requires scanning the sample or sample beams. An alternative cell design may include two longitudinally placed cells, which requires scanning in depth using the reference galvanometer.

Physiological range and refractive index change per unit concentration of glucose may yield larger phase shifts than the other analytes (Chapter 3). However, direct measurement of glucose concentration from physiological tissues

may be problematic in areas having different combination and concentration of analytes. If laser irradiation at a specific wavelength, which targets glucose or any other analyte, is applied to the sample, temperature induced refractive index change due to absorption may yield a technique for measuring analyte concentrations in complex media.

9.2.3 Electrokinetic Response of Cartilage

In cartilage, lower frequencies and higher amplitudes of the electrical stimulation caused larger surface displacements. Because surface displacement of cartilage depends on stimulation frequency, a chirp waveform consisting of stimulation frequencies may be applied for frequency domain analysis of the cartilage response. Since the PS-OLCR with laterally displaced channels does not require a reference glass surface, relative displacement between two laterally distinct points on the cartilage surface is possible.

PS-OLCR can yield depth resolved measurement of reflectivity. Therefore, stress induced inside cartilage due to electrical stimulation may result in refractive index or birefringence variations. For example, application of laser pulses that generate photothermal related changes in tissue is suggested as an alternative stimulation method. Temperature rise due to the absorption of laser pulses can induce stress and deformation in cartilage. Surface waves can also be detected. The measurement of stress-induced birefringence change suggests a PS-OLCR single beam operation. Further work is requested to investigate non-contact PS-OLCR assessment of cartilage viability.

9.2.4 Photothermal Response of Arterial Tissue

Mechanical properties of atherosclerotic plaques may be assessed using PS-OLCR in combination with laser excitation, which triggers photothermal response in the arterial tissue. PS-OLCR provides not only depth-resolved images, but also nanometer scale path length changes between two points in arterial tissue in response to laser stimulation. Because of unknown factors such as non-uniform distribution of chromophores, the preliminary results reported in Chapter 6 are difficult to interpret. Additional experiments should be performed in simpler models. Surface temperature of the samples should be monitored during the experiments.

9.2.5 Optical Detection of Neural Activity

Repetitive stimulation of cuttlefish axons (~ 200 stimuli/s) was reported to give a cumulative surface displacement, which can be as large as 100 nm (Hill, 1950). In this case the surface displacement is created in a few minutes, and would be detected using PS-OLCR. Although such a signal is not due to faster events (milliseconds) taking place during action potential propagation, it is worthwhile to investigate in a great detail. For example, if surface displacement contributes to the birefringence signal reported in previous years, it needs to be quantified. Nerve itself is a birefringent tissue; therefore, the surface displacement could directly change the form birefringence. Since the action potential works with ‘all or none’ rule, the repetitive stimulation is not expected to increase birefringence signal caused by reorientation of membrane molecules.

Comparison of electrical and optical signals can be done in time domain. Since the optical signal is due to a limited region of the nerve, the comparison of electrical and optical signals may be difficult when the electrical signal is a compound action potential. A squid giant axon seems an ideal model for an easy comparison, because it contributes to the electrical and optical signals by itself. In any case, the dissection and alignment of the nerve require adequate control. Presence of connective tissue around the nerve may damp or diminish the surface displacement signal. Incorporating PS-OLCR with a microscope would be helpful for dissecting and targeting the right region of the nerve.

Animal models having large number of axons should be utilized for measuring optical path length and retardation change experiments. The olfactory nerves of pike and garfish, and walking leg nerves of crab, crayfish and lobster consist of many axons and may be used in further investigation of optical path length and retardation changes. On the contrary, squid giant axon can be studied for surface displacements due to action potential propagation. Squid species having larger giant axon are suggested for easy dissection.

Eye experiments require a wavelength that is not strongly absorbed in the vitreous. FM-OLCR described in Section 9.2.1 is suitable for experiments in the retinal nerve fiber layer, if operating at a wavelength of 850 nm. The sample path of the system may be integrated in a slit lamp. In the eye, retinal stimulation can easily be achieved by visual stimuli, or by a checkerboard pattern. Special care may be taken to block unwanted light entering in eye through the pupil.

The nerve chamber used in *Chapter 8* has some similarities with structures in the eye. For example, the nerve is immersed in water as the retina behind the vitreous. The reflecting surface under the nerve imitates the retinal pigment epithelium, which is a reflecting surface behind the retina. Therefore, change in optical path length and retardation studies can be performed in the retina by using back-reflected light from these biological layers. However, the detection of surface displacement due to retinal stimulation requires a reference surface. If we consider longitudinally displaced channels, the lens is the closest anterior reference surface to the retina. But, its distance from the retina and physiological movements would make this approach extremely difficult. A good alternative is to use the retina as a self-reference. This can be achieved using laterally displaced channels in which the interference signals are formed using the vitreous-retina interface. Local stimulation using visual wavelengths may allow retinal stimulation of a selected area. This configuration has potential use to detect retinal neuropathies.

9.2.6 Other Applications

Additional applications can be derived from PS-OLCR. An example is quantitative phase contrast *en face* imaging of cells with sub-cellular resolution (submitted to *Optics Letters* by Rylander *et al.* in 2003). The goal of the study is to realize a differential phase contrast microscope for quantitative measurements of cellular structures and cellular events. Refractive index distribution of biological tissues with constant thickness (i.e. histology sections), and imaging of

live cells with or without external stimuli are good examples of such a microscope. Moreover, if the use of PM fiber probes in endoscopic probes is feasible, PS-OLCR may yield a number of new applications *in-vivo*.

9.3 CONCLUSION OF THE DISSERTATION

Based on the experimental results reported in this dissertation, a highly sensitive and accurate PS-OLCR for phase sensitive ranging of biological materials is designed and developed. Optical problems of the device are identified and engineering solutions are implemented. In addition to non-invasive, depth resolved ($\sim 10 \mu\text{m}$) imaging of tissue microstructures, PS-OLCR yields Angstrom/nanometer scale optical path length changes between two depth-resolved polarization channels using differential phase measurements. Then, biomedical applications of PS-OLCR to obtain a novel diagnostic tool are presented in each chapter. Application areas investigated in this dissertation are concentration measurement of analytes including glucose, imaging surface topography, cartilage surface response to electrical stimulation, arterial tissue response to photothermal stimulation, birefringence measurement of nerves and optical detection of neural activity. For each application, results of PS-OLCR differential phase measurements are presented and discussed. If a clinical diagnostic device similar to that presented here is designed for non-contact, non-invasive, or minimally invasive applications, work reported in this dissertation will provide an important basis.

References

- Akkin, T., Davé, D. P., Youn, J., Telenkov, S. A., Rylander-III, H. G., and Milner, T. E.; 'Imaging tissue response to electrical and photothermal stimulation with nanometer sensitivity', *Lasers in Surgery and Medicine*, 33: 219-225 (2003).
- Bear, R. S., Schmitt, F. O., and Young, J. Z.; 'The sheath components of the giant nerve fibers of the squid', *Proc. Royal Soc. London, Series B, Biological Sciences*, 123: 496-504 (1937).
- Berkenblit, S. I., Frank, E. H., Salant, E. P., and Grodzinsky, A. J.; 'Nondestructive detection of cartilage degeneration using electromechanical surface spectroscopy', *Tran. ASME*, 116: 384-392 (1994).
- Bhusnan, B., Wyant, J. C., and Koliopoulos, C. L.; 'Measurement of surface topography of magnetic tapes by Mirau interferometry', *Applied Optics*, 24: 1489-1497 (1985).
- Bohren, C. F., and Huffman, D. R.; 'Absorption and Scattering of Light by Small Particles', Wiley, NY, (1983).
- Bryant, S. H., and Tobias J. M.; 'Optical and mechanical concomitants of activity in carinus nerve I. Effect of sodium azide on the optical response II. Shortening of the nerve with activity', *J. Cellular Comp. Physiol.*, 46:71-95 (1955).
- Cohen, L. B., Keynes, R. D., and Hille, B.; 'Light scattering and birefringence changes during nerve activity', *Nature*, 218: 438-441 (1968).
- Cohen, L. B., Hille, B., and Keynes, R. D.; 'Light scattering and birefringence changes during activity in the electric organ of electrophorus', *Journal of Physiology*, 203: 489-509 (1969).
- Cohen, L. B., Hille, B., and Keynes, R. D.; 'Changes in axon birefringence during the action potential', *Journal of Physiology*, 211: 495-515 (1970).
- Cohen, L. B., Hille, B., Keynes, R. D., Landowne, D., and Rojas, E.; 'Analysis of the potential-dependent changes in the squid giant axon', *Journal of Physiology*, 218: 205-237 (1971).

- Cohen, L. B.; 'Changes in neuron structure during action potential propagation and synaptic transmission', *Physiological Reviews*, 53: 373-418 (1973).
- Davé, D. P., and Milner, T. E.; 'Optical low-coherence reflectometer for differential phase measurement', *Optics Letters*, 25: 227-229 (2000).
- Davé, D. P., Akkin, T., Milner, T. E., and Rylander III, H. G.; 'Phase-sensitive frequency-multiplexed optical low-coherence reflectometry', *Optics Communication*, 193: 39-43 (2001).
- Davé, D. P., Akkin, T., and Milner, T. E.; 'Polarization-maintaining fiber-based optical low coherence reflectometer for birefringence characterization and ranging', *Optics Letters*, 28: 1775-1777 (2003).
- de Boer, J. F., Milner, T. E., van Gemert M. J. C., and Nelson, J. S.; 'Two-dimensional birefringence imaging in biological tissue by polarization-sensitive optical coherence tomography', *Optics Letters*, 22: 934-936 (1997).
- Esenaliev, R. O., Larin, K. V., Larina, I. V., and Motamedi, M.; 'Noninvasive monitoring of glucose concentration with optical coherent tomography', *Optics Letters*, 26: 992-994 (2001).
- Frank E. H., and Grodzinsky, A. J.; 'Cartilage electromechanics I: electrokinetic transduction and the effects of electrolyte pH and ionic strength', *J. Biomechanics*, 20: 615-627 (1987).
- Frank E. H., and Grodzinsky, A. J.; 'Cartilage Electromechanics II: a continuum model of cartilage electrokinetics and correlation with experiments', *J. Biomechanics*, 20: 629-639 (1987).
- Grodzinsky, A. J.; 'Electromechanical and physicochemical properties of connective tissue', *CRC Critical Reviews in Biomedical Engineering*, 9: 133-199 (1983).
- Hammer, D. X., Dave, D. P., Milner, T. E., Choi, B., Rylander III, H. G., and Welch, A. J.; 'Investigation of the transduction mechanism of infrared detection in *Melanophila acuminata*: photo-thermal-mechanical hypothesis', *Comp. Biochem. and Physiology Part A*, 132: 381-392 (2002).
- Hill, B. C., Schubert, E. D., Nokes, M. A., and Michelson, R. P.; 'Laser interferometer measurement of changes in crayfish axon diameter concurrent with action potential', *Science*, 196: 426-428 (1977).

- Hill, D. K.; 'The volume change resulting from stimulation of a giant nerve fibre', *J. Physiology*, 111: 304-327 (1950).
- Hitzenberger, C. K., and Fercher, A. F.; 'Differential phase contrast in optical coherence tomography', *Optics Letters*, 24: 622-624 (1999).
- Huang, D., Swanson, E. A., Lin, C. P., Schuman, J. S., Stinson, W. G., Chang, W., Hee, M. R., Flotte, T., Gregory, K., Puliafito, C. A., and Fujimoto, J. G.; 'Optical coherence tomography', *Science*, 254: 1178-1181 (1991).
- Huglin, M. B.; 'Light Scattering From Polymer Solutions', Academic Press, New York, (1972).
- Iwasa, K., and Tasaki, I.; 'Mechanical changes in squid giant axons associated with production of action potentials', *Biochemical and Biophysical Research Communications*, 95: 1328-1331 (1980).
- Kandel, E. R., Schwartz, and Jessell, T. M.; 'Principles of neural science', 4th edition, McGraw-Hill, (2000).
- Kratz, A., and Lewandrowski, K. B.; 'Case records of the Massachusetts General Hospital. Weekly clinicopathological exercises. Normal reference laboratory values', *New England Journal of Medicine*, 339: 1063-1072 (1998).
- Landowne, D.; 'Molecular motion underlying activation and inactivation of sodium channels in squid giant axons', *J. Membrane Biol.*, 88: 173-185 (1985).
- Landowne, D.; 'Measuring nerve excitation with polarized light', *Japanese Journal of Physiology*, 43: Suppl.1, S7-S11 (1993).
- Larin, K. V., Eledrisi, M. S., Motamedi, M., and Esenaliev, R.O.; 'Noninvasive blood glucose monitoring with optical coherence tomography: a pilot study in human subjects', *Diabetes Care*, 25, p. 2263-2267 (2002).
- Larin, K. V., Motamedi, M., Ashitkov, T. V., and Esenaliev, R. O.; 'Specificity of noninvasive blood glucose sensing using optical coherence tomography technique: a pilot study', *Phys. Med. Biol.*, 48, 1371-1390 (2003).
- Long, F. H., and Deutsch, T. F.; 'Pulsed photothermal radiometry of human artery', *IEEE Journal of Quantum Electronics*, QE-23: 1821-1826 (1987).

- Maroudas, A.; 'Physicochemical properties of articular cartilage. Adult Articular Cartilage', Freeman, M.A.R. ed., Pitman Medical, Kent, England, 2nd ed.: 215-290 (1979).
- Rylander, C. G., Davé, D. P., Akkin, T., Milner, T. E., Diller K. R., and Welch, A. J.; 'Quantitative phase contrast imaging of cells with phase sensitive optical coherence microscopy', *Optics Letters*, submitted in 2003.
- Sato, H., Tasaki, I., Carbone, E., and Hallett, M.; 'Changes in axon birefringence associated with excitation: implications for the structure of the axon membrane', *Mechanochem. Cell Motility*, 2: 209-217 (1973).
- Schmitt, J. M.; 'Optical coherence tomography (OCT): A review', *IEE J. Selected Topics in Quantum Electronics*, 5: 1205-1215 (1999).
- Sun, D. N., Gu, W. Y., Guo, X. E., Lai, W. M., and Mow, V. C.; 'A mixed finite element formulation of triphasic mechano-electrochemical theory for charged, hydrated biological soft tissues', *Int J Numer Meth Eng*, 45:1375-1402 (1999).
- Takada, K., Yokohama, I., Chida, K., and Noda, J.; 'New measurement system for fault location in optical waveguide devices based on an interferometric technique', *Applied Optics*, 26: 1603-1606 (1987).
- Tasaki, I., Watanabe, A., Sandlin, R., and Carnay, L.; 'Changes in fluorescence, turbidity, and birefringence associated with nerve excitation', *Proc. Nat. Acad. Sci. U.S.*, 61: 883-888 (1968).
- Tasaki, I., Kusano, K., and Byrne, P. M.; 'Rapid mechanical and thermal changes in the garfish olfactory nerve associated with a propagated impulse', *Biophysical Journal*, 55: 1033-1040 (1989).
- Tasaki, I., and Byrne, P. M.; 'Volume expansion of nonmyelinated nerve fibers during impulse conduction', *Biophysical Journal*, 57: 633-635 (1990).
- Tasaki, I. and Byrne, P. M.; 'Rapid structural changes in nerve fibers evoked by electric current pulse', *Biochem. and Biophys. Research comm.*, 188: 559-64 (1992).
- Tearney, G. J., Bouma, B. E., and Fujimoto, J. G.; 'High-speed phase- and group-delay scanning with a grating-based phase control delay line', *Optics Letters*, 22: 1811-1813 (1997).

- Telenkov, S. A., Davé, D. P., Sethuraman, S., Akkin, T., and Milner, T. E.; 'Differential phase optical coherence probe for depth-resolved detection of photothermal response in tissue', *Physics in Medicine and Biology*, to be published in 2004.
- Torres, J. H., Motamedi, M., Pearce, J. A., and Welch, A. J.; 'Experimental evaluation of mathematical models for predicting the thermal response of tissue to laser irradiation', *Applied Optics*, 32: 597-606 (1993).
- Van de Hulst, H. C.; 'Light Scattering by Small Particles', Dover Publications, Inc., NY, (1981).
- von Muralt, A.; 'The optical spike', *Phil. Trans.*, B270: 411-42 (1975).
- von Muralt, A.; 'The optical spike, structure of the olfactory nerve of pike and rapid birefringence changes during excitation', *Pflügers Archiv, European Journal of Physiology*, 367: 67-76 (1976).
- Weast, R. C.; 'CRC Handbook of Chemistry and Physics', 70th ed., CRC, Cleveland, Ohio (1989).
- Welch, A. J., and van Gemert M. J. C.; 'Optical-thermal response of laser-irradiated tissue', Plenum Press, New York (1995).
- Yang, C., Wax, A., Georgakoudi I., Hanlon E. B., Badizadegan K., Dasari R. R., and Feld M. S.; 'Interferometric phase-dispersion microscopy', *Optics Letters*, 25: 1526-1528 (2000).
- Yao, X., Rector, D. M., and George, J. S.; 'Optical lever recording of displacements from activated lobster nerve bundles and *Nitella* internodes', *Applied Optics*, 42: 2972-2978 (2003).
- Youn, J., Akkin, T., and Milner, T. E.; 'Electrokinetic measurement of cartilage using differential phase optical coherence tomography', *Physiological Measurement*, 25: 85-95 (2004).
- Young, J. Z.; 'The structure of nerve fibers in cephalopods and crustacea', *Proc. Royal Soc. London, Series B, Biological Sciences*, 121: 319-337 (1936).
- Youngquist, R. C., Carr, S., and Davies, D. E. N.; 'Optical coherence-domain reflectometry', *Optics Letters*, 12: 158-160 (1987).

Vita

Taner Akkın, the second son of Hatice Akkın and Kazim Akkın, was born in Gölarmara, Manisa, Turkey on January 3, 1973. Primary and secondary schools were completed in the same town. After graduating from Computer Department of Çınarlı Technical High Scholl, İzmir, Turkey, in 1990, he entered Çukurova University, Adana, Turkey, where he received BS and MS degrees in Electrical and Electronics Engineering in 1995 and 1997, respectively. Taner came to The University of Texas at Austin in 1999 to pursue a Ph.D. in Electrical and Computer Engineering. He was advised by Drs. Thomas E. Milner and H. Grady Rylander III, and worked in the Biomedical Engineering Laser Laboratories. He specialized on fiber based interferometric techniques, and spent plenty of time to detect neural activity, which may be used as a non-invasive diagnostic tool for neural diseases.

Permanent address: Atatürk Mah. Akhisar Cad. No: 37

45580, Gölarmara, Manisa, Turkey

This dissertation was typed by the author.